Title	Design and Fabrication of Functional Hydrogel Composites: from Micro-scale to Macro-scale
Author(s)	高橋, 陸
Citation	北海道大学. 博士(生命科学) 甲第13160号
Issue Date	2018-03-22
DOI	10.14943/doctoral.k13160
Doc URL	http://hdl.handle.net/2115/89226
Type	theses (doctoral)
File Information	Riku_Takahashi.pdf

<u>Doctoral Dissertation</u>

Design and Fabrication of Functional Hydrogel Composites:
from Micro-scale to Macro-scale

（機能性ハイドロゲル複合材料のデザインと創製：ミクロからマクロまで）

By

Riku Takahashi

Supervisor: Jian Ping Gong,

Laboratory of Soft & Wet Matter,

Graduate School of Life Science, Hokkaido University

Sapporo 001-0021, Japan

March, 2018

Contents

CHAPTER 4 49

Visualizing Internal Stress in Hydrogel Matrix Based on Orientation of Semi-Rigid Polymer

CHAPTER 5 70

Creating Macro-scale Hydrogel Composites with Low Melting Point Alloys (LMA)

CHAPTER 1

General Introduction

1.1 Overview

Hydrogels, which are classified as soft/wet materials, exhibit unique properties that cannot be found in hard/dry materials, including low friction, high biocompatibility, stimuli-response, high permeability, and so on[1-4]. These properties strongly related to hydrogel structures, which are three-dimensional network formed by cross-linking polymer chains that can hold a large amount of water while maintaining the structures[5]. Thus, hydrogel actually represent a state of matter intermediate between solid and liquid and they are usually considered as showing a solid character with some features of a liquid[6]. Due to this, hydrogels show aforementioned outstanding functions, therefore, they are expected to be applied in a wide range of fields such as medicine, pharmacy, agriculture, biology, and engineering.

However, conventional hydrogels are brittle and fragile, highly limiting their applications. The brittleness of hydrogels originates from heterogeneity in the network structure and high solvent content[7,8]. The former induces stress concentration locally during fracture, which leads to crack propagation, and the latter causes the chains to be highly extended, decreasing entropy, leading to chain fracture. To overcome such limitations, over the past few decades, intense effort has focused on increasing the mechanical properties of hydrogels. Breakthroughs have occurred due to the development of the following techniques: (1) suppressing crack initiation by homogenization of the network structure (e.g. slide-ring gels and Tetra-PEG gels) [9, 10], and (2) preventing crack propagation by stress yielding (nanocomposite (NC) gels and double network (DN) gels) [11, 12]. These developments have greatly changed the conventional impression of this “weak” soft materials. Due to the maturation of hydrogel research, a new concept get a great deal of attention, which is “composite approach” combining hydrogel matrix with different kinds of materials to emergence outstanding functions for practical applications of hydrogels.

Last previous year in our laboratory, we have developed a lamellar photonic hydrogel, fabricated by combining a three thousands of lipid bilayer with a poly acrylamide (PAAm) hydrogel matrix, showing unique functions such as high toughness, stimuli-responsive structural color, and anisotropic swelling diffusion behavior[13-15]. In addition to this, by utilizing a glass-woven fiber and the poly ampholyte (PA) hydrogel matrix, a fiber reinforced hydrogel composite has been synthesized with extremely flexible yet tougher than metal materials despite of 40% water (in a volume ratio) [16, 17]. These hydrogel composites with outstanding functions suggest an innovation by coupling of hydrogels and different kinds of materials, which is a simple yet versatile approach for fabricating multi-functional materials that are required for high-quality biomedical material, wearable device, and soft robots.

For preparing hydrogel-based composite materials, both the size scale of the reinforcing phase and the “swelling” nature of the hydrogel are important factors. When the reinforcing phase is on the micro-scale (from several nm to several tens of μm) and well dispersed, the orientation of the reinforcing phase influences the resulting properties, but is difficult to independently control. Therefore, a method to control the swelling behavior and an understanding of how swelling influences reinforcing phase architecture is required. On the other hand, when the reinforcing phase is on the macro-scale (from several hundreds of μm to several cm), the matrix and reinforcing phases can be viewed as discrete, independent phases. Swelling the matrix does not inherently result in a change in geometry of the reinforcing phase. As a result, the volume change of the hydrogel matrix induced by swelling causes strong swelling mismatch and interfacial stress between the hydrogel matrix and reinforcing phase, resulting in surface creasing or bulk deformation, at best, and delamination or rupture, at worst. Thus, overcoming the swelling mismatch between components is crucially important to obtain macro-scale hydrogel composites. However, the primary approach in recent hydrogel composite has focused on suppressing the swelling of hydrogels (e.g. using non/slightly swellable hydrogels), with little effort spent attempting to relieve swelling mismatch by utilizing unique characteristics of the reinforcing phase. Therefore, towards establish a general design concept of fabricating functional hydrogel composites, we have developed both micro- and macro-scale hydrogel composite systems and demonstrated unique hybridized functions of the composites.

1.2 Outline of this dissertation

A general idea of composite materials and a back ground of study of hydrogel composite system has been discussed in **Chapter 2**. Also we explain why the composite approach is necessary and hydrogel-based composite have great potentials. The hydrogel composites are divided into two categories; (1) micro-scale hydrogel composites, and (2) macro-scale hydrogel composites. We review the recent progress of each composite systems, mainly focus on their unique functions.

In chapter 3, we report a novel and general strategy to develop micro-scale hydrogel composites with complicated long-range superstructures of rigid fiber-forming molecules by playing with programmed internal stress based on swelling control. Since orientations of semi-rigid polymers or nano rods/sheets embedded in gel matrix are sensitive to strain or internal stress, these randomly dispersed dopants show a uniform alignment under external tensile force. To create a complex superstructure of rigid macromolecules, programmed complex stress field is needed. We applied a photolithographic method to develop composite gradient in the patterned hydrogels. When a soft hydrogel has a swelling mismatching in different regions, an internal stress develops. By controlling the features of masked and unmasked regions of the gels, we can create a programmed internal stress, which induces the localized molecular orientation of rigid molecules. In addition, orientation is fixable by an interaction with the network of cationic gel by using the anionic rigid molecule. Furthermore, we develop a double network structure to tough the hydrogels with programmed superstructures, which deform reversibly under larger strain. This work presents a promising pathway to develop superstructures in hydrogels, and should shed light on designing other biomimetic materials with intricate molecular alignments toward applications in sensors, artificial organs, etc.

In chapter 4, we demonstrated a function of the aforementioned micro-scale hydrogel composites as visualization tool for mechanical instability. A hydrogel, which is soft and wet matter, is one of the model materials to investigate the phenomena such as surface creasing and bulk deformation induced by mechanical instability during swelling. Most studies on hydrogel swelling instability have been focused on a constraint boundary condition. In this chapter, we report the mechanical instability coupling between surface creasing and bulk bending during fast free swelling of a piece of disc-shape hydrogel. At the time of swelling, saddle like shape transition and stripe-like surface crease pattern which is completely different from the pattern under constraint boundary condition was observed. For visualize the mechanical instability of the hydrogels, the micro-scale hydrogel composite are used as stress sensor by determining the orientation of internal semi-rigid polymers. Additionally, we confirm the relationship between surface creasing and bulk bending by investigating the swelling-induced surface pattern on thin hydrogel film fixed onto a saddle-shaped substrate prior to swelling. As a result, anisotropy of surface creasing pattern was controlled by morphology of the substrate. Furthermore, a theoretical mechanism based on an energy model was developed to show anisotropic stripe-like surface crease pattern on a saddle shaped surface. This work should have a merit for develop novel strategies for controlling crease patterns on soft and wet materials by changing its three-dimensional shape.

In chapter 5, we report a simple yet versatile strategy to develop macro-scale hydrogel composites possessing a solid reinforcing phase based on a low melting point alloy (LMA). Since the LMA can transform from a load-bearing solid state to a free-deformable liquid state at relatively low temperature, Hydrogel-LMA composites can release the swelling mismatch by a thermal stimulus. We applied both deswellable and swellable hydrogels as matrix materials to show the universality of our method. The resultant materials show excellent mechanical properties including high stiffness and toughness. Beyond the mechanical properties, these composites demonstrate superior functional abilities such as shape memory, dynamic stiffness control, and thermal healing ability. In addition to this, we further demonstrated unique functions which cannot be achieved with neat hydrogels, including performing electro-chemical reactions in the hydrogel matrix and creating channel structures in the hydrogel for fluidic devices.

In chapter 6, we develop a 3D printable resin reinforced natural rubber or polyvinyl alcohol (PVA) gel system that is similar to the macro-scale composite hydrogel described in chapter 5. Taking advantage of high workability of the 3D printable resin reinforcement, we investigate the geometrical effect of the reinforcing phase in soft matrix on the mechanical properties. In the case of using characteristic architectures such as auxetic architecture (showing negative Poisson's ratio) as reinforcing phase, the macro-scale composites exhibit unique properties, including high stiffness, tunable Poisson's ratio, and work of extension. The knowledge obtained from this work might be helpful for creating smart macro-scale composites whose mechanical properties can be controlled precisely.

In chapter 7, concluding remarks of these works are summarized.

1.3 References

1. S. Ma, M. Scaraggi, D. Wang, X. Wang, Y. Liang, W. Liu D. Dini & F. Zhou, *Adv. Funct. Mater.,* **25,** 7366 (2015).
2. P. Li, Y. F. Poon, W. Li, H. Y. Zhu, S. H. Yeap, Y. Cao, X. Qi, C. Zhou, M. Lamrani, R. W. Beuerman, E. T. Kang, Y. Mu, C. M. Li, M. W. Chang, S. S. J. Leong & M. B. Chan-Park, *Nat. Matter.,* **10,** 149 (2011).
3. I. Tokarev & S. Minko, *Soft Matter,* **5,** 511 (2009).
4. M. C. Branco, D. J. Pochan, N. J. Wagner & J. P. Schneider, *Biomaterials,* **31,** 9527 (2010).
5. K. R. Kamath & K. Park, *Adv. Drug Del. Rev.,* **11,** 59 (1993).
6. C. Vasile, *"Environmentally Degradable Materials based on Multicomponent Polmeric Systems", CRC Press,* **ASIN: B00B3W62FQ,** (2009).
7. M. Shibayama, *Bull. Chem, Soc. Jpn.* **79,** 21 (2006).
8. K. S. Anseth, C. N. Bowman & L. B. Peppas, *Biomaterials,* **17,** 1647 (1996).

9. Y. Okumura & K. Ito, *Adv. Mater.*, **13,** 485 (2001).
10. T. Sakai, T. Matsunaga, Y. Yamamoto, C. Ito, R. Yoshida, S. Suzuki, N. Sasaki, M. Shibayama & Ul. Chung, *Macromolecules,* **41,** 5379 (2008).
11. K. Haraguch, T. Tkehisa, *Adv. Mater.,* **14,** 1121 (2002).
12. J. P. Gong, Y. Katsuyama, T. Kurokawa, Y. Osada, *Adv. Matter.*, **15,** 1155 (2003).
13. M. A. Haque, G. Kamita, T. Kurokawa, T. Tujii & J. P. Gong, *Adv. Mater.*, **22,** 5110 (2010).
14. Y. Yue, T. Kurokawa, M. A. Haque, T. Nakajima, T. Nonoyama, X. Li, I. Kajiwara & J. P. Gong, *Nat. Commun.,* **5,** 4659 (2014).
15. K. Mito, M. A. Haque, T. Nakajima, M. Uchiumi, T. Kurokawa, T. Nonoyama & J. P. Gong, *Polymer,* **128,** 373 (2017).
16. D. R. King, T. L. Sun, Y. Huang, T. Kurokkawa, T. Nonoyama, A. J. Crosby & J. P, Gong, *Mater. Horiz.* **2,** 584-591 (2015).
17. Y. Huang, D. R. King, T. L. Sun, T. Nonoyama, T. Kurokawa, T. Nakajima & J. P. Gong, *Adv. Funct. Mater.* **27,** 1605250 (2017).

CHAPTER 2

Background

2.1 Composite materials

Composite materials describe in this dissertation consist of a matrix and a reinforcing phase. In nature world, there are a lot of examples wherein the idea of composite materials is used. For example, wood is a fiber reinforced composite that made of cellulose fibers (high tensile strength but very flexible) in a lignin matrix (joining fibers and furnishing the stiffness)[1]. Bone is yet another example of an organic/inorganic composite, consisting of short and soft collagen fibers embedded in a mineral matrix called apatite[2]. In addition to these natural composites, engineering materials that is used in our daily lives are full of examples for being utilized composite materials, including the carbon black in rubber, glass fibers in resin, reinforcement steel in concrete matrix[3]. Such composite material systems result in a performance unattainable by the individual components, therefore, they can enable us to make the materials more freely designable. Thus, we can see that the idea of composite materials is very common approach for creating the materials that are required efficient design, like as an aerospace structure, a vehicle, a building, and so on.

2.2 Hydrogel-based composites

With the coming of aging society, there is an expectation towards life support robots and medical supplies, which are of use in the sectors related to people’s lives that supports the safety and security such as welfare and medical care. However, those robots and supplies, including wearable device and biological materials, need to be satisfied multi-functionality such as high/anisotropic mechanical properties, stimuli-response, and high biocompatibility, which is considered to be difficult to be attained by a single materials. Therefore, aforementioned composite approach is one of the smartest idea to tailor-make the materials as per specifications of an optimum design. For designing biomaterials with multi-functions, hydrogels are one of the great candidate for using as matrix materials due to its unique properties (high water content, high flexibility, permeability, antifouling, low friction) similar to bio-tissues[4-8]. Thus, many hydrogel-based composite materials are developed so far. From here, we review the recent progress of the composites, which are divided into two categories; (1) micro-scale hydrogel composites, and (2) macro-scale hydrogel composites.

2.2.1 “Micro-scale” composites

The “micro-scale” composites described here is the size scale of reinforcing phase is about from several nanometer to several tens micrometer. We introduce typical examples of recent developments of the micro-scale composite hydrogels.

- **Double network (DN) gels**

An interpenetrating polymer network (IPN) is a polymer comprising two or more networks which are at least partially interlaced on a polymer scale but not covalently bonded to each other[9]. The network cannot be separated unless chemical or physical bonds that formed one network structure are broken. There are many example of IPN gels, among them, double network (DN) gels, consisting of an interpenetrating brittle/hard network and stretchable/soft network, exhibit noteworthy properties including high Young’s modulus and tremendous toughness despite containing high water content[10]. The profound toughness exhibited by DN gels is due to the “sacrificial bond principle”[11], where energy is dissipated by a wide range fracture of the brittle/hard network prior to rupture of the stretchable/soft network (Fig.2.1).

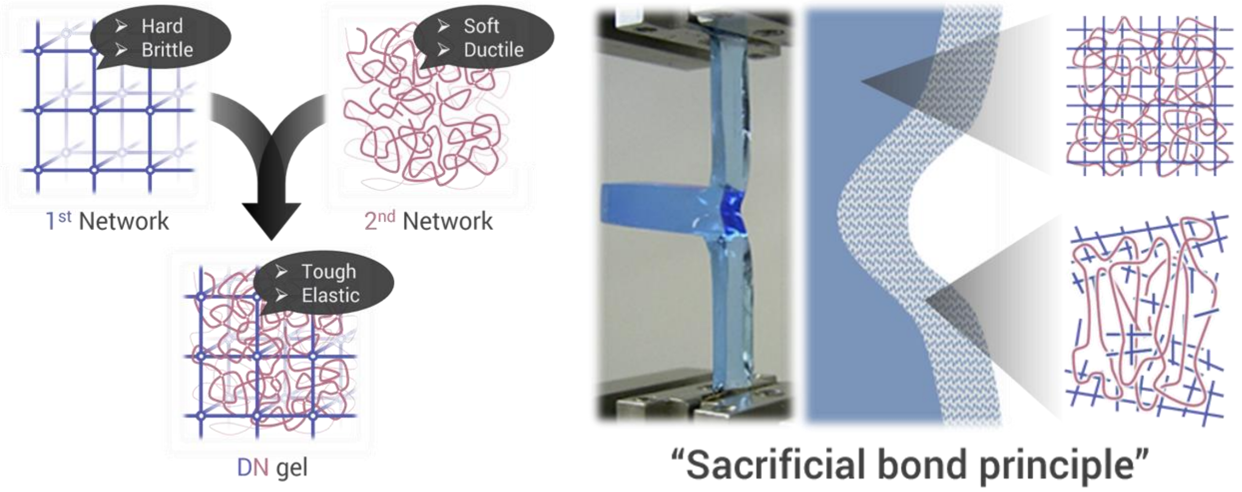

Fig.2.1| An architecture of double network (DN) hydrogels. Schematic illustration of a 1st and a 2nd networks and a sacrificial bond principle. [11, reproduced by The Royal Society of Chemistry]

DN gels perform excellent mechanical properties with conventional hydrogels. However, there are some problems for practical applications. One problem is that it is difficult to synthesized DN gels in desirable shape, caused by poor mechanical strength of the brittle/hard 1st network gels. To overcome such difficulties, particle-based double network (P-DN) hydrogels have been developed[12, 13]. P-DN gels are fabricated through a process modified from traditional DN gel synthesis. First, a hard and brittle first network is synthesized, mechanically ground into micron-sized particles, and swollen with second network monomer. After polymerization of the second network, a composite structure is formed, where the bulk second network interpenetrates the first network particles, resulting in covalently trapped double network particles inside a ductile matrix. The mechanical strength and toughness is comparable with conventional bi-continuous DN hydrogels. In addition, the fabrication process of P-DN gels is suitable for large area and free-formable coating, because the swollen first network particle "paste" can be applied freely prior to polymerization of the second network, minimizing swelling mismatch. The pre-cursor P-DN gel acts as an "ink", which enable us to obtain tough, free-formable, and large area hydrogel coatings or hydrogel 3D printings[14].

The other problem of typical DN gels are irreversible sacrificial bonds. The high toughness of DN gels comes from significant energy dissipation by the internal fracture of covalent bonds in the brittle/hard 1st network, however, permanent internal damage is induced. To remedy this difficulty, many researcher have attempted to apply recoverable physical interactions as sacrificial bonds. For example, J.-Y. Sun *et al.* synthesized a new hydrogel composites that consist of two types of crosslinked polymer: ionically crosslinked alginate and covalently crosslinked polyacrylamide[15]. Although such gels contain ~90 % water, they can be stretched beyond 20 times their initial length, have facture energies of ~9,000 Jm^{-2}, and show partial self-healing ability. H. J. Zhang *et al.* designed a novel physical DN hydrogel by two kinds of polymer: an amphiphilic triblock copolymer cross-linked by hydrophobic association and linear PAAm that can interact with triblock copolymer by hydrogen bonding[16]. The gel, which contains strong hydrophobic domains and sacrificial dynamic bonds of hydrogen bonds, is stiff and tough, and even stiffens in concentrated saline solution. Moreover, because of its supramolecular structure, the gel features improved self-healing and self-recovery abilities. These are no more than a single example of IPN (DN) gels[17-20].

As we described here, the double network concept can be utilized widely, therefore, we consider that this composite approach is one of the most useful technique to improve the mechanical properties of hydrogel, including stiffness, toughness and self-healing ability.

- **Inorganic/organic composite gels**

Recently, composite biomaterials consisting of two or more components have been developed in order to achieve synergic effects. For instance, the combination of organic (polymer) and inorganic (clay, metal oxide, carbon-based matter) structure gives these hydrogels enhanced physical, chemical, electrical, thermal, biological and swelling/de-swelling behavior that cannot be achieved by either material alone[21-24]. One typical example of such composite hydrogel proposed K. Haraguchi *et al.*, consisting of poly(*N*-isopropyl acrylamide) (PNIPA) and water-swellable inorganic clay, is called nanocomposite (NC) gel, in which the cross-linking density and the inter-crosslinking distance can be controlled independently (Fig.2.2)[25]. As a result, high stable, structurally homogeneous materials, with outstanding mechanical properties, such as superior elongation with near-complete recovery, rapid de-swelling response to temperature changes, and large equilibrium swellings were found.

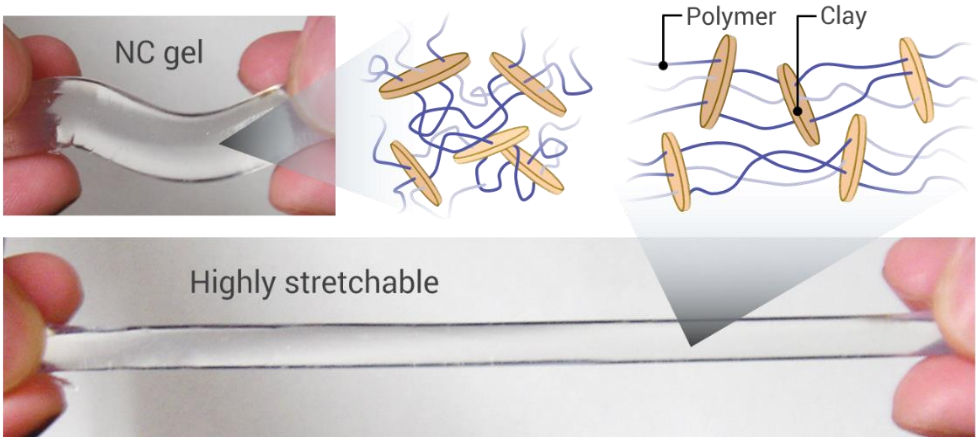

Fig. 2.2 | Schematic network architecture of nanocomposite (NC) gel. The NC gel consisting of uniformly dispersed inorganic clay and two primary types of flexible polymer: grafted on two neighboring clay sheets and one clay sheet. [25]

Furthermore, M. Liu *et al.* developed a new composite hydrogels with anisotropic mechanical properties based on an oriented architecture of an inorganic reinforcing phase[26]. They used metal oxide (Titanate) nanosheets as the inorganic reinforcement and prepared its aqueous colloidal dispersion. When the solution was placed in a strong magnetic field, the nanosheets aligned co-facially, which maximize electrostatic repulsion and thereby induces a quasi-crystalline structural ordering, over macroscopic length scales and with uniformly large face-to-face nanosheet separation. This transiently induced structural order was fixed by transforming the dispersion into a hydrogel using light-triggered *in situ* vinyl polymerization. As a result, the hydrogel, containing charged inorganic structures that align co-facially in a magnetic flux, deforms easily under shear forces applied parallel to the embedded nanosheets yet resists compressive forces applied orthogonally. This and related works are the fascinating examples of emergence of functions based on specific architectures in composite gels[27].

Needless to say, the composite approach enable hydrogels to introduce functions that are originated from the reinforcing phase. The electrical and thermal conductivity and magnetic property of metals (or carbon-based materials) enhance the electrical conductivity and antibacterial property of nanocomposites hydrogels when incorporated[28, 29]. The electrical conducting property is important for the hydrogels to design functional tissues and be used as imaging agents, drug delivery systems, conductive scaffolds, switchable electronics, soft actuators and sensors. There are so many papers described such hydrogel composites functionalized by unique properties of reinforcing phase. Besides this, recent discovery of inorganic/organic composite hydrogels, consisting of hydrogel matrix and biocompatible minerals such as calcium phosphate, is excellent candidate for using as tough implants or bio tissues. N. Rauner *et al.* report an enzyme-induced formation of amorphous calcium phosphate nanostructures that are homogeneously distributed within polymer hydrogels[30]. One best materials exhibit fracture energies of 1300 J/m^2 and stiffness up to 440 MPa, even in their fully water-swollen state. Furthermore, T. Nonoyama *et al.* developed a new strategy to bond a tough hydrogel to bone by using the hydroxyapatite (HAp) coated DN gel[31]. The HAp and the DN gel matrix composite layer show high osteoconductivity, which leads to spontaneously induce the formation of a strong gel-bone interface in vivo. These works will be a giant step for the practical applications of tough hydrogels as substitutes of soft supporting tissues.

- **Organic/organic composite gels**

Supramolecules, including micelle (bilayer), rotaxane, and liquid crystal, embedded in a hydrogel matrix is classified as organic/organic composite gels in this dissertation. Due to its high ordered structures of supramolecules, we can introduce unique functionalities to hydrogel based on the structures. For example, Md. A. Haque *et al.* developed a novel anisotropic hydrogel, consisting of lamellar bilayers (reinforcing phase) and a polymer network (matrix phase), with unidirectional alignment of the bilayer structure (Fig.2.3a)[32]. This unique architecture of the reinforcing phase leaded to one-dimensional swelling, high toughness base on energy dissipation, strong anisotropy in elastic modulus, and exhibited bright visible color. In addition to this, the gel showed reversibly and rapidly tunable structural color under mechanical, chemical, thermal stimulations and could have a great potential for using as new class of color display or stimulus sensor[33, 34].

One of the smartest idea of using unique architectures of supramolecules for a new functionality is slide-ring gel (topological gel) developed by K. Ito *et al.*[35]. In this gel, polymer chains with bulky end groups exhibit neither covalently cross-links as in chemical gels nor attractive interactions as in physical gels but are topologically interlocked by figure-of-eight cross-links based on the rotaxane structure (Fig.2.3b). Therefore, these cross-links can pass along the polymer chains freely to moderate the tension of the threading polymer chains similarly to pulleys, which is called the “pulley effect”. Based on this mechanism, the hydrogel exhibits unique mechanical properties (low elastic modulus, low stress relaxation, etc.) that similar to biotissues, thus, it has a great potential for practical use[36].

In recent years, biomimetic and bioinspired hydrogels have received increasing attention due to their multi-functions, high toughness, and potential applications in tissue engineering. These functions are related to a high degree of architectures that is formed by self-organization of the various components into oriented and hierarchical structures. Thus, liquid crystalline molecules, which have a self-organizing functions, are often used to develop self-assembled architectures in physically or chemically cross-linked hydrogel matrix[37, 38]. Y. Shigekura, *et al.* developed a novel anisotropic gel that is an anionic liquid crystalline polymer embedded in a cationic polymer gel matrix (Fig.2.3c)[39]. The liquid crystalline polymer, a water-soluble, rigid rod-like, synthetic polyelectrolyte, is called PBDT (poly(2,2'-di-sulfonyl-4,4'-bensidine terephthalamide)). In this gel, a small amount of PBDT was added as dopant and the gel exhibited complicated yet high-ordered birefringence pattern based on the orientation of PBDT. Therefore, combining this liquid crystalline polymer with hydrogel matrix is to be considered that a new way to introduce optical anisotropy into synthesized gels. Furthermore, intense efforts have been devoted for understanding and controlling such intricate PBDT architectures[40-42], however, effective approach is still a mystery.

So far, we introduced several types of micro-scale hydrogel composites. There are so many successful examples for introducing functions based on the properties of reinforcing phases but a few examples are reported that the functions are related to the architecture of reinforcing phases. Therefore, the liquid crystalline polymer composite system, which has a great potential for building up complex and hierarchical architectures similar to biological tissue, is chosen and polished up in this dissertation.

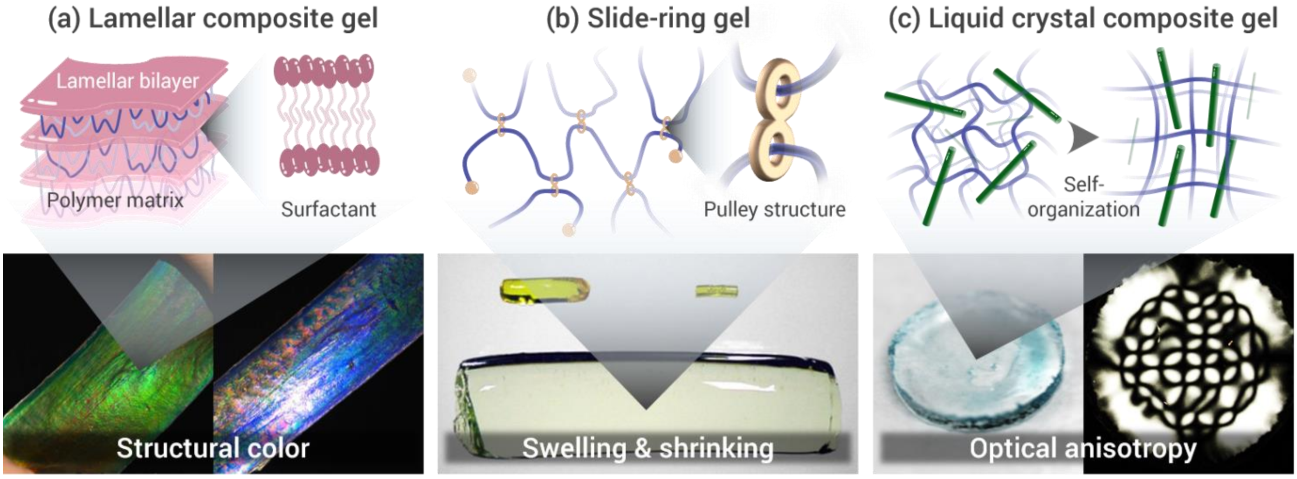

Fig. 2.3 | Various types of organic/organic composite gels. (**a**) Schematic illustration of lamellar bilayer composite gels and the structural color based on Bragg's diffraction. (**b**) Schematic illustration of slide-ring gel. [35] (**c**) Schematic illustration of liquid crystalline polymer composite gels. A photograph (black) represents the intricate birefringence pattern of liquid crystalline polymer.

2.2.2 “Macro-scale” composites

The “macro-scale” composites described here is the size scale of reinforcing phase is about from several hundreds micrometer to several tens millimeter. We introduce typical examples of recent developments of the macro-scale composite hydrogels.

- **Adhesion of hydrogels on solid materials**

Hybrid combinations of hydrogels and solid materials are strongly required for practical applications of hydrogels in diverse fields. A simple yet versatile method for fabricating hydrogel-solid material composites is adhesion of hydrogels. However, in general, hydrogels exhibit low adhesion to solid materials due to their high water content and poor mechanical properties. Although hydrogel with extraordinary physical properties have been recently developed, the weak and brittle interface between hydrogels and solid materials often severely prevents their integration and function in devices and systems. There have been a few attempts to form a robust interface between hydrogels and substrates[43-45]. For example, our group has proposed a method for binding a tough DN hydrogel to a porous solid, utilizing the double-network principle[44]. Under optimal conditions, the bonding strength approaches ~1000 N/m, which is comparable with the fracture strength of bulk DN gels. Furthermore, recently, H. Yuk *et al.* reported a method to strongly bond synthetic hydrogels to non-porous surfaces of diverse solids, including glass, silicone, ceramics, titanium and aluminum[45]. The design strategy is to anchor the long-chain polymer networks of tough hydrogels covalently to non-porous solid surfaces, which can be modified by the silanation of such surfaces. Taking advantage of the high toughness of viscoelastic hybrid gels, the chemical anchorage resulted in a high intrinsic work of adhesion and strong interfacial toughness values of over 1000 N/m, approaching the toughness of the gel itself. These work open new avenues to practical applications of robust hydrogel-solid macro-scale composite in biomedical, soft electronics, soft robotics, and so on.

- **Fiber-reinforced hydrogel composites**

Fiber-reinforced composites consist of fibers of high tensile-strength and modulus embedded in or bonded to a matrix with robust interfaces between them. In this system, both fibers and matrix retain their physical and chemical features, yet they produce a combination of properties that cannot be achieved with either of the constituents acting alone. Basically, fibers act as load-carrying members, while the surrounding matrix keeps them in the desired location and orientation, act as load transfer medium between them, and protects them from environmental damages induced by elevated temperatures, humidity, and ultraviolet light[46]. Therefore, even though the fibers provide reinforcement for the matrix, the latter also provides a number of useful functions in a fiber-reinforced composites.

In general, conventional hydrogels are weak and brittle, it is difficult to use as matrix materials in fiber-reinforced composites: as the composite is loaded, the fibers cut through the hydrogel matrix easily, destroying the synergy between fibers and matrix, and leading to rapid rupture of the composite. However, over the past decade, vast number of tough hydrogels have been developed, and they enable to fabricate fiber-reinforced composite gels. W. R. K. Illeperuma *et al.* developed a composite using the aforementioned alginate-polyacrylamide hydrogel reinforced with a random network of stainless steel fibers[47]. Before rapture the composite dissipates a significant amount of energy, at a tunable level of stress, attaining large deformation. Furthermore, D. R. King *et al.* fabricated a new composites, consisting of tough, adhesive and deswellable polyampholyte hydrogels[48] and glass fiber woven fabrics, exhibit extremely high effective toughness, high tear strength, high tensile modulus and low bending modulus (Fig.2.4a)[49]. Even though these composites contain 40% water (in a volume ratio), their mechanical properties are far superior to those of the neat components, indicating a synergistic effect (Fig.2.4b)[50]. This work provide a simple route to develop extremely tough and biocompatible soft materials and also should merit for potential applications such as energy-absorbing helmets, tendon repair surgery, and stretchable biometric sensors.

So far, we introduced a few examples of macro-scale hydrogel composites. This research field has been developed rapidly in the past few years, therefore, there are some limitations for fabricating the macro-scale composite gels. In general, the volume of hydrogels can change dramatically from the as-prepared state by expelling water to or absorbing water from the environment, causing the hydrogel-solid composite to undergo stress concentration resulting in surface creasing, bulk deformation and interfacial delamination[51-53]. To avoid such stress concentration, the matrix materials are highly limited in the previous research; mechanically tough and relatively low-swelling hydrogels are required[15, 48]. Therefore, in this dissertation, a universal strategy and practical method for fabricating diverse hydrogel-based composites is investigated for versatile applications.

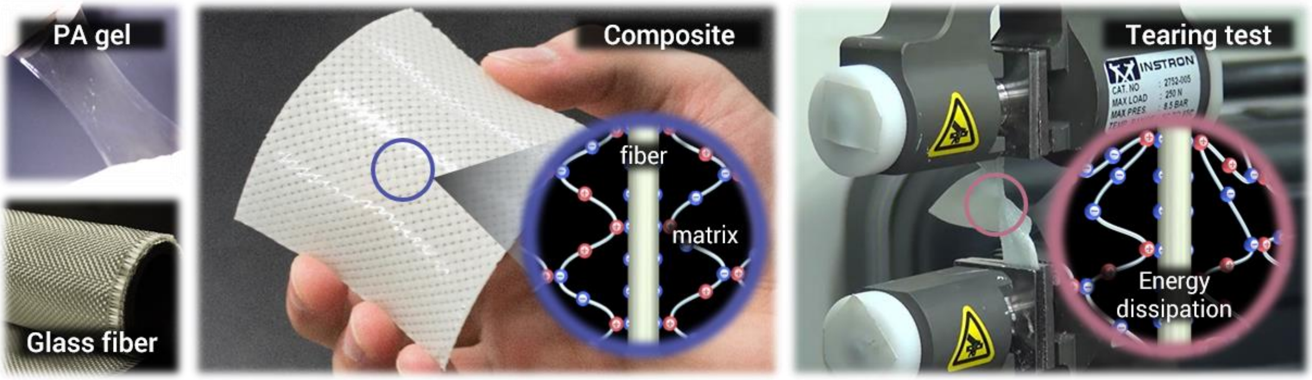

(a) Glass-fiber PA gel composites (b) Toughening mechanism

Fig. 2.3 | Extremely tough fiber-reinforced hydrogel composites. (**a**) Schematic illustration of each components of the composites. Due to the self-adjustable adhesion property of PA gel, strong electro-static interaction between glass-fibers and PA matrix is formed. [50, Published by The Royal Society of Chemistry] (**b**) A snapshot of the composite gel during tearing test. The glass-fiber transfer the load to PA gel matrix and the PA gel dissipate significant energy due to a large amount of sacrificial bonds (ionic interactions). As a result, the composite exhibit extremely high toughness despite of water-swollen state. [49]

2.3 References

1. S. Weiner & H. D. Wagner, *Annu. Rev. Mater.*, **28,** 271 (1998).
2. M. Elices, *"Structural biological materials", Pergamon Press, Amsterdam Schier JF, Juergenes RJ,* **21,** 44 (2000).
3. K. K. Chawla, *"Composite Materials: Science and Engineering (Materials Research and Engineering)", Springer,* **ISBN: 0387743642,** (2012).
4. Q. Wang, J. L. Mynar, M. Yoshida, E. Lee, M. Lee, K. Okuro, K. Kinbara & T. Aida, *Nature,* **463,** 339 (2010).

5. T. Sakai, Y. Akagi, T. Matsunaga, M. Kurakazu, U. Chung & M. Shibayama, *Macromole. Rapid Commun.,* **31,** 6072 (2010).
6. J. Honiger, P. Balladur, P. Mariani, Y. Calmus, M. Vaubourdolle, R. Delelo, J. Capeau & B. Nordlinger, *Biomaterials,* **16,** 753 (1995).
7. S. Q. Liu, C. Yang, Y. Huang, X. Ding, Y. Li, W. M. Fan, J. L. Hedrick & Y.- Y. Yang, *Adv. Mater.,* **24,** 6484 (2012).
8. D. Kaneko, T. Tada, T. Kurokawa, J. P. Gong, Y. Osada, *Adv. Mater.,* **17,** 535 (2005).
9. J. V. Aleman, A. V. Chadwick, J. He, M. Hess, L. Horie, R. G. Jones, P. Kratochvil, I. Meisel, I. Mita, G. Moad, S. Penczek & R. F. T. Stepto, *The Sci. J. IUPAC,* **79,** 10 (2007).
10. J. P. Gong, Y. Katsuyama, T. Kurokawa, Y. Osada, *Adv. Matter.,* **15,** 1155 (2003).
11. J. P. Gong, *Soft Matter,* **6,** 2583 (2010).
12. J. Hu, K. Hiwatashi, T. Kurokawa, S. M. Liang, Z. L. Wu & J. P. Gong, *Macromolecules,* **44,** 7775 (2011).
13. J. Saito, H. Furukawa, T. Kurokawa, R. Kuwabara, S. Kuroda, J. Hu, Y. Tanaka, J. P. Gong, N. Kitamura & K. Yasuda, *J. Polymer Chem.,* **2,** 575 (2011).
14. H. Muroi, R. Hidema, J. Gong & H. Furukawa, *J. Solid Mech. Mater. Enginer.,* **7,** 163 (2013).
15. J. Y. Sun, Z. Zhao, W. R. K. Illeperuma, O. Chaudhuri, K. H. Oh, D. J. Mooney, J. J. Vlassak & Z. Suo, *Nature* **489,** 133-136 (2012).
16. H. Zhang, T. L. Sun, A. Zhang, T. Nakajima, T. Nonoyama, T. Kurokawa, O. Ito, H. Ishitobi & J. P. Gong, *Adv. Mater.,* **28,** 4884 (2016).
17. A. Nakayama, A. Kakugo, J. P. Gong, Y. Osada, M. Takai, T. Erata & S. Kawano, *Adv. Funct. Mater.,* **14,** 1124 (2004).
18. S. Naficy, J. M. Razal, P. G. Whitten, G. G. Wallace & G. M. Spinks, *J. Poly. Sci. Part B,* **50,** 423 (2012).
19. Q. Chen, L. Zhu, C. Zhao, Q. Wang, J. Zheng, *Adv. Mater.,* **25,** 4171 (2013).

20. L. Weng, A. Goyldstone, Y. Wu & W. Chen, *Biomaterials,* **29,** 2153 (2008).
21. P. Huang, W. Chen & L. Yan, *Nanoscale,* **5,** 6034 (2013).
22. V. Pardo-Yissar, R. Gabai, A. N. Shipway, T. Bourenko & I. Willner, *Adv. Mater.,* **13,** 13320 (2001).
23. R. Ananthoji, J. F. Eubank, F. Nouar, H. Mouttaki, M. Eddaoudi & J. P. Harmon, *J. Mater. Chem.,* **21,** 9587 (2011).
24. J. Wang, L. Lin, Q. Cheng & L. Jiang, *Angew. Chem.,* **124,** 4754 (2012).
25. K. Haraguch, T. Takehisa, *Adv. Mater.,* **14,** 1121 (2002).
26. M. Liu, Y. Ishida, Y. Ebina, T. Sasaki, T. Hikima, M. Takata & T. Aida, *Nature,* **517,** 68 (2015).
27. Y. S. Kim, M. Liu, Y. Ishida, Y. Ebina, M. Osada, T. Sasaki, T. Hikima, M. Takata & T. Aida, *Nat. Mater.* **14,** 1002 (2015).
28. V. Thomas, M. M. Yallapu, B. Sreedhar & S. K. Bajpai, *J Colloid Inter. Sci.,* **315,** 389 (2007).
29. Y. Xu, K. Sheng, C. Li & G. Shi, *ACS nano,* **4,** 4324 (2010).
30. N. Rauner, M. Meuris, M. Zoric & J. C. Tiller, *Nature,* **543,** 407 (2017).
31. T. Nonoyama, S. Wada, R. Kiyama, N. Kitamura, Md. T. I. mredha, X. Zhang, T. Kurokawa, T. Nakajima, Y. Takagi, K. Yasuda & J. P. Gong, *Adv. Mater.,* **28,** 6740 (2016).
32. M. A. Haque, G. Kamita, T. Kurokawa, T. Tujii & J. P. Gong, *Adv. Mater.,* **22,** 5110 (2010).
33. Y. Yue, T. Kurokawa, M. A. Haque, T. Nakajima, T. Nonoyama, X. Li, I. Kajiwara & J. P. Gong, *Nat. Commun.,* **5,** 4659 (2014).
34. Y. Yue, X. Li, T. Kurokawa, M. A. Haque & J. P. Gong, *J. Mater. Chem. B,* **4,** 4104 (2016).
35. Y. Okumura & K. Ito, *Adv. Mater.,* **13,** 485 (2001).
36. K, Ito, *Polymer Journal,* **39,** 489 (2007).
37. T. Kato, N. Mizhoshita & K, Kishimoto, *Angew. Chem., Int. Ed.,* **45,** 38 (2006).
38. C. L. Lester, S. M. Smith & C. D. Colson, *Chem. Mater.,* **15,** 3376 (2003).
39. Y. Shigekura, Y. M. Chen, H. Furukawa, T. Kaneko, D. kaneko, Y. Osada & J. P. Gong, *Adv. Mater.,* **17,** 2695 (2005).
40. Z. L. Wu, T. Kurokawa, S. Liang, H. Furukawa & J. P. G. *J. Am. Chem. Soc.,* **132,** 10064 (2010).

41. M. Arifuzzaman, Z. L. Wu, T. Kurokawa, A. Kakugo & J. P. Gong, *Soft Mater.*, **8,** 8060 (2012).
42. M. Arifuzzaman, Z. L. Wu, R. Takahashi, T. Kurokawa, T. Nakajima & J. P. Gong, *Macromolecules,* **46,** 9083 (2013).
43. H. Yuk, T. Zhang, G. A. Parada, X. Liu & X. Zhao, *Nat. Commun.* **7,** 12028 (2016).
44. T. Kurokawa, H. Furukawa, W. Wang, Y. Tanaka & J. P. Gong, *Acta Biomaterialia,* **6,** 1353 (2010).
45. H. Yuk, T. Zhang, S. Lin, G. A. Parada & X. Zhao, *Nat. Matter.*, **15,** 190 (2016).
46. P. K. Mallick, *"Fiber-Reinforced Composites: Materials Manufacturing, and Design", CRC Press,* **ISBN: 9781420005981** (2007).
47. W. R. K. Illeperuma, J.-Y. Sun, Z. Suo & J. J. Vlassak, *Extreme Mechanics Letters,* **1,** 90-96 (2014).
48. T. L. Sun, T. Kurokawa, S. Kuroda, A. B. Ihsan, T. Akasaki, K. Sato, Md. A. Haque, T. Nakajima & J. P. Gong, *Nat. Mater.* **12,** 932-937 (2013).
49. D. R. King, T. L. Sun, Y. Huang, T. Kurokkawa, T. Nonoyama, A. J. Crosby & J. P, Gong, *Mater. Horiz.* **2,** 584-591 (2015).
50. Y. Huang, D. R. King, T. L. Sun, T. Nonoyama, T. Kurokawa, T. Nakajima & J. P. Gong, *Adv. Funct. Mater.* **27,** 1605250 (2017).
51. V. Trujillo, J. Kim & R. C. Hayward, *Soft Matter,* **4,** 564 (2008).
52. Zhang, X. C. L. Pint, M. H. Lee, B. E. Schubert, A. Jamshidi, K. Takei, H. Ko, A. Gillies, R. Bardhan, J. J. Urban, M. Wu, R. Fearing & Ali, Javey, *Nano Letters* **11,** 3239-3244 (2011).
53. M. Y. Kim, B. Jung & J.-H. Park, *Biomaterials* **33,** 668-678 (2012).

CHAPTER 3

Control of Semi-Rigid Polymer Structures Embedded in Hydrogel Matrix via Tunable Swelling

3.1 Introduction

Hydrogels are 3D networks of hydrophilic polymers that can absorb a large amount of water while maintaining the structure. Recent developments of tough hydrogels[1-3] have vastly expanded the applications of this material in diverse fields, such as soft robotics, artificial organs, drug delivery system, and etc4[-9]. Beyond the toughness, one of the next challenges is how to introduce *long-range* superstructures into isotropic and amorphous hydrogels matrix. Many specific functions of biological soft tissues are strongly related to the superstructures of semi-rigid, fiber-forming molecules. For example, rigid collagen fibers in the articular cartilage align parallel to the sliding surface but perpendicular to the interface with bone[10-12]. These superstructures of collagen fibers are considered that they play an important role for the functions of cartilages, including high impact absorbance, low sliding friction and strong bonding to bone[13-15]. These natural systems with spatially intricate superstructures provide us elegant paradigms in designing new biomimetic materials with specific functions and promising applications. However, developing programmable *long-range* superstructure in hydrogels matrix is a non-trivial aim, because the bottom-up approach of self-assembly no longer works. Many efforts have been made to induce uni-axial polymer orientation in hydrogel matrix, for example, by shear, by electric or magnetic fields[16-21]. These methods are not straightforwardly applicable to develop complicated *long-range* superstructure in the hydrogel matrix, and alternative strategies are definitely required.

In this chapter, we report a novel strategy to develop hydrogel composites with *long-range* superstructures from a semi-rigid polymer by playing with programmed internal stress. When a soft hydrogel has a swelling mismatching in different regions, an internal stress develops at the interface. The internal stress can align semi-rigid polymers directly. In this study, we applied photolithographic technology to induce programmed swelling mismatching in the positively charged hydrogel (Fig.

3.1a,b)[22,23]. Considering a slab of hydrogel with alternative stripes of different swelling, the large swelling region is compressed by the less swelling region. Oppositely, the less swelling region is stretched by the large swelling region. If semi-rigid polymers are embedded in the hydrogel matrix (which is micro-scale hydrogel composites), they intend to orient along the tensile direction while they orient perpendicular to the compressive direction (Fig. 3.1c). This internal-stress-directed orientation of semi-rigid polymers inside the hydrogel matrix has recently been demonstrated[24-26]. When both of the embedded semi-rigid polymer and the hydrogel matrix are polyelectrolytes but carry opposite charges, the orientation can be "memorized" by polyion complex formation by the dialysis of their counter-ions[25,26]. Therefore, various superstructures of semi-rigid polyelectrolytes could be formed in oppositely charged polymeric hydrogel matrix by harnessing internal-stress-directed orientation of rigid macromolecules. Furthermore, by using double network concept[1], we developed tough double network hydrogels with programmed superstructures. This work gives a pathway to synthesize tough hydrogel composites with complex superstructures and should merit designing other biomimetic materials towards specific functions.

3.2 Experiments

5.2.1 Materials

PBDT, a water soluble anionic semi-rigid polyelectrolytes, was synthesized by an interfacial poly-condensation reaction. The synthesized PBDT had an average molecular weight, M_w of about 200,000 g•mol^{-1}, number average molecular weight, M_n of about 150,000 g•mol^{-1}, and polydispersity ($M_\mathrm{w}/M_\mathrm{n}$) of about 1.4, as measured by size exclusion chromatography-multi angle light scattering (SEC-MALS, L-6000 HPLC, Hitachi as pump and injector, SB-805HQ, Showa Denko as column, DAWN Heleos as static light scattering, Optilab rEX as refractive index detector) with 0.1 M Na_2SO_4 as the elution solvent (Fig. 3.5). Its aqueous solution showed a critical low liquid crystalline concentration, C_LC^* of 2.8 wt%. The cationic monomer, *N*-[3-(*N,N'*-dimethylamino)propyl]acrylamide methyl chloride quaternary (DMAPAA-Q) (Kohjin Co. Ltd., Japan), the photo-initiator, 2-oxoglutaric acid

(OA) (Wako Pure Chemical Industries Ltd., Japan), were used as received without further purification. Acrylamide (AAm) (Junsei Chemical Co. Ltd., Japan) was recrystallized from chloroform. *N,N'*-methylenebis(acrylamide) (MBAA) (Wako Pure Chemical Industries Ltd., Japan) was recrystallized from ethanol and used as a chemical cross-linker. For all experiments, water was deionized and purified with 0.22 μm and 5 μm membrane filter prior to use.

5.2.2 Synthesis of semi-rigid polymer (PBDT)

PBDT was prepared by an interfacial poly-condensation reaction, as described in Scheme 3.1. 11g of sodium carbonate was dissolved in 140 ml of deionized water in a flask. The mixture was stirred carefully, then, 12.7 g of purified diaminobenzidine disulfonate (benzidine-2,2'-disulfonic acid (BDSH)) was obtained. A second solution was prepared by adding 1 g of poly(ethylene glycol) distearate with M_n =930 as a surfactant to 5 ml of purified tetrahydrofuran (THF) and added to the former solution. After 30 min dramatic stirring, the speed slowed down. A third solution was prepared of 5.23 g of purified terephthaloyl chloride (TPC) in 100 ml of purified chloroform and dropped into the above mixture within 3 h. The stirring with a slow speed continued for 6 h to complete the reaction.

The product with high viscosity was precipitated with 3000 ml of acetone and filtered using a Buchner funnel. It was redissolved in 120 ml of pure water, again precipitated with 1500 ml of acetone, and filtered. The procedure was followed twice more to five polymer free of carbonate and chloride salts. The wet polymer was dried at 40°C to five a white fibrous solid at about 80 % yield.

5.2.3 Synthesis of hydrogels with programmed swelling mismatch

To synthesize hydrogel film with programmed swelling mismatching, photolithographic technique was adopted. The reaction cells were prepared by sandwiching the square frame of a silicone spacer (thickness: 1 mm) between two parallel glass plates. Then, two photo-masks with the same pattern prepared by Overhead projector films (OHP films) (KOKUYO Co. Ltd., Japan) were gripped on two sides of the reaction cell in phase, to guide the progress of photo-polymerization at specific regions (Fig. 3.1a). The aqueous precursor solutions contained 1.0 wt% of the PBDT, 2.0 M of the DMAPAA-

Q, 2.0 mol% of the MBAA, and 0.15 mol% of the OA. The amount in mol% was relative to the DMAPAA-Q concentration. After proper mixing, the precursor solution was injected into the reaction cells. As-prepared gels were obtained after UV irradiation from the both sides of the reaction cell (UV light intensity was 3.9 mW•cm^{-2}) for 7.5 h under an argon atmosphere at room temperature. By using masks with different patterns described in Fig. 3.3, gels with different programmed swelling mismatching were obtained. The as-prepared gels were swelled in a large amount of water for several days to achieve the equilibrium state.

5.2.4 Synthesis of tough double network hydrogels with superstructures

The PBDT-containing PDMAPAA-Q gel was used as the first network, and polyacrylamide (PAAm) was used as the second network. The as-prepared PBDT-containing PDMAPAA-Q gel was immersed in precursor solution of the second network (4 M acrylamide monomer, 0.01mol% MBAA, and 0.01mol% OA) for 2 days until reaching equilibrium. Then the second network was formed by UV irradiation for 10 h[29]. The as-prepared double network gels were swelled in water for several days to allow gels to reach the equilibrium state.

5.2.5 Optical observation of superstructures

The surface morphology and the birefringence of the gels in the as-prepared state and the equilibrium swelling state were observed under a polarizing optical microscope (POM) (Nikon, Eclipse, LV100POL) in the parallel and crossed polarization modes, respectively, at room temperature. Sample gels were placed on glass slides and observed from the top (Fig. 3.2a and 3.2c) or side (Fig. 3.2b and 3.2d). All the samples of PBDT-containing PDMAPAA-Q gel exhibited a first order white-gray birefringence color. To identify the molecular orientation direction, a 530 nm sensitive tint plate was inserted[25-27]. PBDT has a positive birefringence and PDMAPAA-Q has a negative birefringence. At the prescribed condition in this study, the birefringence intensity of PBDT surpasses that of PDMAPAA-Q[24,25]. So the birefringence color observed is governed by the PBDT orientation.

The birefringence patterns of gels in the equilibrium swelling state were also observed under optical microscope (OLYMPUS, SZX12) with circular polarizer plate (MeCan Imageing Inc., Saitama, Japan) at room temperature. Sample gels were sandwiched between clockwise and counterclockwise circularly polarizing plates and observed from the top (Fig. 3.3b). The highly oriented parts in the patterned gel exhibited a white-gray birefringence color regardless of orientation direction[30,31].

5.2.6 Linear dichroism measurements of a swollen stripe-patterned hydrogel

Linear dichroism (LD) measurements were performed on the swollen PBDT-containing PDMAPAA-Q gel with stripe-pattern by using a Photonic Multi-Channel Analyzer C10027 (Hamamatsu Photonics K.K., Japan). In order to make polarized UV light (wavelength range: 200~400 nm), LIGHTNINGCURE^{TM} (Hamamatsu Photonics K.K., Japan) was used as a light source, UV Bandpass Filter UG-11 (Edmund Optics Inc.) was used as a filter, and UV-vis polarized filter (OPT-LINE, Inc.) was used as light polarizer. The masked region and unmasked region were irradiated with the spot of the light, and the absorbance of the polarized UV light which is perpendicular or parallel to the stripe pattern were measured (Fig. 3.10). A_x and A_y are the absorbance of polarized UV light along with x-axis and y-axis defined in Supplementary Fig. 3.10, respectively.

5.2.7 Tensile experiments

The tensile stress-strain measurements were performed on water-swollen DN gels using a tensile-compressive tester (Tensilon RTC-1310A, Orientec Co.). The patterned DN gel sheet was cut into specific dimensions (length: 20 mm; width: 15mm; height: 3 mm) and stretched along the length direction of the samples at an extension rate of 100 mm/min. Tensile strain, ε, is defined as $(L-L_0)/L_0$, in which L_0 and L are the length of the gel before and during elongation, respectively. The pictures and movies during tensile test were taken by a digital camera. To show the birefringence pattern, the movies were taken under crossed polarizers without (in this situation, the background color is black) and with (in this situation, the background color is purple) 530 nm tint plate to determine the orientation of PBDT molecules.

3.3 Results & discussion

3.3.1 Superstructure formation in hydrogel matrix

The composite gel containing a semi-rigid polymer was synthesized by polymerizing the precursor aqueous solution containing prescribed amount of the *rigid* polyanion PBDT, cationic monomer DMAPAA-Q, chemical cross-linker, and photo-initiator (see Scheme 3.2). Two identical photo masks of stripe pattern were placed in phase on the surfaces of the reaction cell, composed of two pieces of glass plates separated by a silicone spacer of 1 mm in thickness, to guide the photo-initiated polymerization and gelation process, which built a composition gradient in the gel (Fig. 3.1a,b). It took 7.5 h to finish the gelation in both the masked and unmasked regions and to obtain an integrated piece of gel strong enough for handling.

The as-prepared gel was transparent with a periodical groove pattern of thickness undulation, where thin parts were located in the middle of masked regions, as shown in Fig. 3.2a (top view) and Fig. 3.2b (side view). The boundary of the thin parts and thick parts did not coincide with that of the mask, but inside the masked region, 0.7 mm from the masking boundary, due to the non-parallel irradiation of the UV light and the diffusion of reactive species (monomer, cross-linker and initiator) during the reaction (Fig. 3.6 and Fig. 3.7). For simplicity, however, we called the thin part as the masked region, and the thick part as the unmasked region in the later text. Under polarizing optical microscope (POM), the sample showed strong birefringence in masked regions, as observed from top of the sample (Fig. 3.2a-ii). However, when observed from cross section of the sample, the central layer of unmasked regions showed birefringence (Fig. 3.2b-ii). The birefringence of the gel comes from both PBDT that has a positive birefringence and PDMAPAA-Q that has a negative birefringence. Previous study has shown that PBDT has a much strong birefringence than PDMAPAA-Q and the net birefringence observed here is related to the orientation of the semi-rigid PBDT molecules[25-27]. From the birefringence color observed with 530 nm sensitive tint plate (Fig. 3.2a-iii and Fig. 3.2b-iii), we identified that PBDT aligns parallel to the stripes in the masked regions (Fig. 3.2a-iv) and aligns parallel to the gel surface yet without in-plane directional preference in the central layer of unmasked regions (Fig. 3.2b-iv). As the gel was synthesized at a PBDT concentration (1 wt%) lower than its critical liquid crystalline concentration (C_{LC}^{*} = 2.8 wt%), this result indicates that internal stress built during the gelation directs the orientation of PBDT. During the synthesis of sheet-shape gel by photo-polymerization, both surface layers of the sample have a faster reaction speed, resulting in composition gradient in the gel thickness direction. The gelation at the central layer is relatively slow to freeze the complexation process, which leads to localized volume contraction to some extent. As a result, the central layer of the gel is stretched by the surface layers, and PBDTs align along with the stretching stress, i.e., parallel to the gel surface.

After swelling, the masked regions have a higher swelling ability than the unmasked region. Both regions showed strong birefringence, yet with different colors, indicating the different orientations of PBDT, as illustrated in Fig. 3.2c. The PBDT in the masked regions oriented vertical to the stripes direction while it oriented parallel to the stripes direction in the unmasked regions. The alignment of PBDT was also confirmed by side view of the samples (Fig. 3.2d and Fig. 3.8).

We should notice that the birefringence of masked regions changed from blue of as-prepared gel to orange of the swollen gel (Fig. 3.2a and 3.2c), indicating a reversion of PBDT alignments. This reversion of PBDT orientation is related to the change of the internal stress field by the swelling. Before swelling, the thicknesses of the masked and unmasked regions of the as-prepared gels were 0.7 mm and 0.9 mm, respectively. Thus, the masked regions, having a low swelling ability, experience a tension from the unmasked regions (Fig. 3.2b). As a result, the PBDT molecules in the masked regions aligned parallel to the boundary. However, after swelling, the masked regions have a higher swelling ability than the unmasked region (Fig. 3.2d). So this region receives a compression along the boundary and PBDT molecules convert the orientation in the direction perpendicular to the boundary. On the other hand, the unmasked region, which has less swelling ability, receives a tension along the boundary that directs the PBDT molecules to align with this tensile direction. The gel shows a global anisotropic swelling, with slightly large swelling in the direction vertical to the stripes.

The swelling of the hydrogel in pure water removes the paired small counter-ions of the oppositely charged polyelectrolytes from the gel matrix (dialysis effect), and therefore, the orientation of PBDT directed by internal stress in the hydrogel was “memorized” by polyion complex formation. As the polymer matrix is in excess of its mass than that the PBDT, a large ionic osmotic pressure still exists to swell the gel substantially. We confirmed that the superstructure was maintained even after releasing of the internal stress by slicing the masked and unmasked regions into separate stripes (Fig. 3.9).

3.3.2 Further characterization of superstructures in hydrogel matrix

In addition to the POM observation, we also characterized the localized molecular alignments in the gels using linear dichroism (LD) measurements. In both the masked and unmasked regions, a very strong absorbance appears in the 300~350 nm wavelength range (Fig. 3.10), which is attributed to the absorbance of PBDT that shows strong absorbance to UV light with a wavelength less than 360 nm.[27] This peak is assigned to the carbonyl group and phenyl group and it is red-shifted by delocalization of π-electron and bathochromic effect in a PBDT molecule.[35] However, PDMAPAA-Q only shows very weak absorbance at the range of 300~400 nm (data not shown), so we could not identify the signal from PDMAPAA-Q. As for the masked region, a negative peak of the A_x-A_y spectrum appears around 354 nm (the green line in Fig. 3.10a). Phenyl group of PBDT has a symmetric chemical structure and shows direction-independent absorbance, whereas carbonyl group has an asymmetric structure and direction-dependent absorbance. Therefore, the negative peak of A_x-A_y spectrum around 354 nm should stem from the carbonyl group of oriented PBDT molecules, indicating that these carbonyl groups preferentially oriented along with the y-axis. Considering its chemical structure, PBDT therefore aligns along with x-axis (i.e. perpendicular to the stripe direction). As for unmasked region, in contrast, a positive peak of the A_x-A_y spectrum appears around 347 nm (the green line in Fig. 3.10b), indicating that carbonyl groups of PBDT orient along with the x-axis. As a result, PBDT aligns parallel to the stripe direction. The PBDT alignments measured by LD spectroscopy are consistent with results of POM observation (Fig. 3.2c).

As the absorbance shown in Figure 3.10 was too strong and they were partially saturated, we could not accurately determine the orientation degree from these spectrum results. However, for a simple and rough comparison, we estimated the orientation degree between the masked and unmasked regions, Dichroic ratio, R = $\frac{Ax-Ay}{Ax+Ay}$, using the difference spectrum peak of A_x-A_y. R in the masked and unmasked regions was -0.21 and 0.11, respectively, indicating a better orientation of PBDT molecules in the masked region. This result matches well with the different birefringence intensity in POM image, in which the masked region shows a stronger birefringence than the unmasked region (Fig. 3.2c-ii). We should note that, although the patterned gels showed strong birefringence, PBDT only possesses weak orientation, as revealed by the small linear dichroic ratio (Fig. 3.10). For simplicity and better understanding the proposed mechanism, however, we drawn the PBDT in perfect alignments in the schematic figures.

The swelling mismatching depends on many factors, such as the dimension of mask, the polymerization kinetics, the formulation of the precursor solution of gel, etc. In the present system, the swelling mismatching boundary was not sharply coincident with the mask boundary but located inside the mask region, 0.7 mm from the boundary. Therefore, when the width of the masked region was decreased below a value of 1.5 mm, strong swelling mismatching could not be formed, and we observed a decrease in the birefringence of unmasked regions.

Two reasons are considered for why the boundary between high swelling region and low swelling region did not coincide with the boundary of the photo mask. One is the non-parallel UV light irradiation, as shown in Supplementary Fig. 3.6a. The other is the mass transportation of reactive species (small molecules of monomer, crosslinker, and initiator) and water from the masked region towards the unmasked region during the reaction, as the latter region has a fast polymerization during the gelation. As the polymerization took hours, the maximal diffusion distance d of reactive species is in the order of 1 mm, using the diffusion relation $d = (D•t)^{0.5}$ and diffusion constant $D = 10^{-5}$ $cm^2•s^{-1}$ for small molecules[32]. This justifies that the diffusion effect of reactive species could not be neglected. On the other hand, the PBDT diffusion is negligible due to its large molecular weight. Thus, a composition gradient was formed, where the unmasked regions have a higher concentration of matrix polymer and the high ratio of the matrix polymer/PBDT than those of the masked regions. The former was evidenced by the large thickness in the unmasked region of the as-prepared samples (Fig. 3.6b-i and Fig. 3.6c), and the latter was confirmed by the results shown in Figure 3.7. As the polymerization in the masked region was retarded, it has a larger swelling ratio than the unmasked region, as shown in Supplementary Fig. 3.6c. Based on the experimental results, however, this deviation of pattern feature does not affect the conclusion of this work.

3.3.3 Universality for creating complex superstructures

Following the above concept, hydrogels with more complex superstructures could be developed by designing different masks to control the swelling mismatching (Fig. 3.3). We used three basic shapes, stripe, dot, and branch as masked regions (black), to build five mask patterns with different features. Besides the periodical straight stripes (mask I) as already shown in Fig. 3.1b, concentric circle stripes (mask II), periodical cubic dots (mask III), hexagonal dots (mask IV), and periodical honey-comb networks (mask V) were designed (Fig. 3.3, top). These mask patterns can be classified into three types: (A) line symmetric (I), (B) circular symmetric (II), and (C) periodical (III, IV, V).

The as-prepared gels with these masks also showed grooves or wells in the masked regions (Fig. 3.3a). After the gels were swelled in water, the masked regions showed higher swelling than the unmasked regions. The swelling mismatch led to programmed strong internal stress and PBDT alignments, which were confirmed by observation under circular polarizing light (Fig. 3.3b). The alignments of PBDTs identified by POM images with tint plate (Fig. 3.3d) for swollen gels are illustrated in Fig. 3.3c and 3.3e.

Type (A) has been discussed in the previous text; here we consider type (B). The mask of circular stripes produces circular orientation of PBDT in the unmasked region that experiences a tension due to less swelling, and radial orientation in the masked region that experience a compression due to more swelling (Fig. 3.3, Column II), similar to the effect of the straight stripes mask (Fig. 3.3, Column I). The gel also showed a global saddle-like deformation, indicating that the outer region of the gel swells more than that of the inner region, and a net internal stress leads to the deformation of the gel[28]. Then, we consider type (C). The dot mask (cubic dots and hexagonal dots) produces dot-like high swelling regions (Fig. 3.3, Column III, IV). In these cases, the unmasked regions between two nearest dots experience compression in the direction of line that connects the two dots. As a result, the PBDT molecules in this region oriented perpendicular to the line that connects the two dots. Since the net stress in the center of the cubic or hexagonal patterns is cancelled, PBDT has no preferential orientation in the central region. The honey-comb mask produces network-like high swelling regions (Fig. 3.3, Column V). Since these network arms are under compression, PBDT molecules oriented in perpendicular to the network arms. PBDT has no preferential orientation in the central region of the network, indicating that there is no net stress in this region. Thus, all the gels of type (C) share the common feature that the internal stress is cancelled in the center of unmasked region to give amorphous structure in this region. These gels, having no net stress globally, were flat after swelling. These results demonstrate that by designing proper masks, very complicated liquid crystal domains are possible to be obtained.

3.3.4 Toughening the superstructure hydrogels

As common polyelectrolyte hydrogels, these superstructure hydrogels were mechanically weak. Taking advantage of their polyelectrolyte nature, we further toughen these gels by introducing a second neutral network, based on the double network concept[1,29]. The superstructures were preserved even after inducing the second network of polyacrylamide (PAAm) (Fig. 3.4a). The obtained double network gel was much tougher than its single network, sustaining large tensile deformation.

Accompanying with the deformation, the superstructure deformed reversibly without rupture (Fig. 3.4a and 3.4b). The tensile stress-strain curves are anisotropic, showing higher fracture stress and strain along the strip direction than those of the vertical direction (Fig. 3.4c). These anisotropic mechanical properties should be attributed to the patterned gel structure itself, not to the PBDT superstructure.

The superstructure change under the stretching parallel to the stripe direction is shown in Fig. 3.4a. Before stretching, the birefringence of PBDT was stronger than that of PDMAPAA-Q gel. The masked and unmasked regions showed orange and blue birefringence color under crossed polarizers with 530 nm tint plate, respectively. At this time, in the masked regions, orientation of PBDT was vertical to the tensile direction, and in the unmasked regions, orientation of PBDT was parallel to the tensile direction. When stretching started, PDMAPAA-Q gel and PBDT gradually oriented along with the tensile direction. After extension to a certain strain, ε, birefringence of PDMAPAA-Q gel became stronger than PBDT and showed opposite birefringence color against PBDT. In the unmasked regions, orange color birefringence was shown by PDMAPAA-Q. In the masked region, PBDT molecules rotated toward the stretching direction. After that, birefringence gradually disappeared due to increasing birefringence of the PDMAPAA-Q gel (elongation strain $\varepsilon = 0.5$). The change of birefringence with tensile strain is completely reversible. After stretching, the initial birefringence pattern still remained.

The superstructure change under the stretching perpendicular to the stripe direction is shown in Fig. 3.4a and. Before stretching, in the masked regions, orientation of PBDT was parallel to the tensile direction and in the unmasked regions, orientation of PBDT was vertical to the tensile direction. When stretching started, PDMAPAA-Q gel and PBDT gradually oriented along with the tensile direction. After some extension, in the masked regions, PBDT molecules rotated toward the stretching direction and showed orange birefringence color of oriented PDMAPAA-Q. In the unmasked regions, due to the strong orientation of PBDT, this region still showed blue color birefringence by oriented PBDT ($\varepsilon = 0.3$). After stretching, the initial birefringence pattern still remained.

3.4 Conclusions

In conclusion, we have developed *long-range* superstructure hydrogel composites with alignments of semi-rigid polyelectrolyte molecules by tuning the internal stress field. By photolithographic patterning, we can program the swelling mismatch of the gels, which induces large internal stress. This internal stress directs orientation of semi-rigid polymers, which are frozen by the strong polyion complexation between the two oppositely charged polyelectrolytes. By using the double network concept, these superstructure gels can be developed into tough double network gels. At the moment, we could only prepare the superstructure gels containing low concentration of PBDT (several wt%) due to its high viscosity limitation. Accordingly, we did not observe distinct mechanical property or swelling property originated from this superstructure. In forthcoming paper, we will apply this idea to rigid biomolecules with relatively low molecular weight at high concentration for creation of specific functions. For example, by controlling the orientation of rigid collagen molecules in tough double network hydrogels, we are able to develop hydrogels with anisotropic mechanical properties like cartilages.

Structural biomacromolecules, such as F-actin, microtubule, and collagen, are all negatively charged rigid molecules. During tissue growth, different growth rate will build internal stress which may also play a role in directing the orientation of these structural biomacromolecules. This work should give insight in understanding the structure formations of these biomacromolecules in living cells and soft tissues.

3.5 References

1. Gong, J. P., *Soft Matter* **6,** 2583-2590 (2010).
2. J. Y. Sun, Z. Zhao, W. R. K. Illeperuma, O. Chaudhuri, K. H. Oh, D. J. Mooney, J. J. Vlassak & Z. Suo, *Nature* **489,** 133-136 (2012).

3. T. L. Sun, T. Kurokawa, S. Kuroda, A. B. Ihsan, T. Akasaki, K. Sato, Md. A. Haque, T. Nakajima & J. P. Gong, *Nat. Mater.* **12,** 932-937 (2013).

4. E. Palleau, D. Morales, M. D. Dickey & O. D. Velev, *Nat. Commun.* **4,** 2257 (2013).

5. P. Calvert, *Adv. Mater.* **20,** 1-14 (2008).

6. A. R. Liberski, J. T. Delaney, H. Schäfer, J. Perelaer & U. S. Schubert, *Macromol. Biosi.* **11,** 1491-1498 (2011).

7. A. S. Hoffman, *Adv. Drug Deliver. Rev.* **64,** 18-23 (2012).

8. B. V. Slaughter, S. S. Khurshid, O. Z. Fisher, A. Khademhosseini & N. A. Peppas, *Adv. Mater.* **21,** 3307-3329 (2009).

9. Y. Qiu and K. Park, *Adv. Drug Deliver. Rev.* **64,** 49-60 (2012).

10. A. K. Jeffery, G. W. Blunn, C. W. Archer & G. Bentley, *J. Bone Joint Surg. Br.* **73-B,** 795-801 (1991).

11. Y. Wang, T. Azais, M. Robin, A. Vallee, C. Catania, P. Legriel, G. Pehau-arnaudet, F. Babonneau, M. Giraud-Guille & N. Nassif, *Nat. Mater.* **11,** 724-733 (2012).

12. A. P. Newman, *Am. J. Sports Med.* **26,** 309-324 (1998).

13. Q. Z. Chen, C. T. Wong, W. W. Lum K. M. Cheung, J. C. Leong & K. D. Luk, *Biomaterials* **25,** 4243-4254 (2004).

14. P. Kiviranta, J. Rieppo, R. K. Korhonen, P. Julkunen, J. Toyras, J. S. Jurvelin & *J. Orthop. Res.* **24,** 690-699 (2006).

15. R. Aspden, *Proc. R. Soc. B* **258,** 195-200 (1994).

16. E. Loizou, L. Porcar, P. Schexnailder, G. Schmidt & P. Butler, *Macromolecules* **43,** 1041-1049 (2010).

17. M. T. Mc-Clendon & S. I. Stupp, *Biomaterials* **33,** 5713-5722 (2012).

18. E. Paineau, I. Dozov, I. Bihannic, C. Baravian, M.-E. M. Krap, A.-M. Philippe, S. Rouziere, L. J. Michot & P. Davidson, *ACS Appl. Mater. Interfaces* **4,** 4296-4301 (2012).

19. L. Maggini, M. Liu, Y. Ishida & D. Bonifazi, *Adv. Mater.* **25,** 2462-2467 (2013).

20. M. A. Firestone, D. M. Tiede & S. Seifert, *J. Phys. Chem. B* **104,** 2433-2438 (2000).

21. S. Zhang, M. A. Greenfield, A. Mata, L. C. Palmer, R. bitton, J. R. Mantei, C. Aparicio, M. Olvera de la Cruz & S. I. Stupp, *Nat. Mater.* **9,** 594-601 (2010).

22. J. Kim, J. A. Hanna, M. Byun, C. D. Santangelo & R. C. Hayward, *Science* **335,** 1201-1205 (2012).

23. Z. L. Wu, M. Moshe, J. Freener, H. Therien-Aubin, Z. Nie, E. Sharon & E. Kumacheva, *Nat. Commun.* **4,** 1586 (2013).

24. M. F. Islam, M. Nobili, F. Ye, T. C. Lubensky & A. G. Yodn, *Phys. Rev. Lett.* 95, 148301 (2005).

25. Md. Arifuzzzaman, Z. L. Wu, T. Kurokawa, A. Kakugo & J. P. Gong, *Soft Matter* **8,** 8060-8066 (2012).

26. Md. Arifuzzaman, Z. L. Wu, R. Takahashi, T. Kurokawa, T. Nakajima, & J. P. Gong, *Macromolecules* 46, 9083-9090 (2013).

27. Z. L. Wu, T. Kurokawa, S. M. Liang, H. Furukawa & J. P. Gong, *J. Am. Chem. Soc.* **132,** 10064-10069 (2010).

28. Y. Klein, E. Efrati & E. Sharon, *Science* **315,** 1116-1120 (2007).

29. J. P. Gong, Y. Katsuyama, T. Kurokawa & Y. Osada, *Adv. Mater.* **15,** 1155-1158 (2003).

30. M. W. Frohlich, *Biotech. Histochem.* **61,** 139-143 (1986).

31. P. Whittaker, R. A. Kloner, D. R. Boughner, & J. G. Pickering, *Basic Res. Cardiol.* **89,** 397-410 (1994).

32. D. Eisenberg & D. Crothers, *Physical Chemistry with Applications to the Life Sciences* 603-606 (The Benjamin, San Francisco, 1979).

33. K. Wagner, D. Harries, S. May, V. Kahl, J. O. Rädler & A. Ben-Shaul, *Langmuir* **16,** 303-306 (2000).

34. J. Gummel, F. Cousin & F. Boué, *J. Am. Chem. Soc.* **129,** 5806-5807 (2007).

35. M. Hesse, H. Meier & B. Zeeh, *Spectroscopic Methods in Organic Chemistry* 4-19 (Thieme, Stuttgart, 2007).

3.6 Schemes

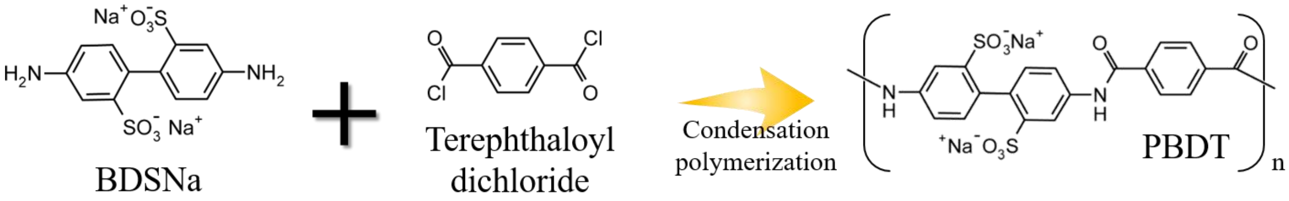

Scheme 3.1 | Synthesis of PBDT by an interfacial poly-condensation reaction.

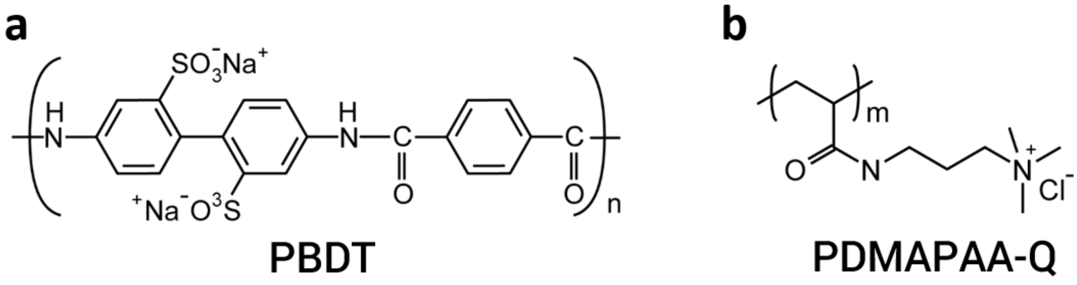

Scheme 3.2 | Chemical structure of components. (**a**) The rigid anionic polyelectrolyte, PBDT, which is embedded in hydrogel matrix. (**b**) The flexible cationic polyelectrolyte, PDMAPAA-Q, which forms a hydrogel network by chemically crosslinking.

3.7 Figures

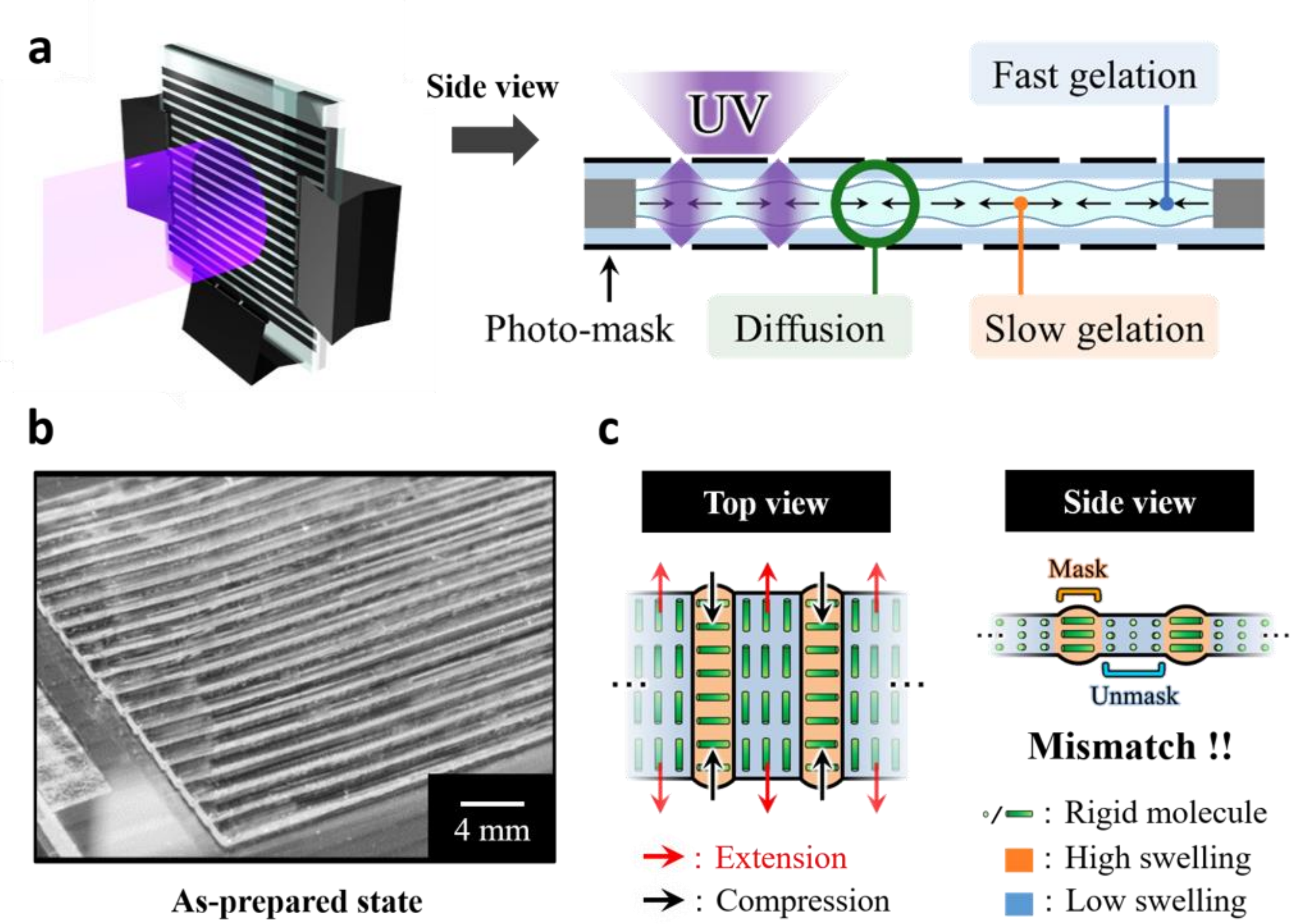

Figure 3.1 | Photolithographic patterned hydrogels with controllable swelling mismatch and the resultant of internal-stress-directed orientation of rigid macromolecules. (**a**) Experimental set-up for synthesis of programmed superstructure in the hydrogels using photolithographic method. As an example, two identical photo masks of stripe pattern are placed in phase on two surfaces of the reaction cell containing precursor solution of gel. The width of masked regions (black) and unmasked regions (white) are 2 mm and 0.6 mm, respectively. UV was irradiated from both sides of the cell to initiate polymerization. (**b**) After gelation, the as-prepared gel shows morphology characteristic to the mask pattern. (**c**) Schematic to show the built-up of internal stress, due to the swelling mismatch, and the resultant superstructure of rigid molecules in the photolithographic patterned gels. In the gel, composition gradient between the masked and unmasked regions leads to swelling mismatch. For stripe-patterned hydrogel, as shown in (**b**), the large swelling region experiences a compression from the less swelling region. Rigid molecules embedded in the gel intend to orient along the tensile direction while they orient in perpendicular to the compressive direction. Thus, the patterned swelling mismatch induces programmed internal stress, which directs the orientation of the rigid macromolecules. Using oppositely charged rigid molecules and polymer network, the structure is memorized by polyion complex formation after dialysis of their counter-ions.

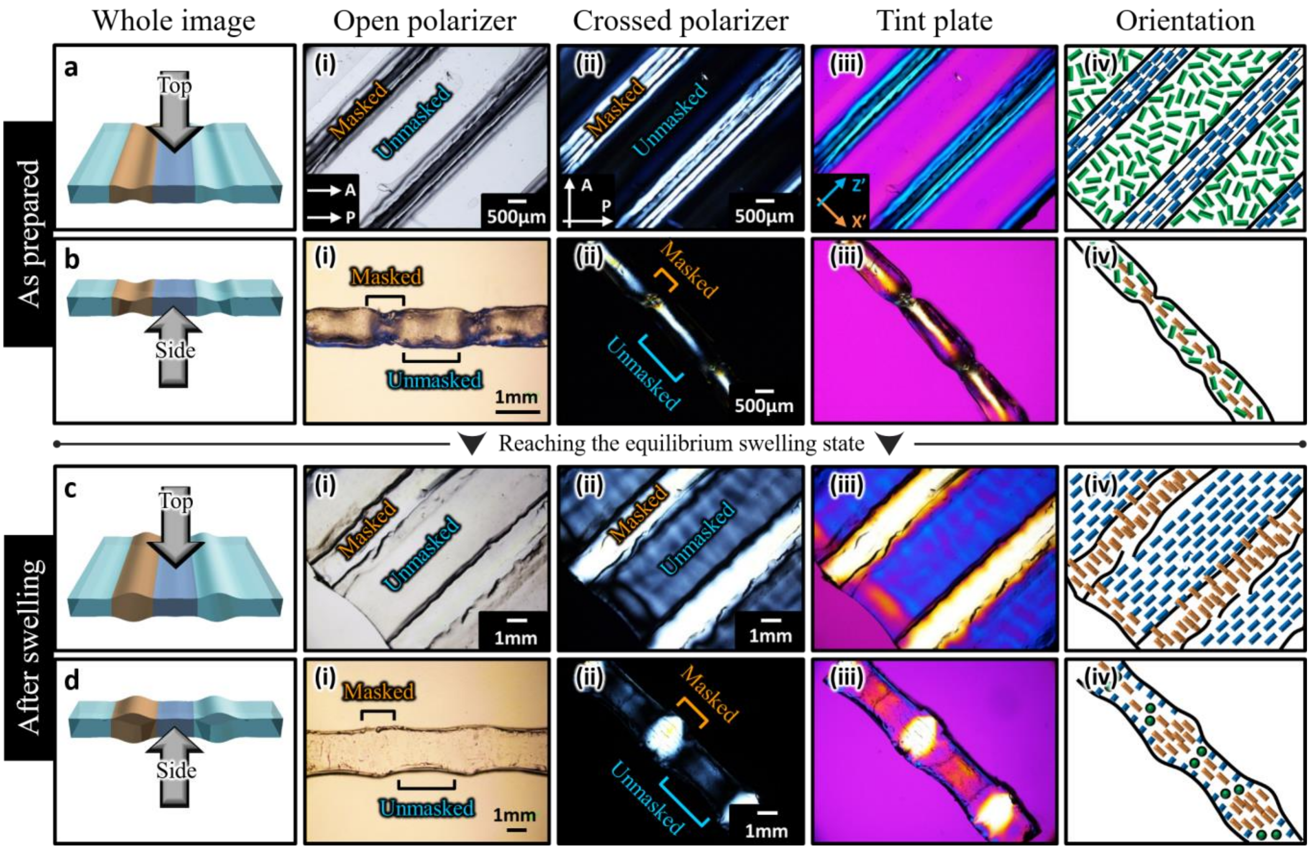

Figure 3.2 | Characterization of superstructure formed in patterned hydrogels. Observation of superstructure of PBDT in patterned PDMAPAA-Q hydrogels at as-prepared (**a**, **b**) and swollen (**c**, **d**) states. The gels were observed under polarizing optical microscope (POM) from top (**a**, **c**) and side (**b**, **d**) direction. The thickness of the observation direction from side was unified into about 2 mm. The images in column (i) were observed under the parallel polarizers, columns (ii) and (iii) were observed under the crossed polarizers without and with 530 nm tint plate, respectively. The column (iv) is a schematic illustration of the orientation of PBDT molecules within the gel, where the green bars represent PBDTs with weak orientation, the green circles represent PBDTs orientation of vertical direction to the sheet, the orange and blue bars represent highly ordered PBDTs. A: Analyzer; P: Polarizer; X′: Fast axis of the tint plate; Z′: Slow axis of the tint plate.

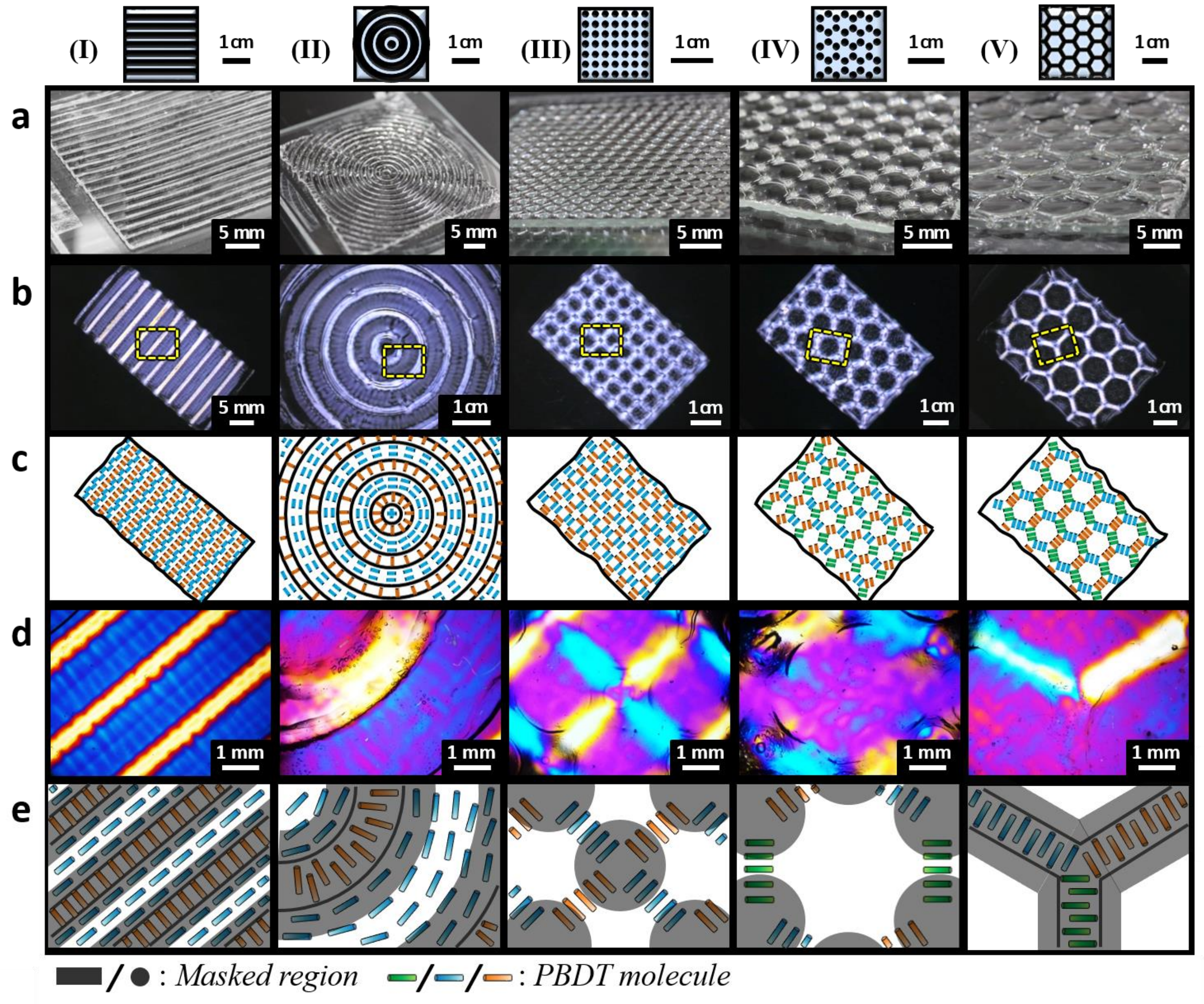

Figure 3.3 | Controlling of superstructure in hydrogels by using different masks. (**a**) Images of the as-prepared gels taken by digital camera to show the gel appearances and patterns. The masks used for photolithography are shown in the top of each column, where the masked regions are black and unmasked regions are white. (**b**) Images of swollen gels observed under circular polarized light. The oriented domains show strong birefringence. (**d**) The yellow rectangle regions shown in row (**b**) were observed by crossed polarizers with 530 nm tint plate to determine the molecular orientation. (**c**) and (**e**) Schematic illustrations of the orientation of PBDT molecules within the swollen gel, where the orange, blue and green bars represent highly ordered orientation. The grey regions in **(e)** correspond to the regions of masks, where the central parts of gels have high swelling. Size of mask patterns: (I) Width of masked stripes and distance between stripes are 1.5 mm and 0.5 mm, respectively. (II) Width of masked stripes and distance between stripes are 2.0 mm and 0.6 mm, respectively. (III, IV) Diameter of dots and distance between dots are 2.0mm and 0.6mm, respectively. (V) Width and length of branch line are 1.5mm and 4.0mm, respectively.

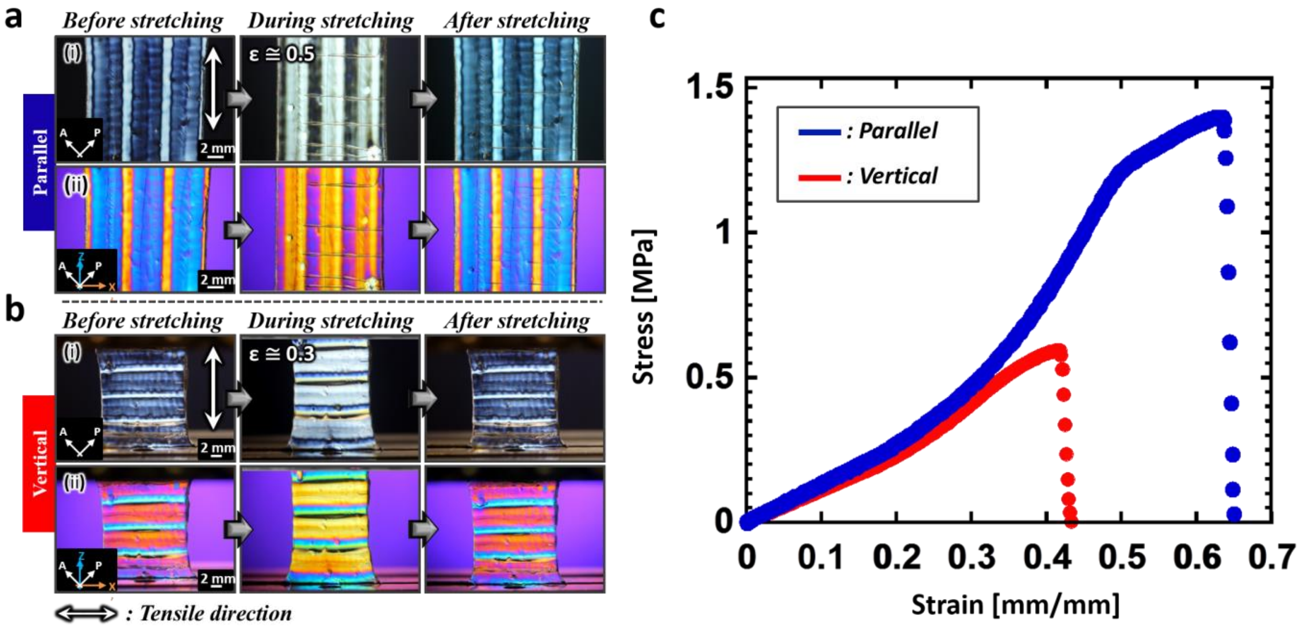

Figure 3.4 | Tough double network (DN) hydrogels with superstructures. (**a, b**) Birefringence patterns showing the reversible change in the stripe superstructures of DN gel during stretching in the direction parallel (**a**) and vertical (**b**) to the strip direction. Images in rows (a-i) and (b-i) were observed under the crossed polarizers. Images in rows (a-ii) and (b-ii) were observed under the crossed polarizers with 530 nm tint plate. Double-headed arrow shows the tensile direction. Tensile strain, ε, is defined as $(L\text{-}L_0)/L_0$, in which L_0 and L are the length of the gel before and during elongation, respectively. (**c**) Stress-strain curves of DN gels stretched in the directions parallel (blue) and vertical (red) to the stripe direction.

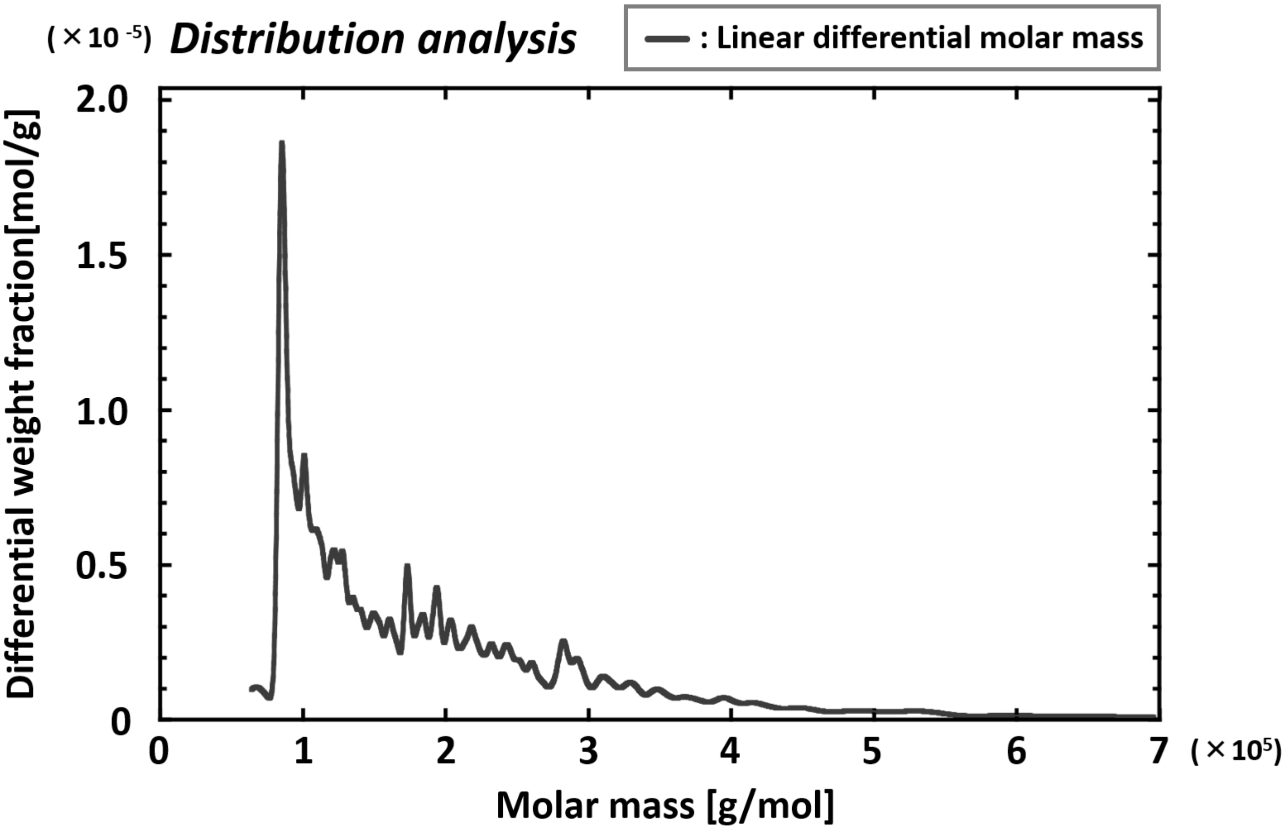

Figure 3.5 | Molecular weight measurement of PBDT by SEC-MALS. Distribution analysis shows that PBDT used in the present study has an average molecular weight, M_w of about 200,000 g•mol^{-1}, number average molecular weight, M_n of about 150,000 g•mol^{-1}, and polydispersity, M_w/M_n of about 1.4.

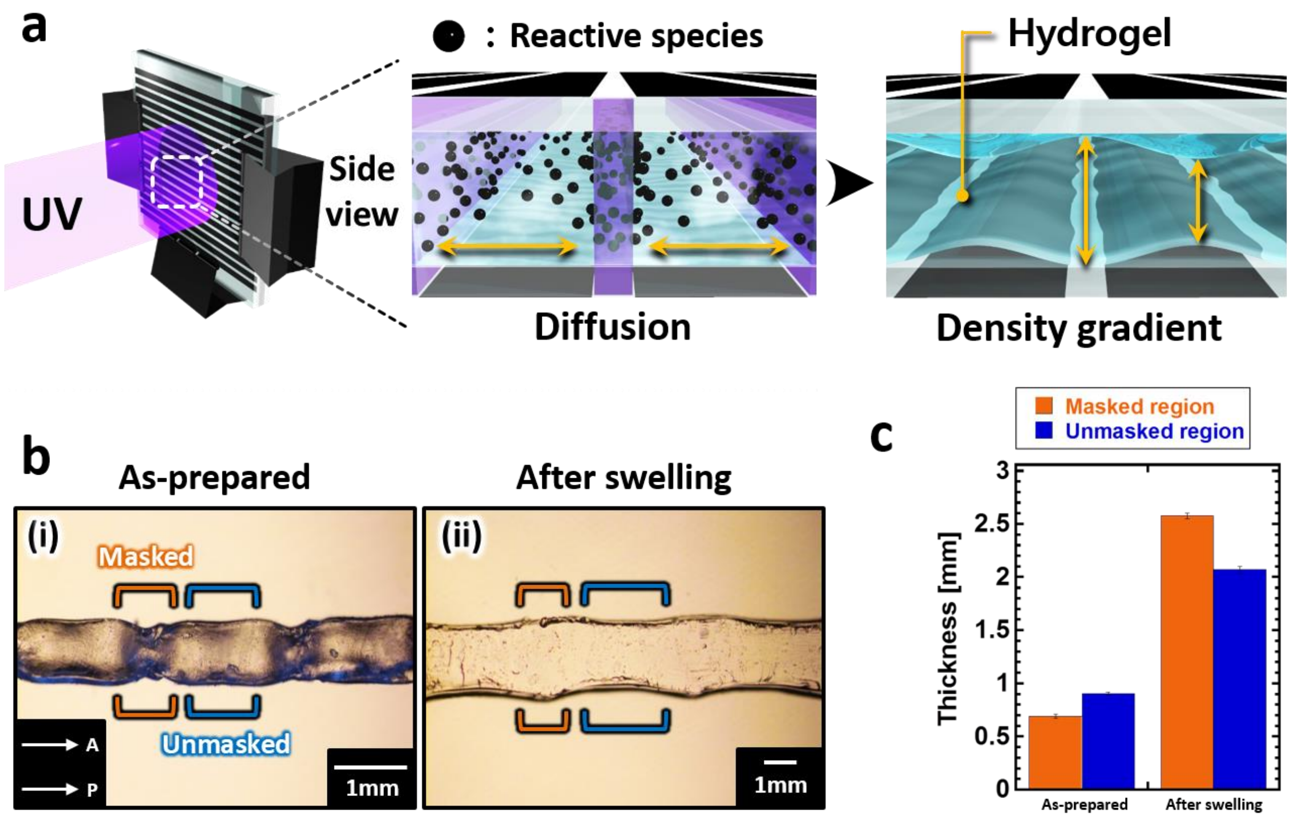

Figure 3.6 | Illustration of the deviation of the width of masked and unmasked regions in the as-prepared patterned gel from the feature of photo mask. (**a**) Schematic to show the feature deviation between the patterned gels and the photo mask. There are two reasons for this deviation. 1) Because the UV light irradiated for polymerization is not completely parallel, the width of area irradiated is wider than that of transparent stripe in the mask. On the other hand, the width of area without direct irradiation is narrower than that of black stripe in the mask. 2) The regions with direct and indirect irradiation have quite different reaction kinetics. Due to the difference of reaction kinetics, diffusion of reactive species (monomer, crosslinker and initiator) from the masked region having a slow reaction to unmasked region having a fast reaction was induced. Therefore, composite gradient and internal stress during the gelation and swelling processes was built. Since the reaction time was long (about 7 h), the latter effect should play an important role in the formation of the gradient structure. (**b**) The images of patterned gels observed from side direction. The images (i) and (ii) are patterned gel in the as-prepared state and swollen state, respectively. (**c**) Thickness of the masked and unmasked regions of patterned gel in the as-prepared and swollen states.

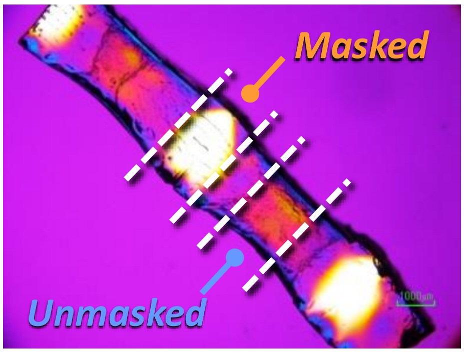

Sample^{a}	C %	H %	N %	S %	W_Q/W_P^{b}
Masked	47.10	9.40	12.06	0.46	23.4
Unmasked	47.35	9.43	12.26	0.17	65.1

Figure 3.7 | Elemental analysis results of the masked and unmasked regions of patterned gel. (**a**) The sample with stripe-patterned gel was used for elemental analysis. After swelling the as-prepared gel in a large amount of water to remove the residual reagents, the patterned gel was cut into small piece in masked and unmasked regions, as shown in the following scheme. After vacuum-drying, elemental analysis was conducted at the chemical analytical center of Hokkaido University, Japan, using the standard techniques. (**b**) Mass ratio of PDMAPAA-Q to PBDT, W_Q/W_P, is estimated from the values of N and S. The mass ratio in feed was 41.2. The table shows that the mass ratio of PDMAPAA-Q to PBDT, W_Q/W_P, is much lower than the value in feed (41.2) in the masked region while much higher than the value in feed in the unmasked region. The result confirms that the reactive species diffuse from the masked region to unmasked region during the polymerization.

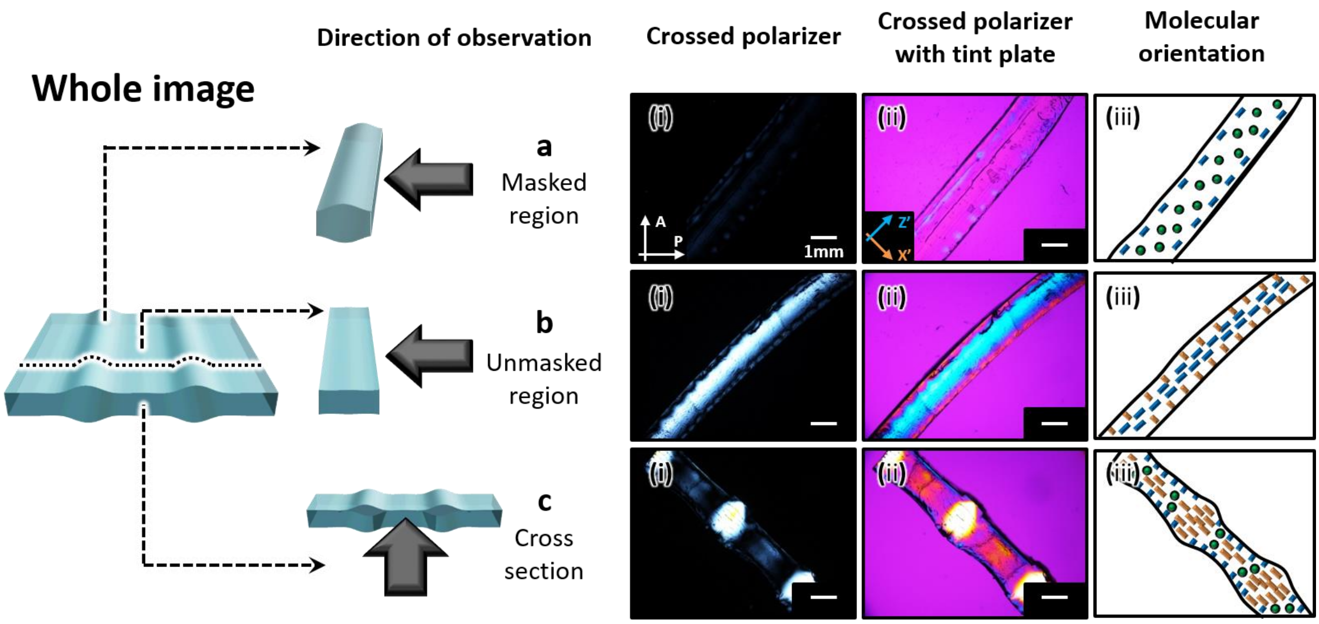

Figure 3.8 | Observation of swollen PBDT-containing PDMAPAA-Q hydrogel from cross-section direction. Two pieces of gels were cut from masked (**a**) and unmasked (**b**) regions, respectively, along the patterned stripe direction and observed from the cross-section direction. One piece of gel was also cut vertical to the patterned stripes and then observed from the cross section direction (**c**). The images in columns (i) and (ii) were observed under the crossed polarizers without and with insertion of 530 nm tint plate, respectively. The column (iii) is a schematic illustration of the orientation of PBDT molecules in the gel, where the green circles represent PBDT oriented vertical to the sheet, the orange and blue bars represent highly ordered PBDTs.

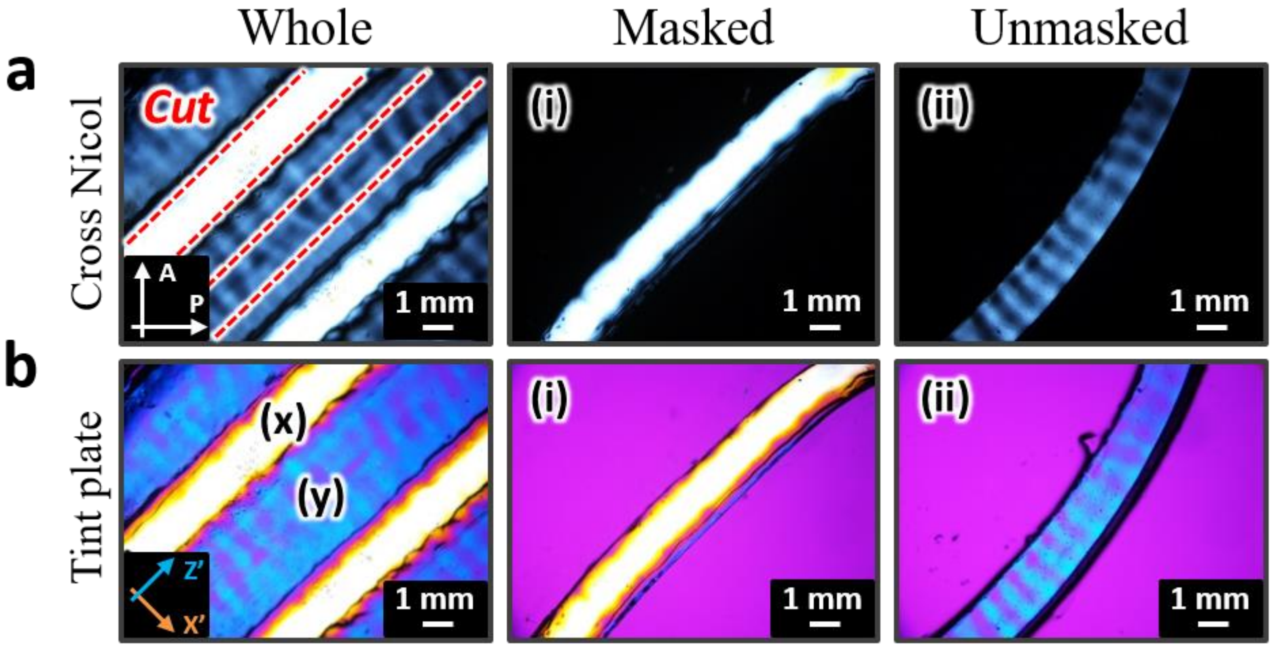

Figure 3.9 | Observation of swollen PBDT-containing PDMAPAA-Q hydrogel from top direction after slicing the masked and unmasked regions into separate stripes. Two pieces of gels were cut from masked (i) and unmasked (ii) regions, respectively, along the patterned stripe direction and observed from the cross-section direction. The images in columns (**a**) and (**b**) were observed under the crossed polarizers without and with insertion of 530 nm tint plate, respectively. The results indicate that the oriented structure is fixed even after removal of the internal stress.

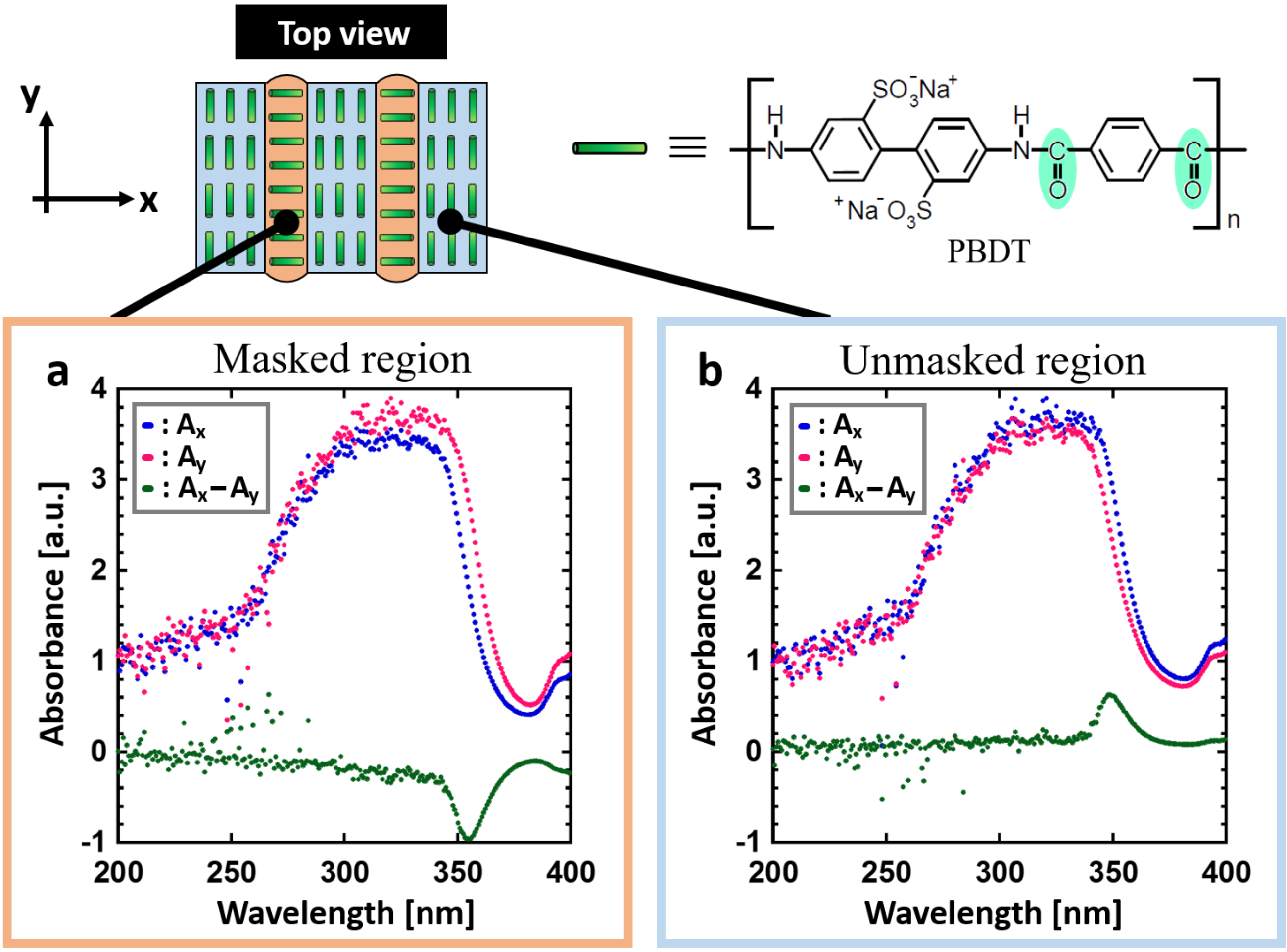

Figure 3.10 | Linear dichroism measurements in the masked and unmasked regions of swollen PBDT-containing PDMAPAA-Q hydrogel with stripe-pattern. Absorbance of polarized UV light in the masked (a) and unmasked (b) regions. A_x and A_y are the absorbance of polarized UV light along with x-axis and y-axis, respectively. The x-axis and y-axis in a sample were defined as shown in the above schematic. The difference of A_x-A_y showed a peak around 350nm. Dichroic ratio, R = $\frac{Ax-Ay}{Ax+Ay}$, in the masked and unmasked regions was -0.21 and 0.11, respectively, as calculated by using the spectrum peak of A_x-A_y. The opposite sign of A_x-A_y values in the masked and unmasked regions indicates the vertical orientation of PBDT in these two regions. These results are quantitatively in agreement with the POM observation results.

CHAPTER 4

Visualizing Internal Stress in Hydrogel Matrix Based on Orientation of Semi-Rigid Polymer

4.1 Introduction

Intriguing surface patterns and bulk deformations are often observed in dynamic, non-equilibrium processes of soft substances[1-5]. For example, intricate morphological patterns found in the human body, such as creases of the brain, wrinkles on the skin, branches in the lungs and the morphology of the gut, are formed during tissue growth[6-9]. Surface creasing of hydrogels induced by fast heterogeneous swelling is also a well-known phenomenon[10, 11]. These phenomena are considered to be formed via the mechanical instability induced during tissue growth and hydrogel swelling[12, 13]. Many researches, both theoretical and experimental, have been devoted to reveal the surface crease formation mechanism using hydrogels as a model substance[14-17]. The mechanical instability phenomenon has also been exploited to generate functional properties such as tunable wettability or adhesiveness, switchability of photonic properties, and cellular interaction ability[18-21]. Precise understanding of the mechanical instability of gels cannot only provide understanding on the morphology formation of biological tissues but also give direction to design and fabricate novel, functional soft materials.

Most studies on the hydrogel swelling instability have been focused on a constraint boundary condition[14-17, 22-24]. That is, the gel layer is fixed to the rigid substrates that are flat or cylindrical. When a gel layer is constraint to a flat substrate, “polygonal” surface crease pattern is formed. The crease formation is explained by the swelling mismatch between the outer and inner layers of the gel. When the gel is immersed in water, the swelling starts from the surface layer of the gel, and this layer is able to expand freely. In contrast, the inner layer swelling is restricted to the substrate of the gel. This swelling mismatch induces a mechanical instability and leads to buckling. T. Tanaka, *et al.* firstly revealed this buckling mechanism and developed a theory that well describes the “polygonal” crease pattern under restricted swelling condition[25]. Later, Suo *et al.* extensively studied the conditions for the occurrence of buckling[26].

When a gel is permitted to swell in an unrestricted condition, usually more rich and complicated phenomenon is observed. For example, a piece of sheet-shape hydrogel shows both surface buckling and bulk shape deformation, and the surface crease pattern evolves differently from the “polygonal” pattern observed for the gel restricted to a flat substrate[14-17, 22-25]. This suggests the effect of mechanical coupling between the bulk deformation and the surface buckling. However, understanding of the unrestricted swelling is still quite limited[10, 11].

In this Chapter, we study the mechanical instability occurring during the free swelling of a piece of disc-shape hydrogel. The chapter consists of three parts. In the first part, we show experimentally the evolution of surface crease pattern and bulk deformation during the swelling. A polyelectrolyte hydrogel, which has fast swelling kinetics was adopted to induce mechanical instability. Semi-rigid polyelectrolyte molecules carrying opposite charges were physically entrapped in the hydrogel matrix as stress sensor for analyzing the internal stress induced by the mechanical instability[10, 11, 27]. The semi-rigid macromolecules can sense the internal stress field sensitively by orienting their direction along the internal tensile direction in hydrogels. Such orientation of the semi-rigid polyelectrolyte molecules is “memorized” by forming polyion complex with the oppositely charged network, even after swelling[10,11]. Therefore, we could recall the instability pattern during heterogeneous swelling by analyzing the molecular alignment in the post-swollen sample from birefringence observation. This robust method should give us useful information which was previously unattainable. In the second part, we show that the unique crease pattern is the result of coupling of surface instability with the saddle-like bending of the gel. In the third part, we develop a theoretical mechanism to describe this mechanical coupling, based on the contraction energy initially proposed by T. Tanaka, *et al.*, assuming that the gel is not flat but saddle shaped with a mean curvature approaching zero (minimal surface).

4.2 Experiments

4.2.1 Materials

The cationic monomer, *N*-[3-(*N,N*-dimethylamino)propyl]acrylamide methyl chloride quaternary (DMAPAA-Q) (Kohjin Co. Ltd. Japan) and the photo-initiator, 2-oxoglutaric acid (OA) (Wako Pure Chemical Industries Ltd. Japan) were used as received without further purification. *N,N'*-methylenebis(acrylamide) (MBAA) (Wako Pure Chemical Industries Ltd. Japan) was recrystallized from ethanol and used as a chemical cross-linker. Poly(2,2'-disulfonyl-4,4'-benzidine terephthalamide) (PBDT), a water soluble, anionic, semi-rigid polymer, was synthesized by an interfacial polycondensation reaction[28]. The synthesized PBDT had an average molecular weight, M_w of about 200,000 g/mol, number average molecular weight, M_n of about 150,000 g/mol, and polydispersity, M_w/M_n of about 1.4. These values were investigated by GPC assay. The aqueous solution of PBDT exhibited a critical low liquid crystalline concentration, C_LC^*, of 2.8 wt%[29,30]. For all experiments, water was deionized and purified with 0.22 µm and 5 µm membrane filters *prior to* use.

4.2.2 Synthesis of hydrogels

The positively charged gel was synthesized by radical polymerization of DMAPAA-Q and MBAA in the presence of a small amount of PBDT as stress sensor. In order to synthesize the hydrogel film, the reaction cells were prepared by sandwiching a 1 cm wide silicone spacer (thickness: 1 mm) along the periphery between two parallel glass plates. The aqueous pre-gel solution contained 2.0 M DMAPAA-Q, 1.0 wt% PBDT, 2 mol% MBAA, and 0.15 mol% OA (the amount in mol% is related to DMAPAA-Q). After proper mixing, the pre-gel solution was injected into the reaction cells. UV irradiation from both sides of the reaction cell (UV light intensity is 3.9 mW/cm^2) was performed for 6.0 h in an argon atmosphere at room temperature to form the gel. After that, the as-prepared gel, of 60×60×1.0 mm^3 in dimension, was carefully removed from the glass reaction cell and cut into disc shape (diameter (D):6 mm, thickness (T):1 mm) using a mechanical gel cutter (Dumb Bell Co. Ltd. Japan).

4.2.3 Swelling experiments

The as-prepared disc-shape gel was immersed in a large excess of water. Blue dye, Alcian blue (0.05 wt%), was added in the water to acid the visualization of the surface crease pattern. At different swelling times, the gel was taken out from the solution and photographed with a digital camera and then observed with an optical microscope.

4.2.4 Polarizing optical microscope (POM) observation

The birefringence of the gels in the equilibrium swelling state was observed with a polarizing optical microscope (POM) (Nikon, Eclipse, LV100POL) in parallel and crossed polarization modes at room temperature. Gel samples were placed on glass slides and observed from the top. All of the PBDT-containing PDMAPAA-Q gel samples exhibited a first-order white-gray birefringence color, so that a 530 nm sensitive tint plate was inserted between the polarizer and the analyzer to determine the orientation direction of the rigid PBDT molecules[10,11,31].

4.2.5 Preparation of a thin hydrogel sheet fixed onto the saddle shaped substrate

Two polyurethane rubber sheets (width: 15 mm, length: 150 mm, thickness: 1 mm) were stretched uniaxially along their longitudinal directions (strain: $\varepsilon=0.3$) and then glued together perpendicularly, forming a residually stressed compound. A square-shaped hydrogel (width: 13 mm, length: 13 mm, thickness: 0.5 mm) was glued onto the surface of the stretched rubber compound at the junction point. By releasing the stretching of the compound, a compressive stress was applied on the hydrogel, which induces a saddle shape transition.

Each sample was immersed in a large excess of water. Blue dye, Alcian blue(0.05 wt %), was added in the water to acid the visualization of the surface crease pattern. After reaching equilibrium state (~600 s), the samples were taken out from the solution and photographed with a digital camera and then observed with an optical microscope. The thickness of gel changed from 0.5 mm to 1.15 mm. We should notice that the gel sheets homogeneously adhered to the polyurethane substrate without any delamination even after swelling.

4.3 Results & discussion

4.3.1 Results of visualization of internal stress induced by swelling instability

The as-prepared gel, with a diameter of 6 mm and a thickness of 1 mm, was smooth, flat, and transparent, as shown in Figure 4.1a. When the sample was immersed in water, creasing at surface and annulus regions were immediately observed. Sharp boundaries between bumps of creases were clearly observed as blue lines. In concomitant to these surface and edge instabilities, the flat gel bended into saddle-like shape (Figure 4.1b,c). At the early stage of swelling (~100 s), polygonal-like surface creasing was observed (inset of Fig. 4.1b,c), in similar to the previous reports of the surface crease pattern on gels constraint on flat rigid substrates[14-17, 22-25]. As the swelling time increased (~200 s to ~400 s), the crease on the annulus region disappeared and the polygonal pattern on the central disc region changed to a stripe-like crease pattern (Fig. 4.1d, e,f). The stripe creases on the two surfaces of the gel orthogonally aligned, so the blue boundary lines looked like “lattices” when being observed through the thickness of the gel (Fig. 4.1d, e). It should be pointed out that this “lattice” like pattern was interpreted incorrectly as lattice crease pattern in the previous works[10,11]. At a swelling time of around ~500 s, the surface crease patterns disappeared, and the gel surface became smooth, while the saddle-like shape still remained, with a decreased curvature (Fig. 4.1g). After ~600 s swelling, the gel became completely smooth and flat without any deformation, as like the shape of the as-prepared sample but with an isotropic increase in volume (8 times of the initial volume) (Fig. 4.1h). The stripe-like crease pattern observed in this study is unique and should be attributed to the free swelling of the gel, whereupon the saddle-like bending of the gel also occurred. The vertically crossed stripes on the two surfaces of the sample is the result of coupling of the surface crease pattern and the bulk saddle-like bending that has two bending axes crossing at right angles.

We further performed polarized optical microscopy (POM) observation on the post-swollen samples to analyze the internal stress built during swelling through the alignment of the semi-rigid molecules PBDT entrapped in the gel (Fig. 4.2a). Specifically, the creasing instability induces the internal stress perpendicular to the crease border lines (Fig. 4.2a-i) and the PBDT molecules align along the tensile direction of the internal stress (Fig. 4.2a-ii). The orientation of PBDT is fixed by polyion complex formation between the positively charged gel network and the negatively charged PBDT molecules as a result of dialysis of small ions from the gel during swelling in water[10,11,27]. In order to investigate the correlation between the surface crease pattern and the internal stress, a piece of gel, of 7.0 mm (L)×4.0 mm (W)×2.0 mm (T) in geometry, was cut out from the central region of the disc-shaped sample, with the long axis of the gel piece parallel to one of the bending axes (Fig. 4.2b-x-i). The gel piece was observed through the thickness under POM with inserting the 530 nm sensitive tint plate. Lattice-like birefringence pattern was observed (Fig. 4.2b-x-ii) that can be related to the orientation of PBDT molecules that have positive optical property (Fig. 4.2b-x-iii). Here, the blue bars and orange bars in Figure 4.2b-x-iii indicate the orientation of the PBDT in the two perpendicular directions and black lines indicate the crease border lines on the two surfaces of the sample. Given the high transparency of the gel, this lattice-like birefringence pattern is attributed to the overlapping of the two individual birefringence patterns on the two surfaces of the gel, as the surface stripe crease patterns are aligned in perpendicular with each other on the two surfaces of the gel. This is confirmed by the POM images of two half pieces of the sample sliced through the middle of the thickness (Fig. 4.2b-y-i,z-i)]. Both POM images of the two sliced pieces show the stripe-like birefringence patterns that are in perpendicular to each other (Fig. 4.2b-y-ii,z-ii). The PBDT molecules across the crease border lines are aligned perpendicular to the border lines; while PBDT molecules in between the crease border lines are aligned parallel to the border lines (Figure 4.2b-y-iii,z-iii). The latter indicates that the bending of the bulk gel exerts a tension on the ridge surface and a compression on the basin surface of the bending[32]. Since the stripe-like creases on the two surfaces of the gel are in perpendicular, the PBDT molecules on the two surfaces are also aligned perpendicularly, both for those across and in between the crease border lines. As a result, the whole sample exhibits the “lattice” like birefringence pattern due to the cancellation of birefringence between the border lines, as shown in Figure 4.2b-x-ii, x-iii) [33].

4.3.2 Effect of coupling of two instabilities

Two mechanical instabilities occur during the fast free swelling of the polyelectrolyte gel. One is the saddle-like bending induced by the swelling mismatch between the annulus and inner region of the disc shape gel (Fig. 4.3a), because the annulus region swells faster by taking water from the top, bottom and sides (Fig. 4.3a-i), while the inner disc region swells slower only by taking water from the top and bottom surfaces (Fig. 4.3a-ii). When the inner radius of the annulus is larger than the radius of the disc, the annulus region is compressed, thus the saddle-like bending occurs to minimize the radius mismatch. Such a kind of saddle-like bending was also reported by Y. Klein, *et al.*[34]. Especially, the investigation reported by M. Pezzulla, *et al.*, which is using a disc-shaped elastomer made from a swellable annulus and an unswellable disc, are closely related to our system[35]. The other is surface buckling due to swelling mismatch between the surface layer and inner layer. The surface instability induced by this type of swelling mismatch, as clarified by previous works, generally forms polygonal surface creasing (Fig. 4.3b). The unique stripe-like creasing of crossed orientation on the two surfaces observed in this work is the result of coupling of the surface instability with the saddle-like bending. When the bulk gel deforms into saddle-like shape, the ridge of the bending releases and the basin of bending receives additional stresses (Fig. 4.3c-i), as shown by the orientation of PBDT molecules shown in Figure 4.2. In the center of saddle, on the same point, one direction is in compression and the other direction is in extension. As a result, each surface of the sample receives anisotropic stress by the saddle-like bending, which changes the isotropic polygonal surface creasing into anisotropic, stripe-like pattern (Fig. 4.3c-ii,iii).

We notice that although the bulk bending can induce anisotropy of surface crease, it is not necessary to give continuous stripe-like patterns. The coupling of surface instability and bulk deformation was also studied by observing the surface crease patterns of hydrogel sheets fixed, *prior to* swelling, onto a flat substrate and a saddle-shaped substrate, respectively (Fig. 4.4a). Isotropic polygonal surface crease was observed for the hydrogel fixed on the flat substrate, the same as reported before (Fig. 4.4b-

-i)[15]. In contrary, anisotropic, straight-grained surface crease was found on the hydrogel fixed on the saddle substrate (Fig. 4.4b-ii). The results confirm that the saddle-shaped bending induces anisotropic surface creases, but not necessarily continuous stripes. Next part, we introduce a theory to explain the formation of anisotropic stripe creasing pattern on hydrogel surface.

4.3.3 Theoretical mechanism

Herein, let us consider the mechanism of creasing on the saddle-like hydrogel surface, based on the T. Tanaka's theory. In the beginning, we assume that the priority order of the energy due to compression is lowest with respect to suppression of an energy growth. Under this assumption, it is predicted that a thin gel in the form of a disc morphs into a saddle type minimal surface, because the stretching and bending energy are suppressed on a priority basis[35]. After that, the energy due to compression will be minimized to an acceptable level. Therefore, in the following, we develop a theory by focusing on the energy due to compression of the mechanical potential energy suggested by Tanaka, and consider the influence of the compression with large deformation during swelling. Tanaka's theory is not intended to describe the dynamics in the swelling gel. However, it would be allowed to apply this theory for the crease pattern formation in the process of swelling, because the time scale of crease pattern formation is faster than that of the large deformation. That is, we refer the process of crease pattern formation in our system as a quasi-static transition. Furthermore, in order to fit it to our problem, we consider the energy due to compression from the geometry point of view. In ref. [25], the authors considered the restriction face as an *x*-*y* plane, and the energy due to compression, $U_{\text{(compression)}}$, was described as follows:

$$U_{\text{(compression)}} = \iiint P\left\{1 - \frac{1}{\sqrt{1+\left(\vec{\nabla} w\right)^2}}\right\} d\vec{r} \cong \iiint \frac{P}{2}\left(\vec{\nabla} w\right)^2 d\vec{r}, \tag{1}$$

where, $w(x,y)$ and P represent the displacement of the top surface of the gel and the osmotic pressure, respectively. From the geometric viewpoint, it is possible to rewrite $U_{\text{(compression)}}$ in eq. (1) as follows:

$$U_{\text{(compression)}} = \iiint P\{1 - \cos\theta\} d\vec{r}, \tag{2}$$

where, θ is an angle between the standard layer (x-y plane) and the gel layer, *i.e.*, the angle between the normal directions of the two layers (Fig. 4.5a-i). If we consider that the layer with the least deformity is the standard layer in Tanaka's system, a middle layer, Ω, of the gel will be regarded as the standard in our system with free swelling. That is, θ in eq. (2) represents the angle between the middle layer and the gel layer in our system (Fig. 4.5a-ii). In order to evaluate $\cos\theta$, we set up the local coordinates of which the origin is some point on Ω. We choose this coordinate such that it consists of one outward normal direction and two principal curvature directions with respect to Ω (Fig. 4.5b and Appendix 4.1). First, let us consider a point, R, on Ω. A position vector, $\vec{\varphi}(x,y)$, of R near the origin, O, can be described as $\vec{\varphi}(x,y)=(x,y,z(x,y))$ uniquely. Next, let us consider an inner point, Q, of the gel. According to ref. [25], we can treat the gel as a combination of thin layers, and then, Q is contained in some layer which is named the t-level with a parameter t as shown in Fig. 4.5a. Then, the position vector, $\vec{\phi}(x,y)$ of a point Q can be expressed by the following equation:

$$\vec{\phi}(x,y)=\begin{cases}\vec{\varphi}(x,y)+k(t;h)s(x,y)\vec{n}(x,y), & 0\le t\le h,\\ \vec{\varphi}(x,y)+k(t;h)\bar{s}(x,y)\vec{n}(x,y), & -h\le t<0,\end{cases} \tag{3}$$

where, h, $\vec{n}(x,y)$, and $s(x,y)$ (or $\bar{s}(x,y)$) represent the half-thickness of the gel, an outward normal vector to Ω at R, and a displacement of the top (or bottom) surface with respect to the middle surface, respectively. Additionally, $k(t;h)=\sin(\pi t/2h)$ is constant with respect to x and y. It is then possible to obtain $\cos\theta$ at Q from an inner product of these normal vectors. As a result, the compression energy density, $U^{Q}_{(\text{compression})}$, in Q will be expressed by the following equation (See Appendix 4.2):

$$U^{Q}_{(\text{compression})}=1-\cos\theta=1-\frac{1}{A}. \tag{4}$$

If we supposed that the middle surface morphed into the minimal surface by the large deformation, A in eq. (4) can be calculated as follows:

$$A=\sqrt{\left(\frac{ks_x}{1-k\kappa s}\right)^2+\left(\frac{ks_y}{1+k\kappa s}\right)^2+1}, \tag{5}$$

where, $\kappa > 0$ is a positive curvature of middle surface. Here, at the point Q on the gel layer, the deformation of the gel will occur to suppress the total energy. Thus, the total energy converges to a minimal value (*i.e.*, A becomes bigger) with $s_x^2 + s_y^2 = const.$, then eq. (5) suggests that it is better for $s_y \to 0$ in the top surface because of $k \geq 0$ ($0 \le t \le h$). In contrast, $\bar{s}_x \to 0$ is better in the bottom surface because of $k < 0$ ($-h \le t < 0$). The above discussion does not depend on a choice of the origin on Ω. Therefore, these results suggest that the top (or bottom) surface tends to tilt to the positive (or negative) curvature direction. The directions of the principal curvature are normal to each other, and same applies to the internal properties (such as creases, internal stress, and so on) of the top and bottom of the gel.

According to the above considerations, we can predict the crease pattern on the gel which is in the process of swelling with $\lambda_+ + \lambda_- = 0$. Now, we consider that the middle layer in the process of deformation can be described as $(x,y,z(x,y))$ in the global coordinate system. In particular, we assume that the middle layer is Scherk's minimal surface, *i.e.*, $z(x,y)$ can be described as follows:

$$z(x,y) = \log\left(\frac{\cos y}{\cos x}\right), \quad |x| < \frac{\pi}{2}, |y| \le \frac{\pi}{2}.$$

Then, we can easily obtain the principal curvature directions on the global coordinate system as follows (See Appendix 4.1):

$$\vec{\xi}_\pm = \frac{\tan x \tan y \cos^{-2} y}{\left(1+\tan^2 x+\tan^2 y\right)} \begin{pmatrix} 1 \\ 0 \\ \tan x \end{pmatrix} - \left\{ \frac{\cos^{-2} x \cos^{-2} y}{\left(1+\tan^2 x+\tan^2 y\right)} \mp \sqrt{\frac{\cos^{-2} x \cos^{-2} y}{\left(1+\tan^2 x+\tan^2 y\right)}} \right\} \begin{pmatrix} 0 \\ -1 \\ \tan y \end{pmatrix}. \tag{6}$$

If we consider the continuous crease on the surface as some orbit of the differential equation, $\vec{c}'_\pm(\tau) = \vec{\xi}_\mp$ (τ is a parameter, and prime means the derivative with respect to τ), with an appropriate initial condition, we can check the orbits of the top and bottom that are normal to each other as shown in Fig. 4.6. These above considerations suggest that the creases which are normal to each other can be observed, if the large deformation at the time of swelling has the mean curvature equal to zero.

The theoretical prediction corresponds reasonably well with the above experimental observation, which justified the proposed mechanism. Therefore, these results indicate that surface crease patterns are affected by large three-dimensional shape change induced by geometric swelling mismatch.

4.4 Conclusions

In this study, we have investigated the mechanical instabilities of a thin polyelectrolyte hydrogel disc in the process of fast free swelling. During the swelling process, the gel morphed into a saddle-like shape and then the polygonal surface creases changed to stripe creases due to two swelling mismatches, surface layer/inner layers, and inner disc/outer annulus region. The stripe creases were formed uni-directionally, and were perpendicular to each other at the two surfaces of the sample. From the detail observation of the internal stress analyzed by the orientation of semi-rigid polyanions, we found that both surface creasing and bulk deformation minimize the swelling mismatch. We further demonstrated the surface pattern change of thin hydrogel films fixed onto flat or saddle-shaped substrates and these results confirmed the mechanical coupling of the surface instability and bulk deformation. Under the assumption that the gel morphs into a saddle-like shape with mean curvature of zero, it was theoretically suggested that the gel layer tends to tilt in the one of the principal directions by the minimization of total energy in ref. [25]. The direction of tilt of the gel layer was separated by the middle surface, therefore, the creases on the top and bottom surface were normal each other.

4.5 References

1. J. Wesfreid, H. Brand, P. Monnecille, G. Albinet & N. Boccara, eds., *Propagation in Systems far from Equilibrium,* Springer, 1988.
2. X. Chen and J. Yin, *Soft Matter,* **6,** 5667 (2010).
3. H. Yizhaq, N. J. Balmforth & A. Provenzale, *Physica D,* **195,** 207 (2004).
4. J. Kim, J. A. Hanna, M. Byun, C. D. Santangelo & R. C. Hayward, *Science,* **335,** 1201 (2012).
5. B. Li, Y. P. Cao, X. Q. Feng & H. Gao, *Soft Matter,* **8,** 5728 (2012).

6. E. Hohlfeld & L. Mahadevan, *Phys. Rev. Lett.*, **106,** 105702 (2011).
7. J. Yin, G.J. Gerling & X. Chen, *Acta Biomater.*, **6,** 1487 (2010).
8. R. J. Metzger & M, A, Krasnow, *Science,* **284,** 1635 (1999).
9. T. Savinm N. A. kurpios, A.E. Shyer, P. Florescu, H. Liang, L. Mahadevan & C. J. Tabin, *Nature,* **476,** 57 (2011).
10. M. Arifuzzaman, Z. L. Wu, T. Kurokawa, A. Kakugo & J. P. Gong, *Soft Matter,* **8,** 8060 (2012).
11. M. Ariguzzaman, Z. L. Wu, R. Takahashi, T. Kurokawa, T. Nakajima & J. P. Gong, *Macromolecules,* **46,** 9083 (2013).
12. M. Basa, J. F. Joanny, J. Prost & T. Risler, *Phys. Rev. Lett.* **106.** 1 (2011).
13. D. Chen, L. Jin, Z. Suo & R. C. Hayward, *Mater. Horiz.,* **1,** 207 (2014).
14. M. Guvendiren, S. Yang & J. A. Burdick, *Adv. Funct. Matter.*, **19,** 3038 (2009).
15. V. Trujillo, J. Kim & R. C. Hayward, *Soft Matter,* **4,** 564 (2008).
16. H. Tanaka, H. Tomita, A. Takasu, T. Hayashi & T. Nishi, *Phys. Rev. Lett.,* **68,** 2794 (1992).
17. N. Suematsu, K. Sekimoto & K. Kawasaki, *Phys. Rev. A*, **41,** 5751 (1990).
18. P. C. Lin & S. Yang, *Soft Matter,* **5,** 1011 (2009).
19. E. P. Chan, E. J. Smithm R. C. Hayward & A. J. Crosby, *Adv.Mater.*, **20,** 711 (2008).
20. X. L. Zhu, Y. Zhang, D. Chandra, S. C. Cheng, J. M. Kikkawa & S. Yang, *Appl. Phys. Lett.* **93,** 161911 (2008).
21. X. Jiang, R. Ferrigno, M. Mrksich & G. M. Whitesides, *J. Am. Chem. Soc,* **125,** 2366 (2003).
22. M. Guvendiren, J. A. Burdick & S. Yang, *Soft Matter,* **6.** 2044 (2010).
23. E. Sultan & A. Boudaoud, *J. Appl. Mech.,* **75,** 051002-1 (2008).
24. K. Saha, J. Kim, E. Irwin, J. Yoon, F. Mormin, V. Trujillo, D. V. Schaffer, K. E. Healy & R. C. Hayward, *Biophys. J.,* **99,** 94 (2010).
25. T. Tanaka, S. T. Sun, Y. Hirokawa, S. Katayama, J. Kucera, Y. Hirose & T. Amiya, *Nature,* **325,** 796 (1987).
26. L. Jin, D. Chen, R. C. Hayward & Z. Suo, *Soft Matter,* **10,** 303 (2014).

27. Z. L. Wu, M. Arifuzzaman, T. Kurokawa, H. Furukawa & J. P. Gong, *Soft Matter,* **7,** 1884 (2011).
28. E. J. Vandenberg, W. R. Diveley, L. J. Filar, S. R. Pater & H. G. Barth, J. *Polym. Sci. Part A: Polym. Chem.,* **27,** 3745 (1989).
29. T. Funaki, T. Kaneko, K. Yamaoka, Y. Oshedo, J. P. Gong, Y. Osada, Y. Shibasaki & M. Ueda, *Langmuir,* **20,** 6518 (2004).
30. Y. Shigekura, Y. M. Chen, H. Furukawa, T. Kaneko, D. Kaneko, Y. Osada & J. P. Gong, *Adv. Mater.,* **17,** 2695 (2005).
31. M. F. Islam, M. Nobili, F. Ye, T. C. Lubensky & A. G. Yodn, *Phys. Rev. Lett.* **95,** 148301 (2005).
32. R. Takahashi, Z. L. Wu, M. Arifuzzaman, T. Nonoyama, T. Nakajima, T. Kurokawa & J. P. Gong, *Nat. Commun.,* **5,** 4490 (2014).
33. A. Tagaya, H. Ohkita, M. Mukoh, R. Sakaguchi & Y. Koike, *Science,* **301,** 812 (2003).
34. Y. Klein, E. Efrati & E. Sharon, *Science,* **315,** 1116 (2007).
35. M. Pezzulla, S. A. Shillig, P. Nardinocchi & D. P. Holmes, *Soft Matter,* **11,** 5812 (2015).

4.6 Figures

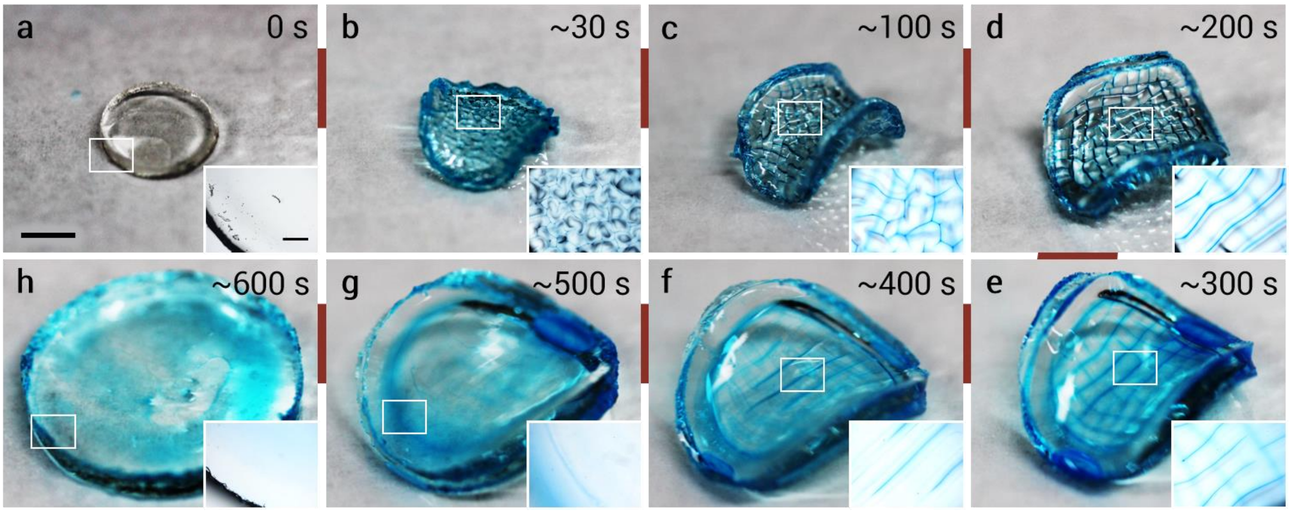

Figure 4.1 | Evolution of surface crease pattern and bending of a disc shape polyelectrolyte hydrogel during free swelling in water. After the appearance of the isotropic polygonal surface crease, stripe-crossed surface pattern and saddle-like bending of the gel were observed. To observe clearly the shape and the boundary of surface pattern, the as-prepared hydrogel was swelled in water containing 0.05 wt% Alcian blue. Each inset in lower right corner reveals the clear surface pattern of the top surface observed with an optical microscope. All the images and insets are shown in the same scale as shown by the scale bars in 0 s (left: 3 mm, right: 500 μm). The dimension of the as-prepared gel was 6 mm (*D*) × 1 mm (*T*). Even the absence of Alcian blue, we observed exactly the same swelling behavior.

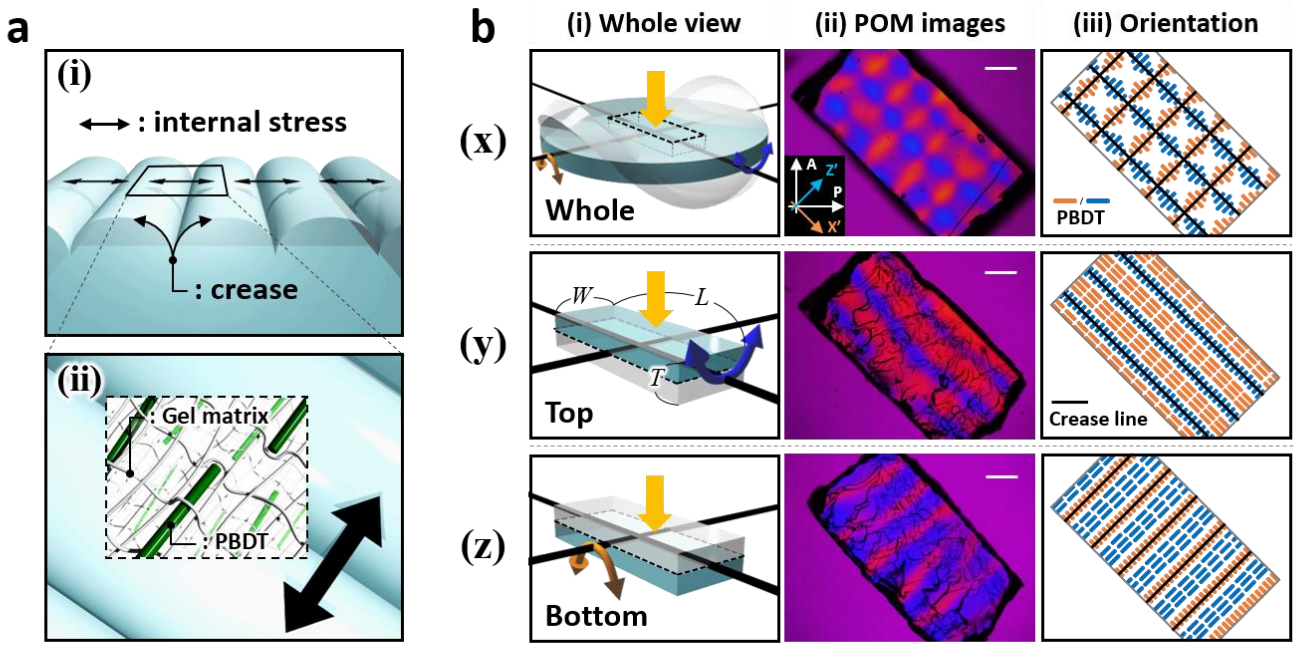

Figure 4.2 | Polarized optical microscope (POM) observation of birefringence patterns due to the orientation of the rigid molecules (PBDT) induced by a fast-heterogeneous swelling of a PDMAPAA-Q hydrogel. (**a**) Schematic illustrations for the internal stress induced by creasing instability (i) and PBDT orientation inside gel matrix (ii). PBDT molecules were sensitively oriented along with the internal. stress and fixed by polyion complexation even after swelling. (**b**) Birefringence pattern observation at equilibrium swollen state. The schematic illustration in (b-x-i) represents the equilibrium state of the gel, where the orange and blue arrows represent the bending direction of the saddle shape during swelling. The gel was cut from the disc-shape sample into specific dimensions about 7 mm (*L*) ×4 mm (*W*) × 2 mm (*T*) (b-x-i). To observe the birefringence pattern on the two surfaces of the gel separately, the sample of (b-x-i) is sliced into two sheets at the middle of the thickness direction to obtain the upper surface (b-y-i) and lower surface (b-z-i). The polarized optical microscope (POM) images of the (b-i) were observed from the thickness direction under crossed polarizers with 530 nm tint plate as shown in column (b-ii). Illustrations in column (b-iii) indicate the PBDT molecular orientation in the hydrogel and crease pattern during swelling. The POM observation confirms that the rectangular birefringence pattern of (b-x-i) sample is the result of the overlapping of the perpendicular aligned birefringence lines on two surfaces of the sample. All the POM images have the same scale bar (1 mm). Key: A, analyzer; P, polarizer; X’ and Z’, fast and slow axis of the tint plate, respectively.

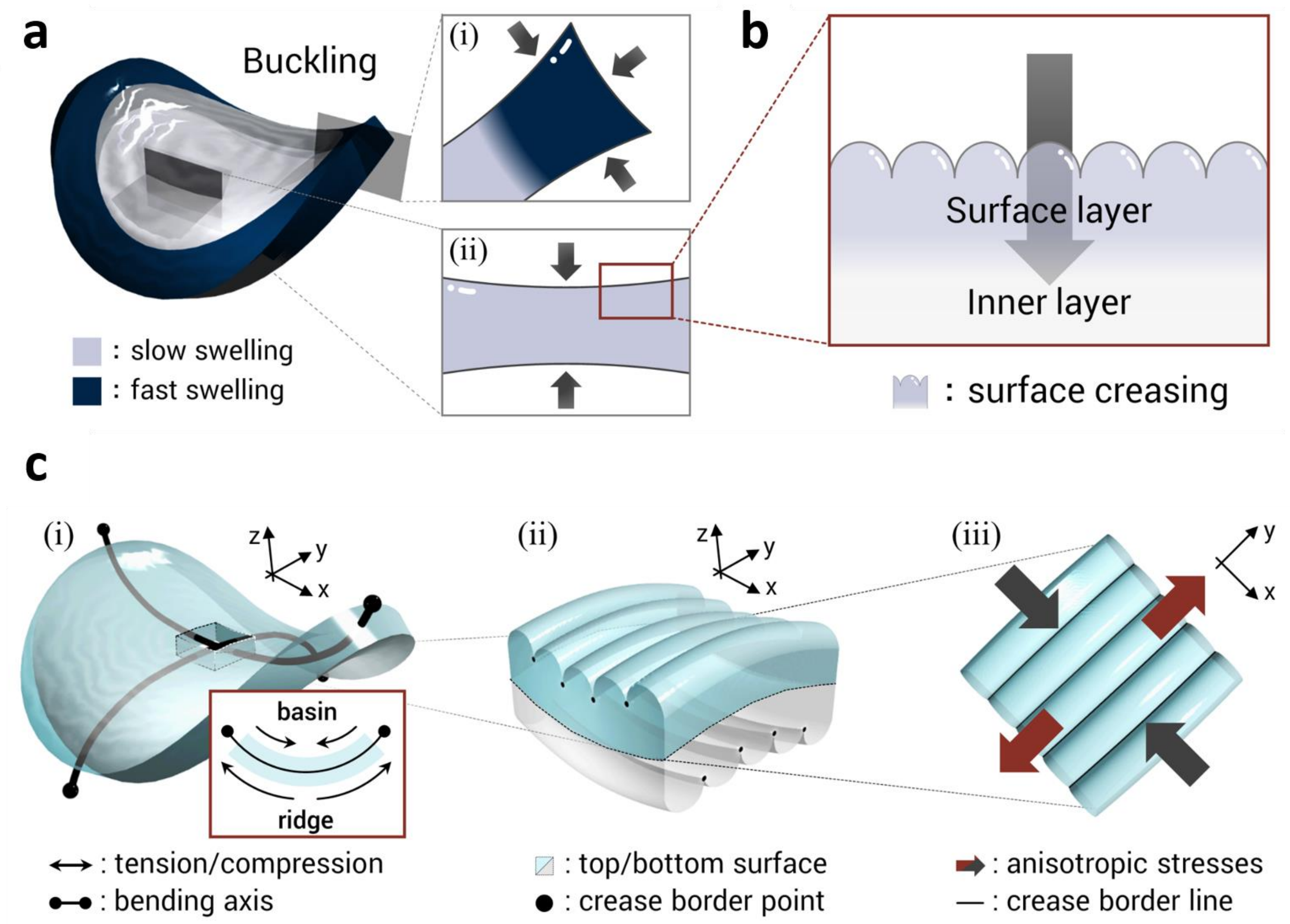

Figure 4.3 | Schematic illustration of two kinds of swelling mismatch and their coupling to induce anisotropic surface creases during fast free swelling of a polyelectrolyte gel. (**a**) Swelling mismatch between the annulus (dark blue) and the inner disc (light blue) induced by the difference in swelling kinetics between the annulus and the inner disc. The annulus can absorb water from three directions (a-i), while the inner disc can only absorb water from two directions (a-ii) as shown by arrows in (a-i, ii). This swelling mismatch induces a saddle-like bending to minimize the swelling mismatch. (**b**) Swelling mismatch between the surface layer (light blue) and inner layer (gray) induced by the difference in swelling kinetics between the surface layer and the inner layer. Surface creasing instability is induced to minimize this swelling mismatch. (**c**) The two mechanical instabilities are coupled to induce anisotropic surface crease pattern. Bending of the sample exerts a tension to the ridge and a compression to the basin (c-i). The saddle-like bending induces anisotropic stresses, perpendicularly oriented, on the two surfaces of the sample (c-ii), which changes the isotropic polygonal crease patterns into the anisotropic stripe crease patterns aligned in right angles on the two surfaces (c-iii).

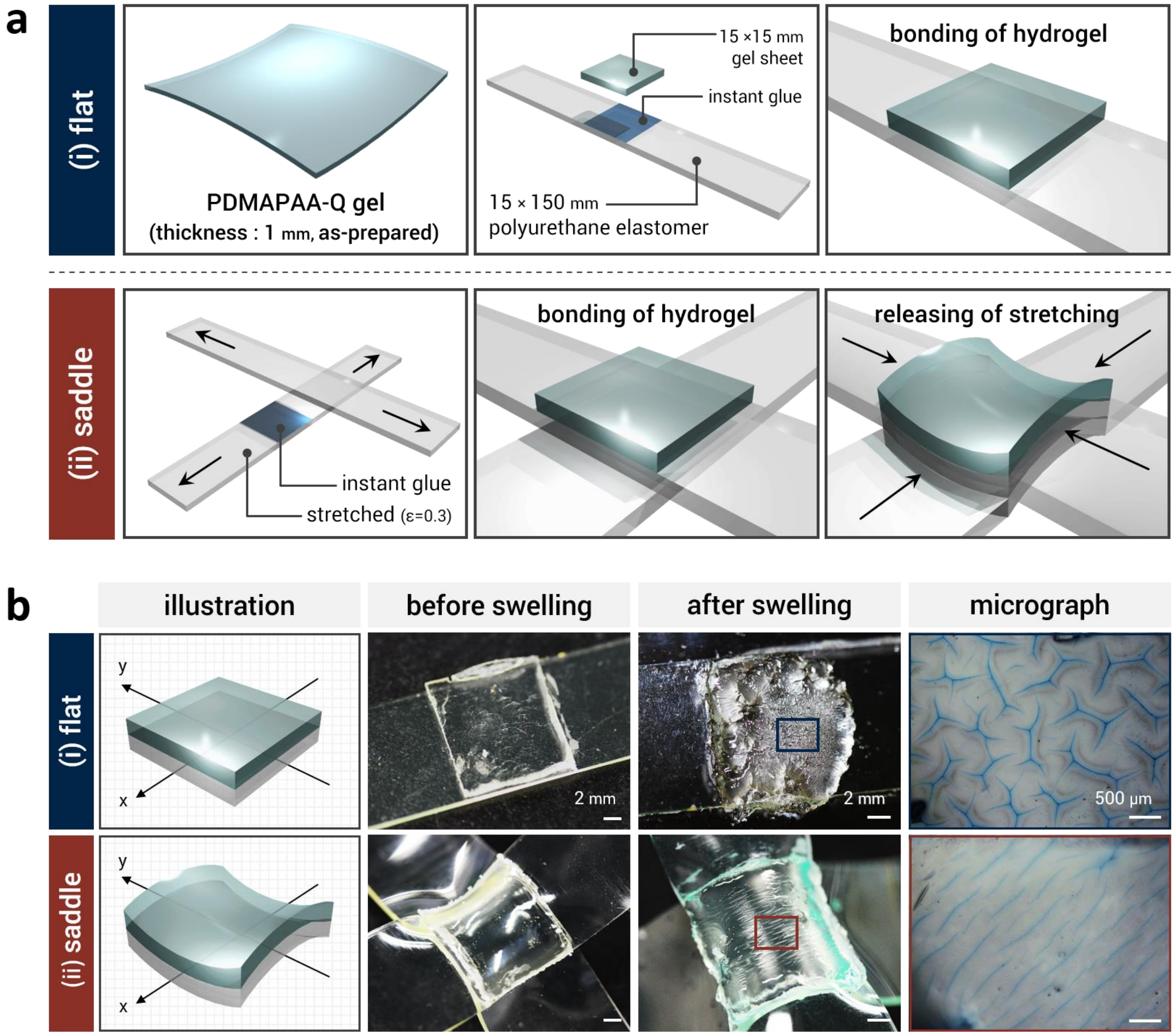

Figure 4.4 | Experimental demonstration of the mechanical coupling of surface crease pattern with the saddle-like bending. (**a**) Preparation method of a thin hydrogel sheet with the flat (i) or saddle shape (ii) induced by mechanical mismatching with the substrate. (**b**) Schematic illustration, photographs of before or after swelling, and micrographs of swollen samples on flat (i) and saddle shape (ii) substrate, respectively. Left column is a schematic illustration of the hydrogel-coated unswellable substrate, where the blue part represents the hydrogel sheet (thickness: 500 μm), while the gray part indicates the polyurethane rubber which is the unswellable substrate. The micrographs presented in right column, observed with an optical microscope, show the surface morphology of the gel. In order to observe clearly the boundary of the surface pattern, the coated hydrogel sheets were swollen in water containing 0.05 wt % Alcian blue. After reaching the equilibrium state (~600 s), isotropic polygonal-like pattern and anisotropic straight-grained pattern were observed on the surface of (b-i) and (b-ii), respectively. All the micrographs have the same scale bar (500 μm). After swelling, the thickness of gel reached to 1.15 mm. The curvature of saddle is 0.155 [1/mm]

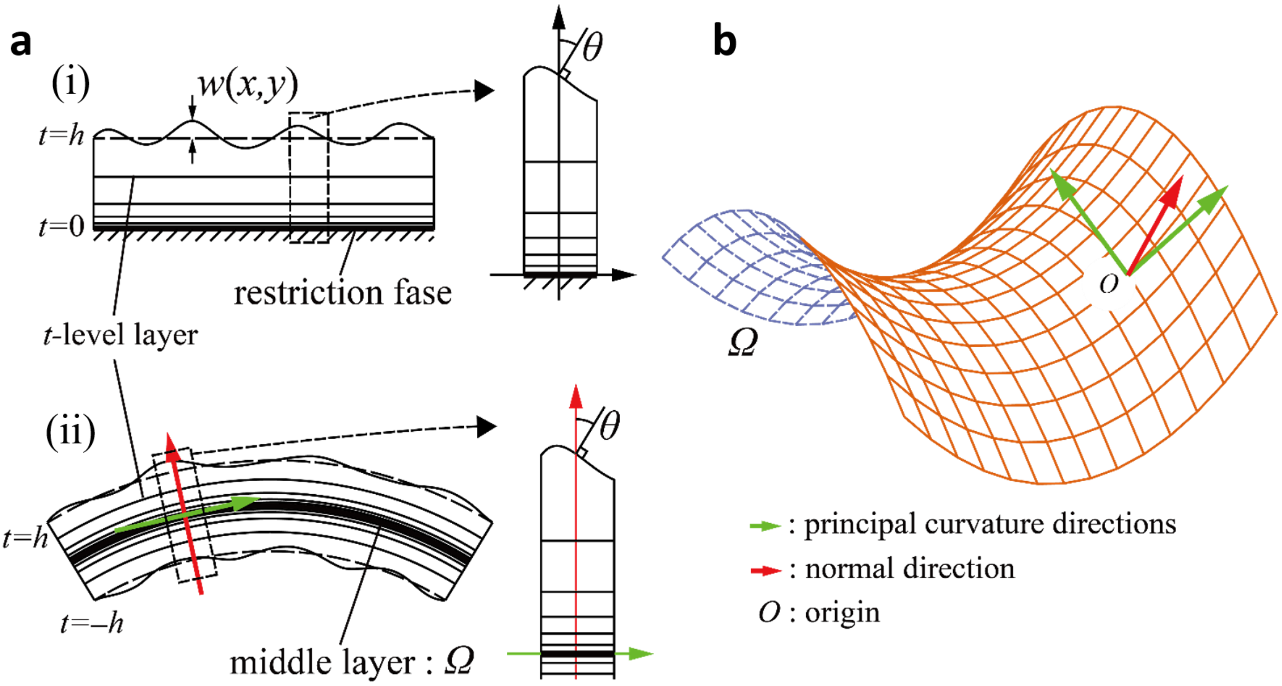

Figure 4.5 | Schematic illustration of the model for describing the mechanical instability of gel sheet during free swelling. (**a**) The gel is treated as the combination of thin layers which are named *t*-level. In particular, the gel has the restriction face in the case of (i), and the gel passes through the process of the free swelling in the case of (ii). In both cases, θ means the angle between the layer with the least deformity and the *t*-level layer. (**b**) The local coordinates on the middle layer, Ω, of the free swelling gel. The green arrows correspond to the directions of the two principal curvatures, and the red arrow corresponds to the direction of the outward normal at the origin, *O*, on restriction phase.

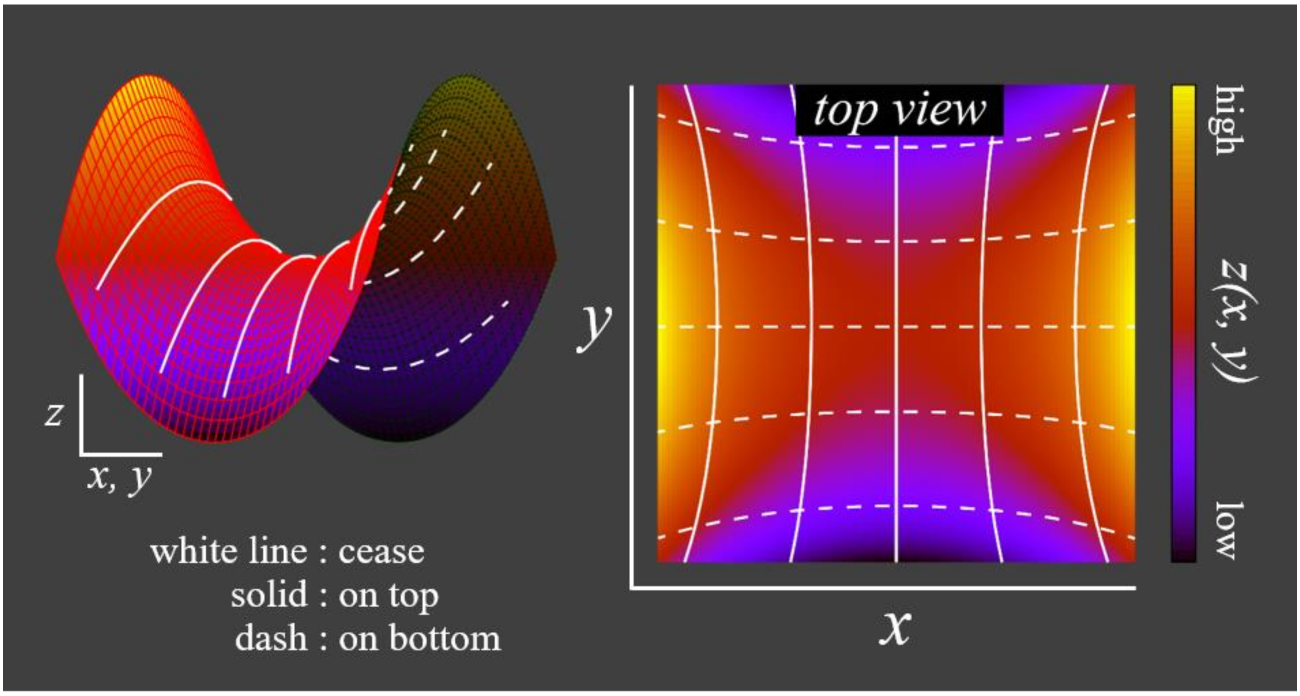

Figure 4.6 | Creases on the Scherk's minimal surface. The colored surface is the Scherk's minimal surface, and the solid and dashed lines represent the creases of the top and bottom surfaces, respectively. These lines are the orbits obtained by the calculation of the differential equation from Eq. 6. On any intersection, these lines are at right angles to each other when viewed from the normal direction.

4.7 Appendixes

Appendix 4.1 |

Under the suitable coordinate system, we assume that the middle layer can be expressed as follows by using two parameters, (*x, y*):

$$\vec{\Phi}(x,y)=\begin{pmatrix} u(x,y) \\ v(x,y) \\ w(x,y) \end{pmatrix}.$$

Then, the first fundamental quantities (*E, F, G*) and second fundamental quantities (*L, M, N*) of the middle layer can be described as follows:

$$E=\left\langle \vec{\Phi}_x \cdot \vec{\Phi}_x \right\rangle,\quad F=\left\langle \vec{\Phi}_x \cdot \vec{\Phi}_y \right\rangle,\quad G=\left\langle \vec{\Phi}_y \cdot \vec{\Phi}_y \right\rangle,$$

$$L=\left\langle \vec{\Phi}_{xx} \cdot \frac{\vec{\Phi}_x \times \vec{\Phi}_y}{\left|\vec{\Phi}_x \times \vec{\Phi}_y\right|} \right\rangle,\quad M=\left\langle \vec{\Phi}_{xy} \cdot \frac{\vec{\Phi}_x \times \vec{\Phi}_y}{\left|\vec{\Phi}_x \times \vec{\Phi}_y\right|} \right\rangle,\quad N=\left\langle \vec{\Phi}_{yy} \cdot \frac{\vec{\Phi}_x \times \vec{\Phi}_y}{\left|\vec{\Phi}_x \times \vec{\Phi}_y\right|} \right\rangle.$$

And, mean curvature (*H*) and Gaussian curvature (*K*) defined by the principal curvatures ($\lambda_\pm(x,y)$) are calculated as follows by using *E, F, G, L, M,* and *N*:

$$H=\frac{\lambda_+ + \lambda_-}{2}=\frac{GL+EN-2FM}{2\left(EG-F^2\right)},$$

$$K=\lambda_+\lambda_-=\frac{LN-M^2}{EG-F^2}.$$

If H=0 and K<0, the principal direction ($\vec{v}_\pm$) which is respect to $\lambda_\pm(x,y)$ can be obtained as follows:

$$\vec{v}_\pm=\frac{FN-GM}{EG-F^2}\vec{\Phi}_x+\left(\frac{GL-FM}{EG-F^2}\mp\sqrt{\frac{M^2-LN}{EG-F^2}}\right)\vec{\Phi}_y.$$

Then, an inner product of principal directions is 0 (*i.e.*, $\left\langle \vec{v}_+ \cdot \vec{v}_- \right\rangle$=0). Therefore, we can confirm that the principal directions are orthogonal to each other at any point in our system. That is, it is possible to choose a local orthogonal coordinate system as including the principal directions for any point on *Ω*.

Appendix 4.2 |

Here, we consider about the integral function of the compression energy. If we choose the local orthogonal coordinate system as including the principal directions, (x and y), the middle layer can be expressed by $\vec{\varphi}(x,y)=(x,y,w(x,y))^T$. In this case, $w(x,y)$ has the following futures, because the plane which consists of the principal directions contacts with the middle layer at the origin.

$$w_x(0,0)=w_y(0,0)=w_{xy}(0,0)=0,\quad w_{xx}(0,0)=\lambda_+, w_{yy}(0,0)=\lambda_- . \tag{S1}$$

Then, the outward unit normal vector at the origin of the middle layer ($\vec{n}(x,y)$) is given by

$$\vec{n}(x,y)\Big|_{(x,y)=(0,0)}=\left.\frac{\vec{\varphi}_x\times\vec{\varphi}_y}{\left|\vec{\varphi}_x\times\vec{\varphi}_y\right|}\right|_{(x,y)=(0,0)}=\begin{pmatrix}0\\0\\1\end{pmatrix}. \tag{S2}$$

Now, let us consider about the outward unit normal vector to t-level layer ($\vec{\eta}(x,y)$) at origin. From eq (3), the following equations can be obtained:

$$\vec{\phi}_x(x,y)=\vec{\varphi}_x(x,y)+ks_x(x,y)\vec{n}+ks(x,y)\vec{n}_x,$$

$$\vec{\phi}_y(x,y)=\vec{\varphi}_y(x,y)+ks_y(x,y)\vec{n}+ks(x,y)\vec{n}_y,$$

where, k:=sin($\pi t/2h$) is constant with respect to (x,y). Therefore, the following equations can be obtained with the considering eq (S1).

$$\vec{\phi}_x(x,y)\Big|_{(x,y)=(0,0)}=\begin{pmatrix}1-k\lambda_+ s\\0\\ks_x\end{pmatrix},\quad \vec{\phi}_y(x,y)\Big|_{(x,y)=(0,0)}=\begin{pmatrix}0\\1-k\lambda_- s\\ks_y\end{pmatrix}.$$

As a result, we can describe the outward unit normal vector ($\vec{\eta}(x,y)$) to t-level layer at (x,y)=(0,0) as follows:

$$\vec{\eta}(x,y)=\frac{\vec{\phi}_x\times\vec{\phi}_y}{\left|\vec{\phi}_x\times\vec{\phi}_y\right|}=\frac{1}{\sqrt{\Psi_1^2+\Psi_2^2+\Psi_3^2}}\begin{pmatrix}\Psi_1\\\Psi_2\\\Psi_3\end{pmatrix}, \tag{S3}$$

where,

$$\begin{pmatrix}\Psi_1\\\Psi_2\\\Psi_3\end{pmatrix}=\begin{pmatrix}-k(1-k\lambda_- s)s_x\\-k(1-k\lambda_+ s)s_y\\(1-k\lambda_+ s)(1-k\lambda_- s)\end{pmatrix}. \tag{S4}$$

Finally, from eqs. S2-S4, we can calculate A^{-1} in the main text as follows:

$$\langle\vec{n}\cdot\vec{\eta}\rangle=\frac{1}{A}=\frac{1}{\sqrt{\Psi_1^2+\Psi_2^2+\Psi_3^2}}\left\langle\begin{pmatrix}0\\0\\1\end{pmatrix}\cdot\begin{pmatrix}\Psi_1\\\Psi_2\\\Psi_3\end{pmatrix}\right\rangle=\left\{\left(\frac{ks_x}{1-k\lambda_+ s}\right)^2+\left(\frac{ks_y}{1-k\lambda_- s}\right)^2+1\right\}^{-1/2}.$$

CHAPTER 5

Creating Macro-scale Hydrogel Composites with Low Melting Point Alloys (LMA)

5.1 Introduction

Composite materials, consisting of a matrix and a reinforcing phase, can show hybridized characteristics of each component, including physical, mechanical, and electrical properties[1-3]. This ability makes well-tuned composite materials uniquely desirable for specific applications in diverse fields, which may require properties that are unattainable with a single material. In particular, hydrogels exhibit a variety of properties that make them extremely useful as a matrix material, such as biocompatibility[3,4], high water content[5,6], high flexibility[7,8], permeability[9,10], antifouling[11,12], low friction[13] and optical clarity[14,15]. However, a serious problem has limited the use of hydrogels as a matrix material in combination with rigid reinforcements: stress-induced deformation can occur due to swelling mismatch between the hydrogel and the solid phase. In general, the volume of hydrogels can change dramatically from the as-prepared state by expelling water to or absorbing water from the environment[16-18], causing the hydrogel-solid composites to undergo strain resulting in surface creasing or bulk deformation, at best, and delamination or rupture, at worst[19-21]. To avoid or reduce deformation due to swelling mismatch, intense efforts have been devoted as follows: (1) relatively low-swelling hydrogels were used as a matrix to reduce the mismatch[22-24]; furthermore (2) geometrically compliant materials that could deform by sliding (steel wool or glass-woven fibers), or stretching (nanometer scale reinforced gels)[22-25], and (3) mechanically compliant materials that could stretch (such as elastomers), were used as reinforcing materials to reduce the mismatch[26]. However, these approaches merely limit the impact of the induced stress, and are not fundamental solutions to swelling mismatch. As a result, the components of hydrogel-solid composites have been highly selective. A universal strategy and practical methods for fabricating diverse hydrogel-based composites is strongly required for versatile applications.

To overcome such limitations, here, we develop a new design concept and a simple fabrication method to prepare “macro-scale” hydrogel composites, consisting of a heterogeneous rigid phase within a soft hydrogel matrix, which can relieve swelling mismatch, preventing stress-induced physical deformation. A Low-Melting Point Alloy (LMA) that can transform from a load-bearing solid state to a free-deformable liquid state at relatively low temperature (Fig. 5.1 and Fig. 5.2a), was processed into a honeycomb-shaped grid (Fig. 5.2b) and used as a reinforcement skeleton in the hydrogel-based composite. Due to the solid-liquid phase transition of LMAs, dramatic stiffness changes have been obtained in elastomer-based LMA composites[27-29]. Inspired by these composites, we attempted to release the stress caused by the swelling mismatch between the LMA and hydrogel by activating the solid-to-liquid phase transition. To verify the universality of this concept, both deswelling and swelling hydrogels, relative to their as-prepared states, were used as matrix materials. After applying a thermal stimulus, the volume of the melted LMA was spontaneously adjusted by the elasticity of the hydrogel matrix and the stress was released. This method results in a hydrogel composite reinforced with a rigid skeleton, free of stress.

This fabrication process enables the production of composite materials with exceptional mechanical and physical properties. The resulting hydrogel composites exhibited high stiffness, similar to the LMA reinforcing phase. When the strength of the matrix was comparable to the LMA reinforcement, toughness of the composites was significantly increased. In addition, we performed experiments highlighting the superior hybridized properties of LMA composite hydrogels, including shape memorable ability, dynamic stiffness control, and thermal healing ability. Importantly, at strains less than 200%, these composites are capable of dissipating extremely large amounts of energy, with complete recovery. Finally, taking advantage of the characteristic properties of hydrogels and the LMA, we further explored unique functional abilities, such as performing electro-chemical reactions in the hydrogel matrix and creating channel structures in the hydrogel for fluidic devices. Through these experiments, we have discovered that the creation of “macro-scale” reinforced composite hydrogels by the incorporation of an LMA scaffold results in a material that not only has superior mechanical properties, but also possesses multiple functional abilities that cannot be achieved with neat hydrogels. This work presents a promising pathway to develop hydrogel composites, which may find use in the fields of soft robotics, wearable electronics, and biocompatible functional materials.

5.2 Experiments

5.2.1 Materials

2-ureidoethyl methacrylate (UMA) was kindly provided by Osaka Organic Chemical Co., Ltd. and Methacrylic acid (MAA) was purchased from Wako Pure Chemical Industries, Ltd. These monomers were used as received for synthesizing the deswellable tough hydrogel. Acrylamide (AAm) (Jundei Chemical Co., Ltd) was recrystallized from chloroform and used as monomer for synthesizing the swellable hydrogel. *N,N'*-Methylenebis (acrylamide) (MBAA; Tokyo Kasei Co., Ltd.), as a cross-linker for both UMA- and AAm-based gels, was recrystallized from ethanol. 2-Oxoglutaric acid (α-keto) (Wako Pure Chemical Industries, Ltd.), as a UV initiator for the polymerization, was used as received. Dimethyl sulfoxide (DMSO) (Wako Pure Chemical Industries, Ltd.) was used as received as the solvent of the PUMA pre-gel solution. A Low Melting-point Alloy (LMA), U-alloy 60 (Asahi-metal Co., Ltd.) was used as received. Sodium chloride phenolphthalein ethanol solutions and pyrrole (Wako Pure Chemical Industries, Ltd.), were used as received for the electro-chemical reaction experiments. Uranine (KANTO Chemical Co., INC.), Indian ink (KURETAKE Co., Ltd.) and Methyl blue (Wako Pure Chemical Industries, Ltd.) were used as received for diffusion experiments in the hydrogel fluidic device.

5.2.2 Synthesis of LMA composite hydrogels

A honeycomb-shaped LMA skeleton was prepared via a silicone molding process. To make the silicone mold, a plastic inverse mold was 3D printed (AGILISTA-3000, Keyence Co.). Subsequently, the plastic mold was washed with ethanol and deionized water. The silicone mold precursor solution was prepared by mixing Silopren (RTV-2K 1406, Momentive Performance Materials Inc.) and curing catalyst (R-14, Momentive Performance Materials Inc.) at a mixing ratio of 100:1. Immediately, the precursor solution was poured into the plastic mold and the mold was placed on a level table for 48 hours to cure the silicone. To prepare the LMA curing cell, the resulting silicone mold was sandwiched between two clean glass plates and fixed by metal clips. The mold was heated to 80°C and melted LMA heated by hot water (80°C) was injected into the mold using a syringe. After cooling at 25°C for 15 minutes, the solid LMA skeleton was removed from the mold and stored in low-humidity conditions before being used for experiments. Then, to prepare the reaction cell, LMA skeletons were fixed nominally in the middle of two glass plates by using two 1 mm thick silicone spacers (total thickness ~2 mm). For the PUMA system, a DMSO solution containing 2.5 M monomers UMA and MAA (0.8 : 0.2 molar ratio), 0.1 mol% MBAA as a chemical cross-linker and 0.1 mol% α-keto as an initiator (all in relative to the monomer) were prepared.

The pre-gel solution was poured into the reaction cells. Photo-induced free radical polymerization was carried out under argon atmosphere with a UV lamp for 10 h (UV light intensity was 3.9 mW/cm^2). After that, the as-prepared sample was cut into specific dimensions ($l_0 \times w_0 \times t_0 = 50 \times 10 \times 2\ mm^3$) and immersed in a large amount of pure water for 1 week to allow the gel to reach equilibrium. After that, the sample was annealed in hot water (80°C) for 1 minute to remove the volume mismatch. Then, the sample was cooled down to room temperature and kept in water.

For the PAAm system, the composite was prepared in the same procedure from an aqueous solution of pre-gel. For mechanical tests and swelling ability tests, an aqueous solution containing 2.5 M AAm monomer, 0.1 mol% MBAA, and 0.1 mol% α-keto was used. For hydrogel fluidic device tests, an aqueous solution containing 4 M AAm, 0.02 mol% MBAA, and 0.1 mol% α-keto was used.

For the pristine gels, the samples were prepared at the same formulation and polymerization conditions as those of the composites for the mechanical tests in the absence of the LMA skeletons.

5.2.3 Size change of pristine gels and composites

The as-prepared samples were cut into specific dimensions ($l_0 \times w_0 \times t_0$ = 50×10×2 mm) and immersed in a large excess of pure water for 1 week to allow the gels to reach the equilibrium swelling conditions. To verify the isotropy of the size changes of the pristine gels and composites, the three dimensions (length (l), width (w) and thickness (t)) of the pristine gels and composites equilibrated in deionized water were measured and compared to the as-prepared dimensions of the samples. Sizes of the composites were measured after annealing of the samples. The size change in relative to the as-prepared state for each dimension was estimated. The volume change in relative to the as-prepared state, V/V_0, was calculated from the size changes in the three directions.

To verify the isotropy of the local dimension changes of the LMA honeycomb in the composites, the three dimensions (interval (a), width (b) and thickness (c)) of the honeycomb in the annealed samples were measured and compared to the as-prepared dimensions of the samples ($a_0 \times b_0 \times c_0$ = 2×0.5×0.5 mm). Then, the local dimension change in relative to the as-prepared state for each dimension was estimated and compared with the global dimension change.

5.2.4 Mechanical testing

Uniaxial tensile tests were performed on water-swollen composites, pristine gels, and the neat LMA skeletons using a tensile-compressive tester (Instron 5965 type universal testing system). The annealed PUMA composite and pristine gels were prepared with the following dimensions, 16×7.5×1.5 mm; 16 mm was the gauge length. The annealed PAAm composite and pristine gels were prepared with the following dimensions, 32×15×3 mm; 32 mm was the gauge length. Two sizes of LMA skeletons (16 ×5.2×0.38 mm, same dimensions as the LMA skeleton in the PUMA composite gel after annealing; 32×10.52×0.75 mm, same dimensions as the LMA skeleton in the PAAm composite gel after annealing) were prepared. All the samples were stretched along the length direction of the samples at an extension rate of 100 mm/min. Tensile stretch ratio, λ, is defined as l/l_0, where l_0 and l are the length of the gel before and during elongation, respectively.

5.2.5 Thermal response of composites gels

To compare Young's modulus and bending modulus of composites at low and high temperature, uniaxial tensile tests and three-point bend tests were performed in cold (25℃) and hot (80℃) water. For the tensile tests, PUMA composites (16×7.5×1.5 mm) and PAAm composites (32×15×3 mm) were used and the tests were performed by a Tensilon machine (RTC-1310A, Orientec Co.) at a crosshead displacement velocity of 100 mm/min.

Three-point bend tests were performed on a custom-built testing apparatus. PUMA composites (16×7.5×1.5 mm) and PAAm composites (32×15×3 mm) were prepared, and the length between bottom points is 24 mm. The testing rate was 30 mm/min.

The cyclic loading/ unloading tensile test for evaluating the thermal healing ability of the composites was performed to one sample repeatedly by using the Instron 5965 type universal testing system. The PUMA composite and pristine gels were stretched to strain $\varepsilon = 0.5 – 2.5$ at a velocity of 100 mm/min at room temperature. Then, samples were returned to the initial displacement immediately at the same velocity as stretching. After each loading and unloading test, the sample were immersed in the hot (80℃) water for 1 minute, and subsequently immersed in cold (25℃) water for 1 minute before the next loading and unloading test. The energy dissipation was estimated from the hysteresis area, U_{hys} by:

$$U_{hys} = \int_{\varepsilon=0}^{\varepsilon=0.5-2.5} (\sigma_{load} - \sigma_{unload}) d\varepsilon$$

Where σ_{load} and σ_{unload} are the stress during loading and unloading, respectively.

5.2.6 Electro-chemical reaction in LMA composites hydrogels

The PAAm composite system was used. For electro-reduction, the PAAm composite gels were immersed in 0.15 M NaCl solution containing 1 wt% phenolphthalein ethanol solution for 24 hours. The internal LMA skeleton was connected to the negative electrode of a power supply unit and a flat stainless steel plate was connected to the positive electrode of a power supply unit. Then, the composite gel was placed on the stainless-steel plate and electrolysis was performed by applying voltage (3V) for 1 minute. For electro-polymerization, the PAAm composite gels were immersed in 0.15 M NaCl solution containing 1 wt% pyrrole solution for 24 hours. The internal LMA skeleton was connected to the positive electrode of a power supply unit and a flat stainless steel plate was connected to the negative electrode of a power supply unit. Then, the composite gel was placed on the stainless-steel plate and electrolysis was performed by applying voltage (3V) for 1 minute.

5.2.7 Preparation and testing of the hydrogels fluidic device

The PAAm composite system was used. The PAAm composite samples were immersed in hot (80°C) water to melt the internal LMA skeleton. The liquid LMA was squeezed out from the hydrogel matrix by air pressure with a syringe. A dye solution (0.1 wt% Uranine aqueous solution) was prepared and injected into the hydrogel fluidic device. After 3 minutes, the device was observed from the top by an optical microscope (Nikon, Eclipse, LV100POL) to verify the diffusion of the dye molecules into the hydrogel matrix. A mixture of dye solution (0.1 wt % Uranine aqueous solution) and Indian ink (0.1 wt %) were prepared and injected into the device. After 3 minutes, the device was observed from the top by an optical microscope to verify that only the dye molecules diffused into hydrogel matrix, and the Indian ink colloidal particles remained concentrated in the channels.

To investigate the mesh size of the PAAm gel for the hydrogel fluidic device, compression tests were performed on the as-prepared PAAm gel of diameter 15.7 mm and thickness 3 mm. From the slope of the stress-strain curve, Young's modulus, E was estimated as 22.2 ± 4.1 kPa. Then, the mesh size, ξ_0 of the PAAm network of as-prepared gel was calculated by the following equation[39],

$$\xi_0 = (\frac{3k_BT}{E})^{1/3}$$

Where k_B and T were the Boltzmann constant and temperature (K), respectively. The mesh size of the swollen PAAm gel, ξ was estimated from following equation.

$$\xi = \xi_0 \frac{l}{l_0}$$

To investigate the capillary force of the hydrogel fluidic channels, the PAAm gel (4 M AAm, 0.02 mol% MBAA, and 0.1 mol% α-keto) with linear channels of varying dimension (cross-sectional shape: square, width: from ~0.75 to ~2.5 mm, length : 100 mm) were fabricated by the above mentioned method. Then, the sample was placed in a dye solution containing 0.1 wt% methyl blue, where capillary forces caused the solution to travel vertically up the columns, and the height of each column was measured. The relationship between the width of the channels, a (mm), and height of the columns, h (mm), were plotted (Fig. 5.9b-iv). For comparison with theoretical values, a calculated curve was inserted in the plot by following equation[40],

$$4\mathrm{a} \times \mathrm{T} \cos\theta = a^2 h \times \rho \times g$$

$$\Leftrightarrow h = \frac{4T cos\theta}{a\rho g}$$

Where T, θ, ρ, and g are the surface tension of water (N/m), the contact angle of water to PAAm gel (same surface condition as the surface of the hydrogel channel), the density of water (kg/m^3), and the acceleration of gravity (N/kg), respectively.

By taking the values from reference[41-43] : T = 0.073 N/m, ρ = 1000 kg/m^3, and g = 9.8 N/kg, and the value measured from the independent experiment at 20 °C: θ = 11.6º (Fig. 5.9b-i), the calculated curve was obtained as follows.

$$\mathrm{h} = \frac{29.2}{a}$$

5.3 Results & discussion

5.3.1 Creation of macro-scale hydrogel composites without swelling mismatch

Any change in volume, either swelling or deswelling, of the hydrogel matrix from its synthesis state will induce stress at the interface with the reinforcing phase of the composite. To investigate whether we can relieve this mismatch in hydrogel composites, both deswelling (releases water from the as-prepared state) and swelling (absorbs water from the as-prepared state) hydrogel matrices were prepared from poly(2-ureidoethyl methacrylate)-co-(methacrylic acid) (PUMA) and polyacrylamide (PAAm) respectively, as model systems to produce Hydrogel-LMA composites (Fig. 5.3). Combined with a honeycomb-shaped LMA skeleton as a reinforcing phase (Fig. 5.2b), 50-mm-long and 10-mm-wide rectangle-shaped samples with a cross-sectional thickness of 2 mm were synthesized (Fig. 5.2c and Fig. 5.2d). From the cross-section view in the inset of Fig. 5.2d, the LMA skeleton was fixed nominally in the middle of the gel matrix (the insets show the PUMA composite, and the appearance of the PAAm composite was similar). After immersing the as-prepared composite gels in pure water for 1 week to allow the gels to reach the equilibrium state, both composite gels exhibited large stress-induced deformation due to the swelling mismatch between phases caused by the change in hydration of the hydrogel matrix as shown in Fig. 5.2e-i. Specifically, the PUMA composite showed buckling and the PAAm composite showed surface creasing due to contraction of PUMA and swelling of PAAm in water, respectively. To release these stress-induced deformations, the samples were immersed in hot water (80°C) causing the LMA to undergo a solid-liquid phase transition. As expected, the LMA skeleton was transformed from the load-bearing solid state to the free-deformable liquid state (Fig. 5.1). Thereafter, the swelling mismatch of the composites were spontaneously released, as shown by the squeezing out of LMA from the PUMA composite and the pore formation in the LMA of the PAAm composite (Fig. 5.2e-ii). Note that the PAAm composite gel was subsequently refilled with additional LMA to recover a continuous LMA phase (Fig. 5.2e-iii).

To verify that all induced stress was completely released, the volume change of the composites and pristine gels were compared for both systems. As shown in Fig. 5.2f, for both systems, there is little difference in volume change (from initial to equilibrium state) for the composite and pristine gels, indicating that macro-scale composites with LMA phases can successfully release their induced stress. The size changes of length, width, and thickness relative to those of the as-prepared state were the same in both pristine and composite gels (the PUMA system was ~0.75 and the PAAm system was ~1.5, respectively), which indicates that they exhibited isotropic deswelling or swelling (Fig. 5.4a). Additionally, the size changes in the local honeycombs were also investigated for both PUMA and PAAm systems (Fig. 5.4b), and were measured as ~0.75 and ~1.5, respectively. These values were the same as the global size change of the composites, demonstrating that the local mismatch was also released.

5.3.2 Enhanced mechanical properties of macro-scale hydrogel composites

To confirm the reinforcing effect of the LMA phase in the composite hydrogels, uniaxial tensile tests were performed on PUMA-LMA composite. Typical force-stretch curves of the PUMA composite, neat LMA honeycomb skeleton, and pristine PUMA gel are shown in Fig. 5.5a. The PUMA composite exhibited much higher stiffness (~25 kNm^{-1}) than the pristine gel (~4 kNm^{-1}), similar to that of the neat LMA skeleton (~27 kNm^{-1}) (Fig. 5.5b). However, the maximum stretch of the composite (~ 480%) was comparable to that of the pristine gel (~ 550%). This is due to the unique fracture process of the composite, which results in a highly stretchable, yet stiff composite. As shown in the macrographs in Fig. 5.5a, initially, the stress was concentrated in the stiff LMA skeleton, until it fractured. Then, the stress was transferred to the soft hydrogel matrix that stretched until it reached a force that was comparable to the fracture force of the LMA skeleton (~16 N). After that, other regions of the LMA skeleton ruptured. Locally, the deformed regions of the gel were highly stretched, which enables high stress. However, rather than fracturing globally, the force caused the LMA skeleton to fracture, and this process continued many times. The composite hydrogel exhibits stretch values close to that of the pristine gel, but with force values near the fracture force of the LMA skeleton. This mechanical response mimics that of double network gels, where the LMA skeleton acts as the first network, breaking to dissipate energy, and the PUMA gel acts as the second network, stretching to maintain global integrity. This phenomenon has also recently been reported in a model fabric mesh-VHB tape composite system[30]. As a result of the high stiffness and extensibility of the composite, the composite toughness was much higher than either neat component (Fig. 5.5c), representing a synergistic increase in mechanical properties.

It should be noted that the matrix component must possess a higher strength than the LMA skeleton to induce the multiple fracture process. This can be clearly seen in the behavior of the PAAm composite, in which the pristine PAAm gel is much weaker than the neat LMA skeleton (Fig. 5.6a). The composite also exhibited much higher stiffness (~37 kNm^{-1}) than the pristine gel (15 Nm^{-1}), similar to that of the neat LMA skeleton (~44 kNm^{-1}) (Fig. 5.6b). However, due to the much lower fracture force of the PAAm hydrogel matrix (0.5 N) than the LMA skeleton (22 N), the matrix was unable to sustain the high force and fractured in one step, rather than the multiple fracture process seen in the PUMA hydrogel system. Thus, the toughness of the PAAm composite was as low as the neat LMA skeleton (Fig. 5.6c).

Utilizing a tough hydrogel, such as PUMA, as the matrix material is important towards developing extremely tough composite hydrogels, because it is capable of sustaining high load prior to fracture. The high strength of PUMA is due to the formation of hydrogen bonds between the polymer chains, as indicated by the deswelling of the PUMA hydrogel in water. Such hydrogen bonds serve as reversible sacrificial bonds to dissipate energy and causes the toughening effect of the PUMA hydrogel based on the DN principle[31]. Accordingly, the PUMA-LMA composite have sacrificial bonds at two length scales: the molecular-scale hydrogen bonds and the macro-scale LMA skeleton.

In this research, only the honeycomb-shaped LMA skeleton was used as a prototype. However, one of the great advantages of macroscopic composite systems is that they are highly customizable, and specialized geometries can be utilized to optimize the design for specific applications[32]. The shape effects and characteristic geometries will subsequently be reported in next chapter.

5.3.3 Tunable mechanical properties and functions via thermal activation

The mechanical properties of LMA are dramatically different below and above the melting point due to the solid-liquid phase transition[27-29]. Similarly, by combining LMA and hydrogels into macro-scale composites, we used temperature as an active stimulus to tune the mechanical properties of the composites. To verify the mechanical response at low (25°C) and high (80°C) temperatures, bending modulus and Young's modulus were measured by three-point bending tests and uniaxial tensile tests in cold (25°C) and hot (80°C) water, respectively (Fig. 5.7b). At low temperature, the bending modulus and Young's modulus of the PUMA composite are approximately 30 and 100 times higher than those at high temperature, respectively. Also the bending modulus and Young's modulus of the PAAm composite at low temperature are approximately 230 and 1000 times higher than those of the PAAm composite at high temperature. The difference between bending modulus and Young's modulus is due to the anisotropy of the geometry of the composite. Since the LMA skeleton is located nominally in the middle of the composite, during bending tests it experiences smaller strain than the surrounding gel, biasing the composite modulus towards that of the gel. Meanwhile, in the uniaxial tensile test, the strain is uniform across the cross-section of the sample, resulting in higher stiffness.

Utilizing the modulus difference between high and low temperature, the PUMA composite gel is capable of demonstrating repeatable shape memory (Fig. 5.7a). The composite gel could retain its shape due to the high stiffness of the internal LMA skeleton at room temperature (25°C) (Fig.5.7a-i). However, after immersing the composite into hot water (80°C), the composite became flexible and returned to its as-prepared shape. The sample then became freely deformable (Fig.5.7a-ii), and when the composite was cooled while keeping a desired shape, the composite retained the new shape (Fig.5.7a-iii). When the shape-fixed composite was reheated above the melting point of the LMA, spontaneously, it returned to the initial shape (Fig. 5.7a-iv), due to the elastic restoring forces of the gel matrix. The ability to quickly change stiffness makes these hydrogel composites good shape memory materials, and opens up the possibility for use as variable stiffness actuators[28].

Beyond possessing enhanced stiffness, toughness, and well-defined shape control, the composite hydrogels introduced here, possessing a macroscopic double network architecture, are capable of rigid first network healing, which is a function that conventional double network hydrogels do not possess. When the composite samples whose internal LMA skeleton ruptured were immersed in hot water (80 °C), the fragments of the internal LMA skeleton melted and re-formed (Fig. 5.7c-i,ii) . After cooling the samples (25°C), LMA composites completely healed to the original state (Fig. 5.7c-iii,iv). To quantitatively evaluate the thermal healing efficiency, loading-unloading cyclic tests were performed with various cycle strains (0.5-2.5) and the mechanical response was measured. Typical load-unloading curves (cycle strain: 1.0) of the PUMA composite and the PUMA pristine gel are shown in Fig. 5.7d. There were no significant differences between the initial test curves and the thermally healed test curves for both the pristine PUMA gel and the composite, showing that the healing efficiency, defined as the ratio between the hysteresis areas under the loading-unloading curve of the initial test and thermally healed test, reached ~98 %. Within this strain range, the dissipated energy (defined as the hysteresis area) of the composite gel (~ 0.95 MJ m^{-3}) was much higher than that of the pristine gel (~ 0.24 MJ m^{-3}) even after thermal healing. Similarly, the same analysis was performed with various cycle strains to investigate the thermal healing behavior (Fig. 5.7e). Below a strain of 1.5, the healing efficiency of the composite was equivalent to the pristine gel. Above a strain of 2.0, the healing efficiency of the composite decreased compared to the pristine gel, because the gel matrix became damaged around the internal LMA skeleton during testing, and the liquid LMA could no longer reform sufficiently (Fig. 5.7f,g). In particular, above a cycle strain of 2.5, the gel surrounding the LMA skeleton ruptured and thermal healing could not be performed due to leakage of the LMA. However, the dissipated energies in the healed composite above the cycle strain of 2.0 were still higher than that of the pristine gels. Therefore, this general method results in very tough hydrogel composites, with significant healing abilities. The healing efficiency likely can be improved through careful engineering of the reinforcing skeleton[29] (changing geometry, matrix, and so on).

5.3.4 Unique applications of LMA-based macro-scale hydrogel composites

Owing to the combination of different kinds of functional materials, the composite gels exhibit various unique characteristics in addition to the improved mechanical properties. For example, given the high electrical conductivity (2.4×10^6 Sm^{-1}) of LMA, similar to typical metals[33], the LMA skeleton can serve as an electrode inside the hydrogel matrix to induce local electro-chemical reactions as shown in Fig. 5.8a. Fig. 5.8b demonstrates an example of electrolysis in a PAAm composite swollen in aqueous solution containing sodium chloride and phenolphthalein. After voltage was applied, hydroxide ions were generated around the LMA skeleton that was connected to the negative electrode of the power supply, which caused a chemical reaction with the phenolphthalein. Subsequently, a color-change was observed[34]. In addition to this, electro-polymerization can be performed at the interface between the LMA electrode and hydrogel matrix. As shown in Fig. 5.8c, when the hydrogel matrix contained sodium chloride and pyrrole, black polypyrrole was electro-chemically polymerized around the LMA skeleton that was connected to the positive electrode of the power supply. This electro-chemical reaction could be used to fabricate composites that have increased interfacial strength[35, 36].

In a contrasting approach, the LMA can be used as template to develop hydrogels with a programmed channel structure. As shown in Fig. 5.9a, by taking advantage of the solid-liquid phase transition of LMA, the internal LMA skeleton of the composite could be easily removed by air pressure in hot water, resulting in hydrogel fluidic devices. Such kind of hydrogel fluidic devices could be used for size excluded separation controlled by the mesh size of the gel matrix. For example, small dye molecules (~16 nm) could diffuse into the bulk of the hydrogel matrix with (Fig. 5.9a-ii), while the large colloidal particles (~100 nm) could not (Fig. 5.9a-iii). Given the high wettability of hydrogels (Fig. 5.9b-i), the hydrogel-based fluidic device showed strong capillary action to aqueous solutions. To demonstrate well-controlled capillary action of the hydrogel fluidic device, a PAAm hydrogel with straight line channels of various sizes was fabricated by utilizing LMA as a template (Fig.5b-ii). Subsequently, the hydrogel was immersed in aqueous solution containing dye and the liquid rose vertically due to the capillary force in the channels of the hydrogels (Fig.5b-iii). The height of the liquid columns, h, was found to be inversely proportional to the size of the channels, a, agreeing with the theoretical relationship (Fig.5b-iv). This result shows that the capillary action is precisely controlled by geometry of the channels. Possessing the ability to rapid transport fluid over a long distance by capillary force, these hydrogel fluidic devices can serve as fast and efficient molecular filters or chemical reactors [37, 38].

5.4 Conclusions

In conclusion, we demonstrate that macro-scale hydrogel composites based on low-melting point alloys represent a universal strategy to develop composites free of swelling-induced physical deformation. When water-swollen composites are immersed in hot water (above the melting point of the LMA), the stress from matrix swelling was spontaneously removed due to the transformation of the LMA skeleton from the load-bearable solid state to the free-deformable liquid state. The resulting composites possess high stiffness similar to the LMA phase. In particular, when the strength of hydrogel matrix is comparable to the internal LMA skeleton, the composites exhibit a synergistic increase in toughness, greater than either neat component, based on the macroscopic double network effect. Additionally, by taking advantage of the solid-liquid phase transition of the LMA, dramatic stiffness changes can be triggered by a thermal stimulus, which simultaneously enables quick and high efficient thermal healing properties. Furthermore, the combination of functional materials makes these materials uniquely designed for versatile applications. For example, integration of a customized LMA electrode in the hydrogel matrix and using the hydrogel as a molecular “cage” enables us to develop devices for diverse fields such as bioelectronics, soft robotics and so on. The channel templating method not only allows us to develop materials for filtering device similar to an artificial kidney, but also provides a promising pathway to create macro-scale composite hydrogels containing smart fluids such as magnetic, liquid crystal, and electrorheological fluids. Utilizing low-melting alloys in macroscopic composite hydrogels should enable the use of hydrogels in a wide range of field and applications that were previously incompatible for hydrogel materials.

5.5 References

1. U. G. K. Wegst, H. Bai, E. Saiz, A. P. Tomsia & R. O. Ritchie, *Nat. Mater.* **14,** 23-36 (2014).
2. X. Sun, H. Sun, H. Li & H. Peng, *Adv. Mater.* **25,** 5153-5176 (2013).
3. B. C-K. Tee, C. Wang, R. Allen, & Z. Bao, *Nat. Nanotechnol.* **7,** 825-832 (2012).

4. S. Hong, D. Sycks, H. F. Chan, S. Lin, G. P. Lopez, F. Guilak, K. W. Leong, X. Zhao, *Adv. Mater.* **27,** 4035-4040 (2015).
5. P. Li, Y. F. Poon, W. Li, H.-Y. Zhu, S. H. Yeap, Y. Cao, X. Qi, C. Zhou, M. Lamrani, R. W. Beuerman, E.-T. Kang, Y. Mu, C. M. Li, M. W. Chang, S. S. J. Leong, & M. B. Chan-Park, *Nat. Mater.,* **10,** 149-156 (2011).
6. M. J. Zohuriaan-Mehr, & K. Kabiri, **17,** 451-470 (2008).
7. Q. Wang, J. L. Mynar, M. Yoshida, E. Lee, M. Lee, K. Okuro, K. Kinbara & T. Aida, *Nature,* **463,** 339-343 (2010).
8. K. Haraguch, & T. Takehisa, *Adv. Mater.* **14,** 1121-1124 (2002).
9. J.-Y. Sun, X. Zhao, W. R. K. Illeperuma, O. Chaudhuri, K. H. Oh, D. J. Mooney, J. J. Vlassak & Z. Suo, *Nature* **489,** 133-136 (2012).
10. N. Hirota, Y. Kumaki, T. Narita, J. P. Gong & Y. Osada, *J. Phys. Chem. B* **104,** 9898-9903 (2000).
11. A. N. Peppas, J. Z. Hilt, A. Khademhosseini, & R. Langer, *Adv. Mater.* **18,** 1345-1360 (2006).
12. I. Banerjee, R. C. Pangule, & R. S. Kane, *Adv. Mater.* **23,** 690-718 (2011).
13. J. P. Gong, T. Kurokawa, T. Narita, G. Kagata, Y. Odada, G. Nishimura & M. Kinjo, *J. A,. Chem. Soc.* **123,** 5582-5583 (2001).
14. J. Franklin, & A. Y. Wang, *Chem. Mater.* **14,** 4487-4489 (2002).
15. H. Yuk, S. Lin, C. Ma, M. Takaffoli, N. X. Fang & X. Zhao, *Nat. Commun.* **8,** 14230 (2017).
16. A. B. Imran, K. Esaki, H. Gotoh, T. Seki, K. Ito, Y. Sakai & Y. Takeoka, *Nat. Commun.* **5,** 5124 (2014).
17. D. J. Beebe, J, S. Moore, J. M. Bauer, Q. Yu, R. H. Liu, C. Devadoss & B.-H. Jo, *Nature.* **404,** 588-590 (2000).
18. T. L. Sun, T. Kurokawa, S. Kuroda, A. B. Ihsan, T. Akasaki, K. Sato, Md. A. Haque, T. Nakajima & J. P. Gong, *Nat. Mater.* **12,** 932-937 (2013).
19. T. Tanaka, S.-T. Sun, Y. Hirokawa, S. Katayama, J. Kucera, Y. Hirose & T. Amiya, *Nature* **325,** 796-798 (1987).

20. Zhang, X. C. L. Pint, M. H. Lee, B. E. Schubert, A. Jamshidi, K. Takei, H. Ko, A. Gillies, R. Bardhan, J. J. Urban, M. Wu, R. Fearing & Ali, Javey, *Nano Letters* **11,** 3239-3244 (2011).
21. M. Y. Kim, B. Jung & J.-H. Park, *Biomaterials* **33,** 668-678 (2012).
22. D. R. King, T. L. Sun, Y. Huang, T. Kurokkawa, T. Nonoyama, A. J. Crosby & J. P, Gong, *Mater. Horiz.* **2,** 584-591 (2015).
23. Y. Huang, D. R. King, T. L. Sun, T. Nonoyama, T. Kurokawa, T. Nakajima & J. P. Gong, *Adv. Funct. Mater.* **27,** 1605250 (2017).
24. W. R. K. Illeperuma, J.-Y. Sun, Z. Suo & J. J. Vlassak, *Extreme Mechanics Letters,* **1,** 90-96 (2014).
25. K. Tonsomboon, A. L. Butcher & M. L. Oyen, *Materials Science & Engineering C.* **72,** 220-227 (2017).
26. H. Yuk, T. Zhang, G. A. Parada, X. Liu & X. Zhao, *Nature Commun.* **7,** 12028 (2016).
27. E. B. Schubert & D. Floreano, *RSC Advances* **3,** 24671 (2013).
28. I. M. V. Meerbeekm, B. C. M. Murray, J. W. Kim, S. S. Robinson, P. X. Zou, M. N. Silbertein & R. F. Shepherd, *Adv. Mater.* **28,** 2801-2806 (2016).
29. A. Tonazzini, S. Mintchev, B. Schubert, B. Mazzolai, J. Shintake & D. Floreano, *Adv. Mater.* **28,** 10142-10148 (2016).
30. X. Feng, Z. Ma, J. V. MacArthur, C. Giuffre, A. Bastawros & W. Hong, *Soft Matter* **12,** 8999-9006 (2016).
31. J. P. Gong, *Soft Matter* **6,** 2583-2590 (2010).
32. O. Bas, D. D7Angella, J. G. Baldwin, N. J. Castro, F. M. Wunner, N. T. Saidy, S. Kollmannsberger, A. Reali, E. Rank, E. M. De-Juan-Pardo & D. W. Hutmacher, *ACS Appl. Mater. Interfaces,* **35,** 29430-29437 (2017).
33. A. Ainla, S. Xu, N. Sanchez, G. D. M. Jeffries, & A. Jesorka, *Lab Chip* **12,** 4605-4609 (2012).
34. J. Tian, T. Arbatan, X. Li, & W. Shen, *Chem. Comm.* **46,** 4734-4736 (2010).
35. M. Sasaki, B. C. Karikkineth, K. Nagamine, H. Kaji, K. Torimitsu & M. Nishizawa, *Adv. Healthc. Mater.* **11,** 1919-1927 (2014).

36. Y. Gao, S. J. Song, S. Li, C. Elowsky, Y. Zhou, S. Ducharme, Y. M. Chen, Q. Zhou & L. Tan, *Nat. Commun.* **7,** 12316 (2016).
37. S. Han, T. Wang, & B. Li, *J. Appl. Poly. Sci.* **134,** 1-10 (2017).
38. R. K. Garg, R. C. Rennert, D. Duscher, M. Sorkin, R. Kosaraju, L. J. Auerbach, J. Lennon, M. T. Chung, L. Paik, J. Nimpf, N. Rajadas, M. T. Longaker & G. C. Gurtner, *Stem Cells Trans. Med.* **3,** 1079-1089 (2014).
39. V. Hagel, T. Haraszti & H. Boehm, *Biointerphases* **8,** 2-9 (2013).
40. G. K. Batchelor, *Cambridge University Press,* ISBN 0-521-66396-2 (1967).
41. G. Vazquez, E. Alvarez & J. M. Navaza, *J. Chem. Eng. Data* **40,** 611-614 (1995).
42. H.-Y. Fang, & J. L. Daniels, *CRC Press,* ISBN 9780-4153-04023 (2006).
43. N. N. Greenwood & A. Earnshaw, *Butterworth-Heinemann,* ISBN 9780-7506-33659 (1997).

5.6 Figures

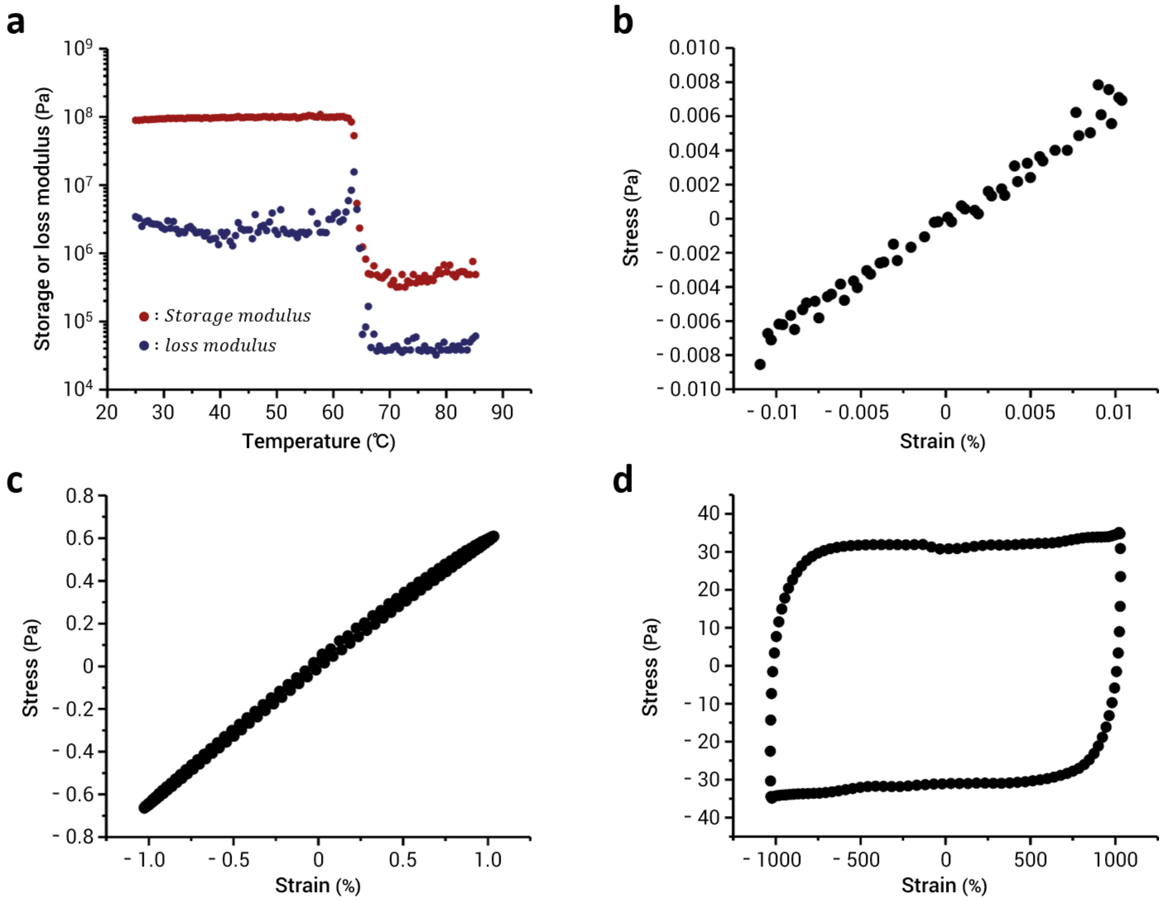

Figure 5.1 | Rheological test of the LMA. (**a**) Temperature dependence of the storage modulus G' and the loss modulus G" of the LMA measured at frequency 1 rad/s and shear strain of 0.01%. (**b,c,d**) Lissajous curves for various strains of (b) 0.01%, (c) 1%, (d) 1000% measured at 80°C and frequency 1 rad/s. At the low strain range (b,c), the Lissajous curves exhibits linear response which indicate that the liquid LMA behaves like an elastic material even above the melting temperature. At high strain range (d), the Lissajous curve shows plastic flow behavior, indicating that the LMA acts as free-deformable liquid.

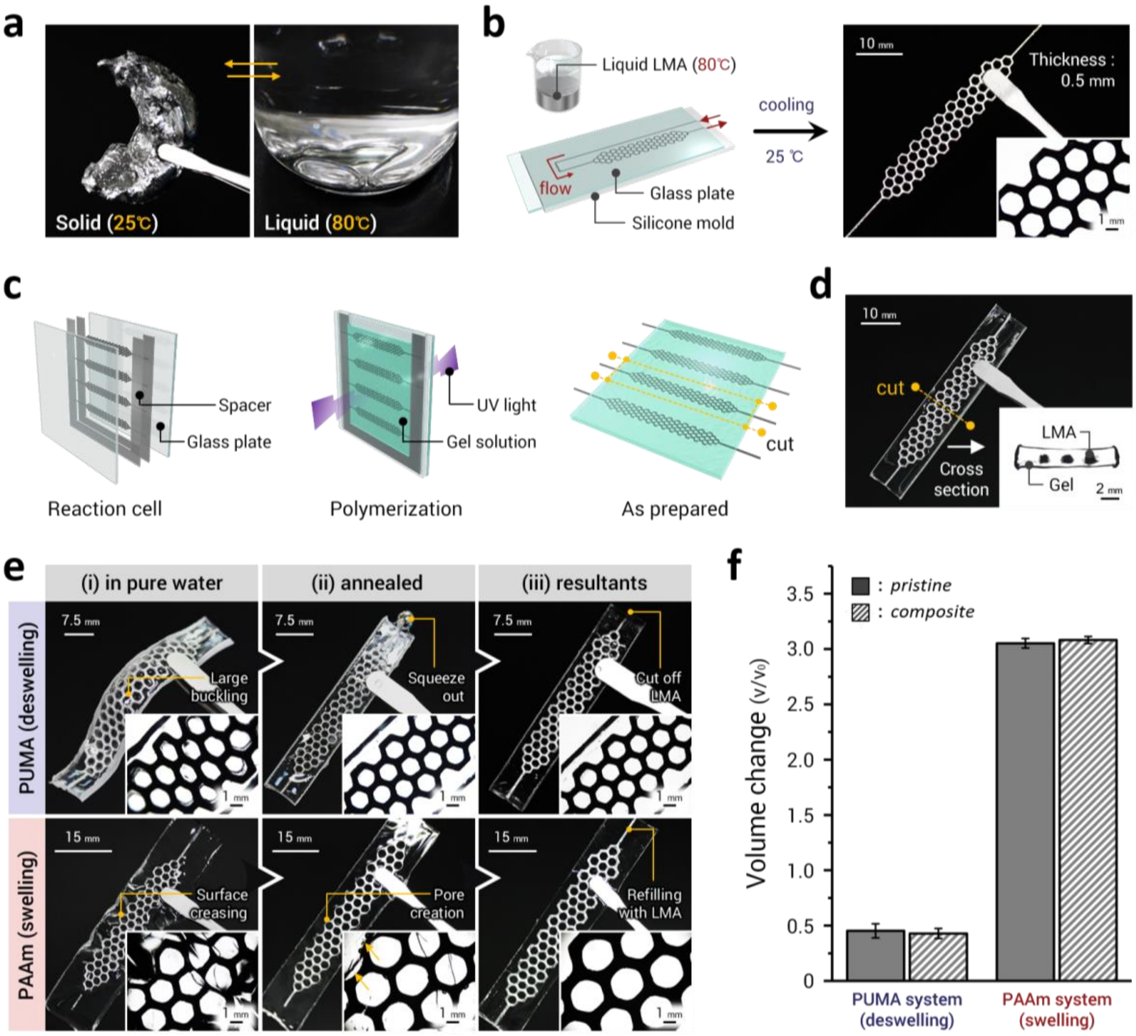

Figure 5.2 | Fabrication of hydrogel-LMA composites without swelling mismatch. (**a**) Solid-liquid phase transition of Low-melting point alloy (LMA); composition of the LMA is 32.5 % Bi, 51% In, 16.5% Sn. (**b**) Schematic illustration of the fabrication process of honeycomb-shaped LMA skeletons from a silicone mold and photograph of the resulting LMA skeleton. The inset image is an optical micrograph of the LMA skeleton observed from the top. (**c**) Schematic illustration of the fabrication process of the composites. (**d**) Photograph of an as-prepared PUMA composite. The inset image is an optical micrograph of the cross-section. Appearance of the as-prepared PAAm composite is similar to the as-prepared PUMA composite. (**e**) Photographs of the composites equilibrated in pure water before (i), after the thermal annealing treatment (ii) and after adjusting the volume of LMA (iii). Due to shrinkage (or swelling) of the PUMA (or PAAm) in water, which induces a large mismatch between the gel and LMA solid skeleton, large buckling (or surface creasing) was observed. After thermal annealing by immersing the samples in 80°C water, the swelling mismatch was spontaneously released due to melting of the LMA. Inset images are optical micrographs observed from top direction. (**f**) Comparison of the volume changes between the pristine gels and composite gels in relative to the as-prepared state. Both deswelling and swelling systems exhibited the same volume changes between the pristine gel and the composite. Each measurement was performed 3-5 times. Error bars represent standard deviation.

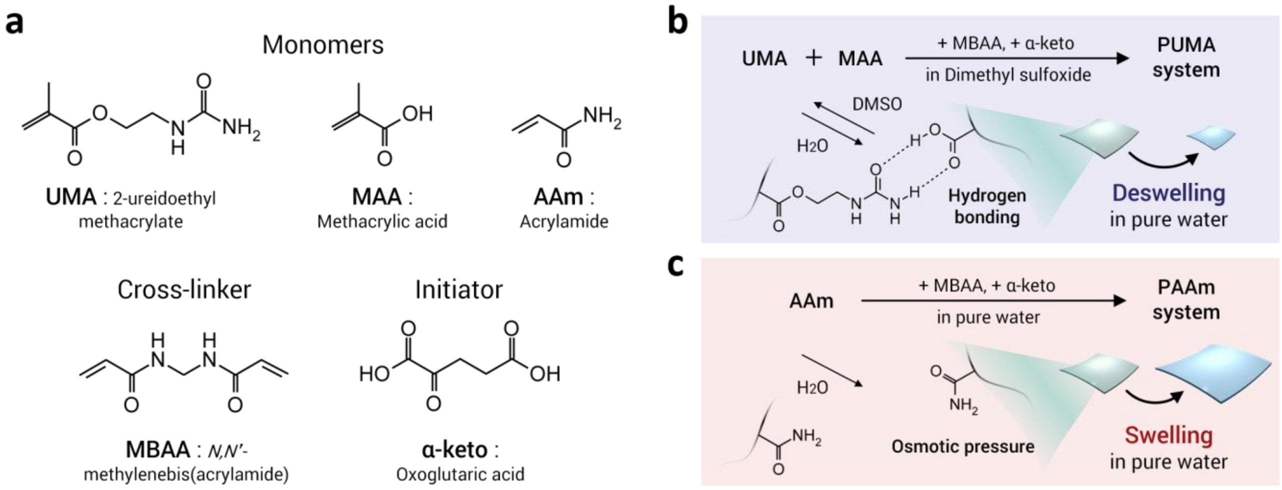

Figure 5.3 | Chemical structures and reaction schemes of deswellable / swellable hydrogels. (**a**) Chemical structures of monomers, cross-linker, and initiator. (**b, c**) Model systems of deswellable (b) and swellable (c) hydrogel matrix. (b) PUMA system exhibits deswelling nature in pure water due to the formation of hydrogen bonds during solvent exchange from dimethyl sulfoxide (DMSO) to pure water. (c) PAAm system exhibits swelling nature in pure water.

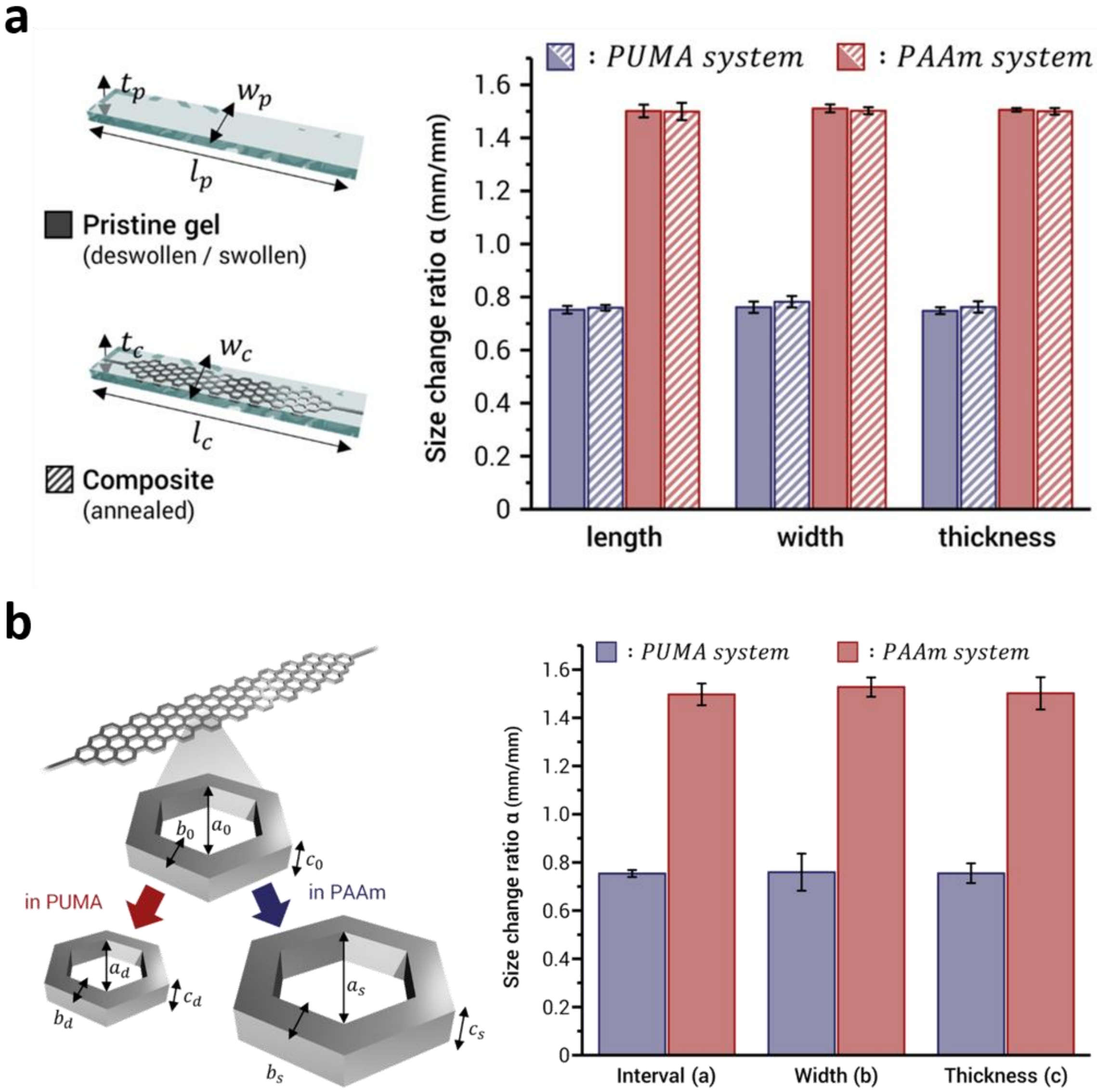

Figure 5.4 | Size changes of pristine gels and composites at swelling equilibrium in relation to their as-prepared states. (**a**) The PUMA system exhibited isotropic shrinkage while the PAAm system exhibited isotropic swelling. Each measurement was performed three times. Error bars represent standard deviation. (**b**) Size changes of the LMA honeycomb in annealed composites in relation to that of the as-prepared state. The PUMA system exhibited isotropic shrinkage while the PAAm system exhibited isotropic swelling. These results well coincide (a), indicating that the local swelling mismatch was also released. Each measurement was performed three times. Error bars represent standard deviation.

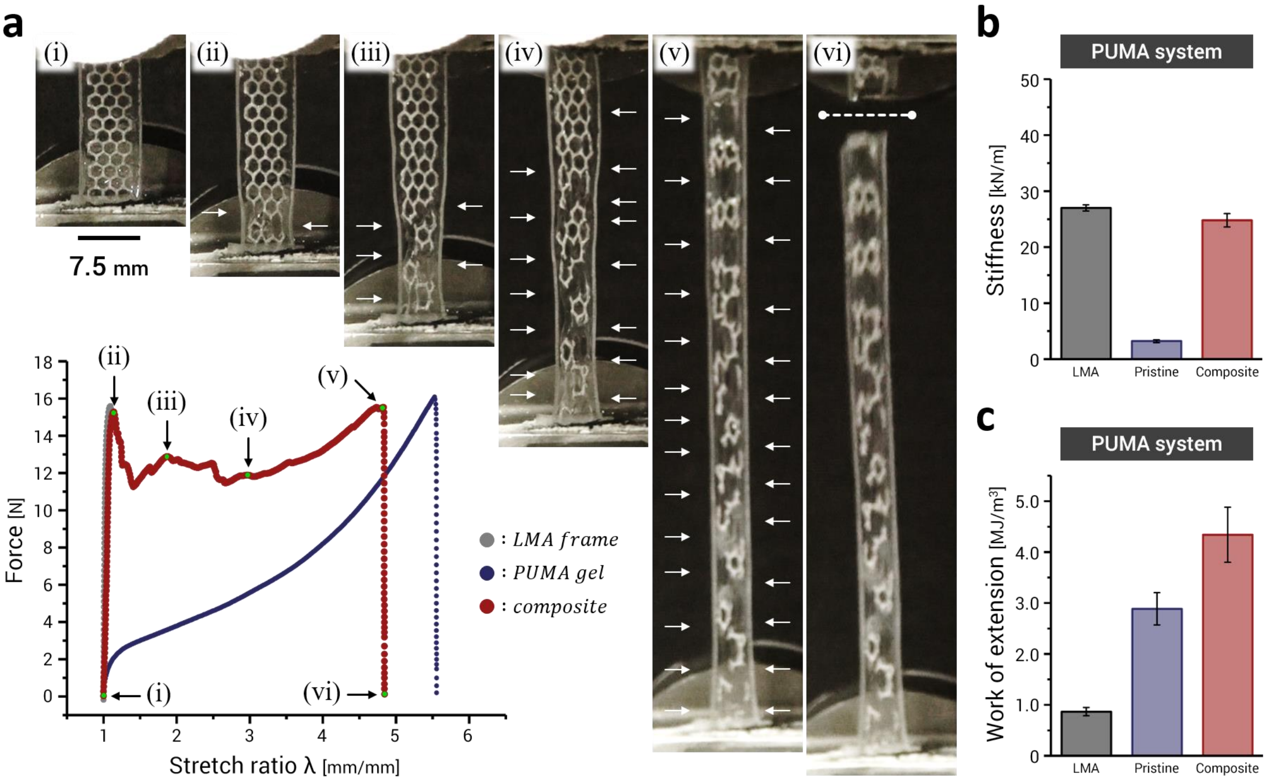

Figure 5.5 | Mechanical properties of PUMA-LMA composites. (**a**) Force-stretch curves of a honeycomb mesh LMA skeleton (grey), a pristine PUMA gel (navy) and their composite (wine). The insets (i)-(vi) represent snapshots of the composite sample at the corresponding stretch shown in the loading curves. Initially, the force of the composite rapidly increased and the LMA skeleton broke at a force comparable to that of the neat LMA skeleton (i-ii). During further stretching of the sample (ii-v), multiple fractures of the LMA skeleton were observed (inset arrows indicate fracture points), while the hydrogel matrix maintains global integrity. As a result, bulk fracture did not occur. Finally, the hydrogel matrix ruptured at the position shown by the dashed line (vi). (**b**) Stiffness of each component and the composite in the respective system. (**c**) Work of extension (area below the stress-strain curve) of each component and composite in the respective system. Each mechanical test was performed 3-5 times. Error bars represent standard deviation.

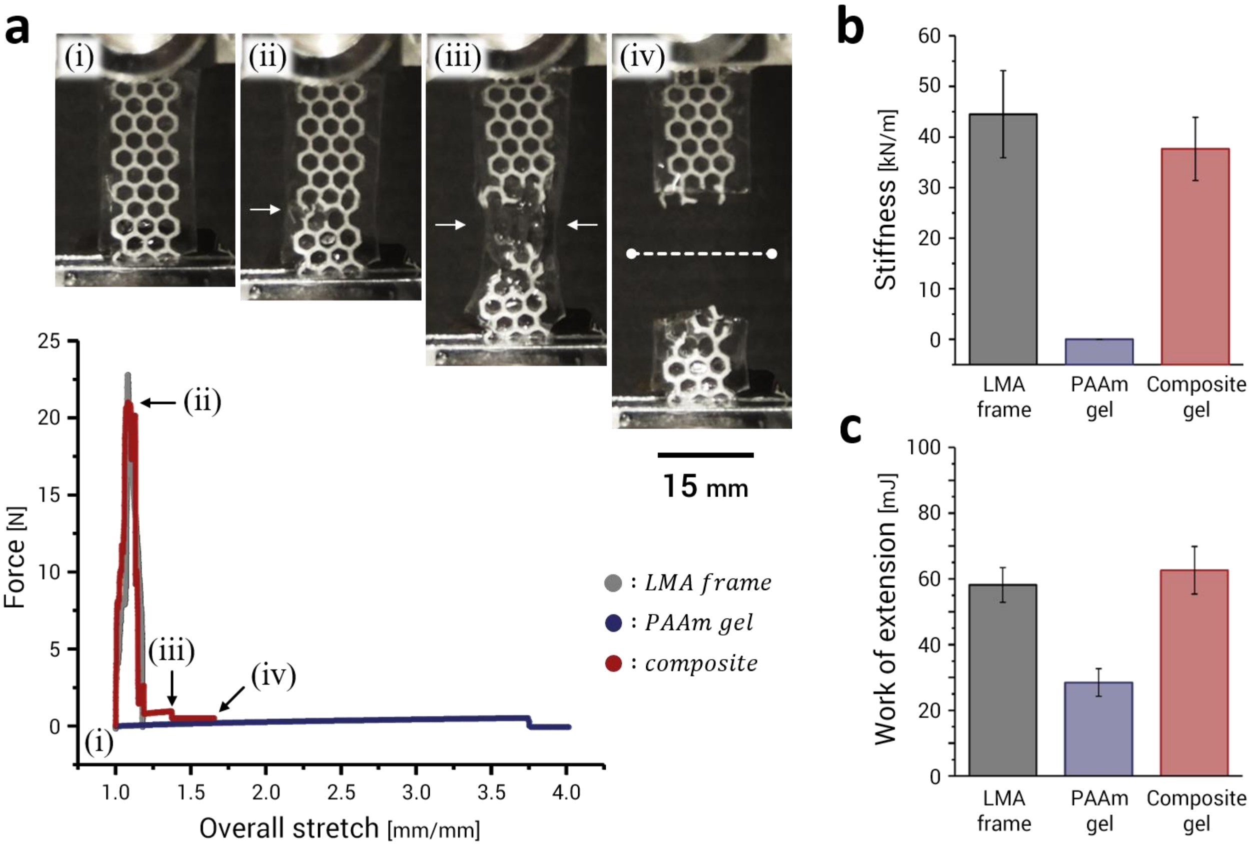

Figure 5.6 | Mechanical properties of PAAm-LMA composites. (**a**) Force-stretch curves of a honeycomb mesh LMA skeleton (grey), a pristine PAAm gel (navy) and their composite (wine). The insets (i)-(iv) represent the snapshots of the composite sample corresponding to the specific points shown in the loading curves. Initially, the force of the composite rapidly increased and the LMA frame broke at a force comparable to that of the neat LMA frame (i-ii). After fracture of the LMA frame, the hydrogel matrix was stretched (ii-iii). Finally, the hydrogel matrix ruptures at the position shown by the dashed line (iii-iv). (**b**) Stiffness of each component and the composite in the respective system. (**c**) Work of extension (area below the stress-strain curve) of each component and composite in the respective system. Each mechanical test was performed 3-5 times. Error bars represent standard deviation.

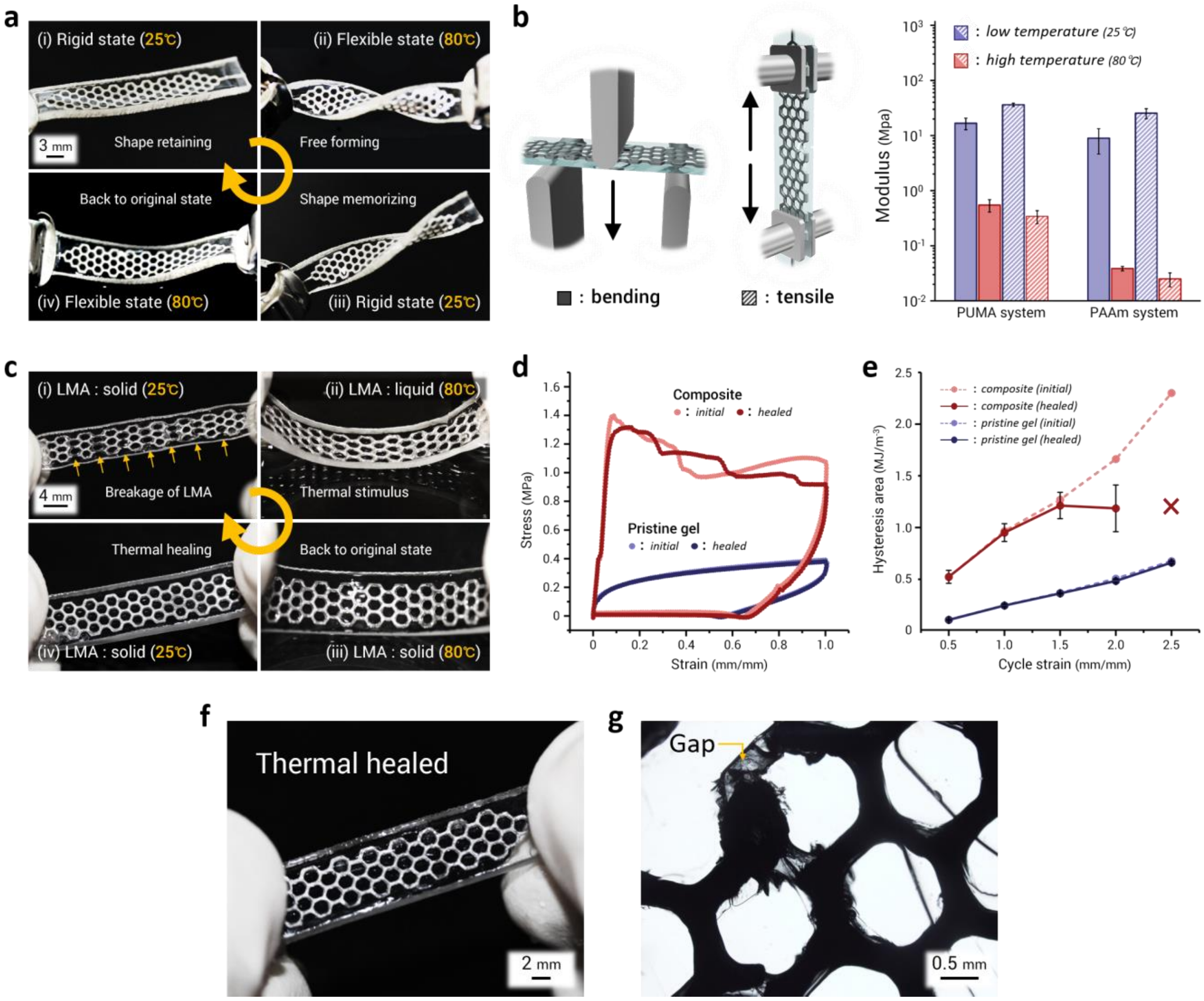

Figure 5.7 | Thermal response and thermal healing of PUMA-LMA composites. (**a**) Demonstration of shape memory based on the solid-liquid phase transition of the LMA skeleton. (**b**) Bending and tensile moduli of the composite at low (25°C) and high (80°C) temperature. (**c**) Demonstration of thermal healing ability at a stretch ratio of approximately 2.5. Inset arrows in (i) represent the broken points of internal LMA skeleton. (**d**) cyclic test curves of composite and pristine PUMA gels. (**e**) Mechanical hysteresis loss during loading and unloading testing at various strains (0.5-2.5). The data for the healed composite at a strain of 2.5 was not available due to breakage of the sample during the first cycle. (**f**) A photograph of the thermally healed sample after loading / unloading test at a strain of 2.0. (**g**) A micrograph of the thermal healed sample. Due to the damage of the matrix, especially around the LMA frame, liquid LMA flowed into the damaged matrix, which caused permanent damage of the composite. Each measurement was performed 3-5 times. Error bars represent standard deviation, and are smaller than the marker unless explicitly shown.

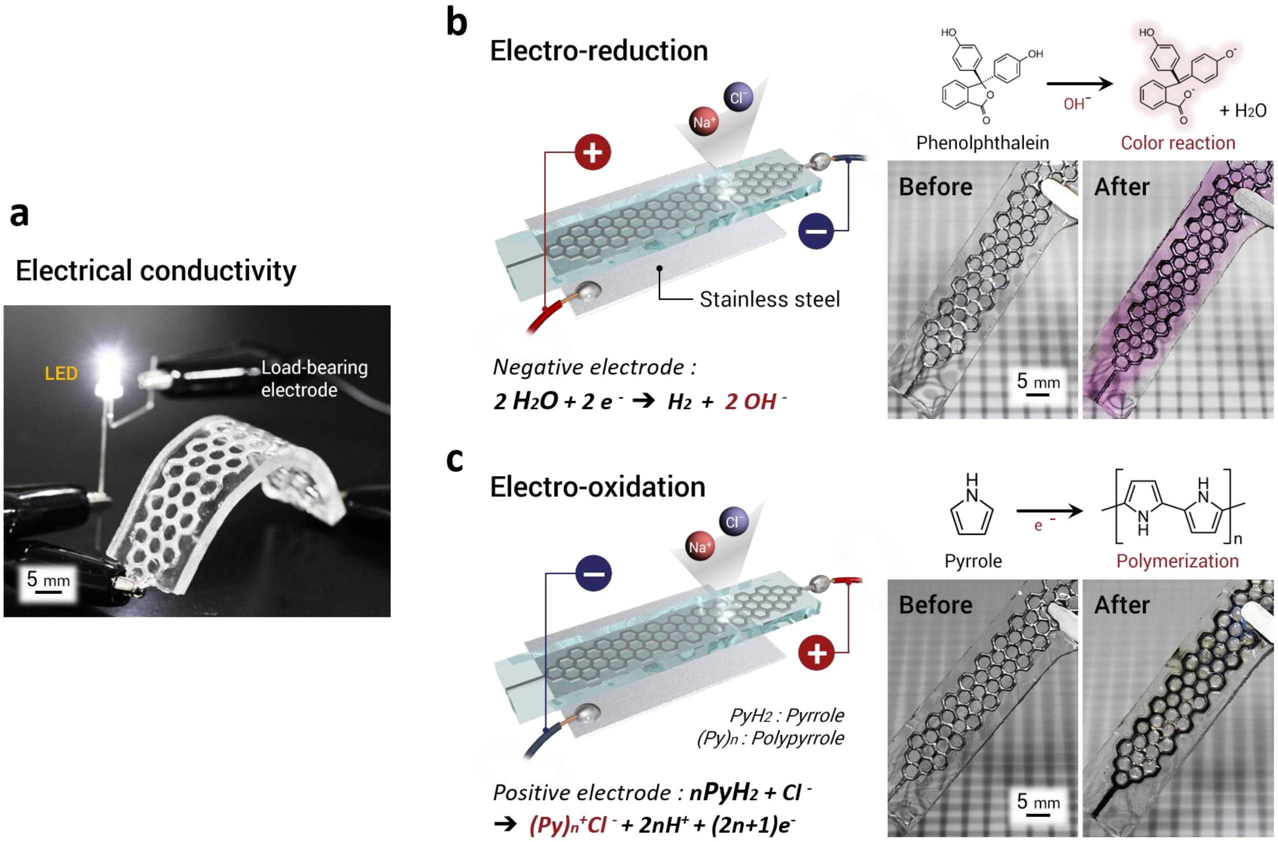

Figure 5.8 | Electrochemical reactions in PAAm-LMA composites. (**a**) Electrical conductivity of LMA composite hydrogels. Both ends of the LMA frame were connected to a power supply unit (3V) and LED light in series. (**b**) Demonstration of electro-reduction in the hydrogel matrix for the composite swollen with NaCl aqueous solution (0.15 M). By connecting the LMA skeleton to the negative electrode and the gel to the positive electrode of a 3V power supply, a reduction reaction was induced and hydroxide ions were generated around the LMA skeleton. When the hydrogel matrix contained phenolphthalein, a color response was observed after electrolysis due to the reaction between the phenolphthalein and the hydroxide ions. (**c**) Demonstration of electro-oxidation in the hydrogel matrix for the composite swollen with NaCl aqueous solution (0.15 M). By connecting the LMA skeleton to the positive electrode and the gel to the negative electrode of a 3V power supply, an oxidation reaction was induced. When the hydrogel matrix contained pyrrole monomers, black polypyrrole can be observed around the honeycomb skeleton of LMA after electrolysis due to the oxidative electro-polymerization.

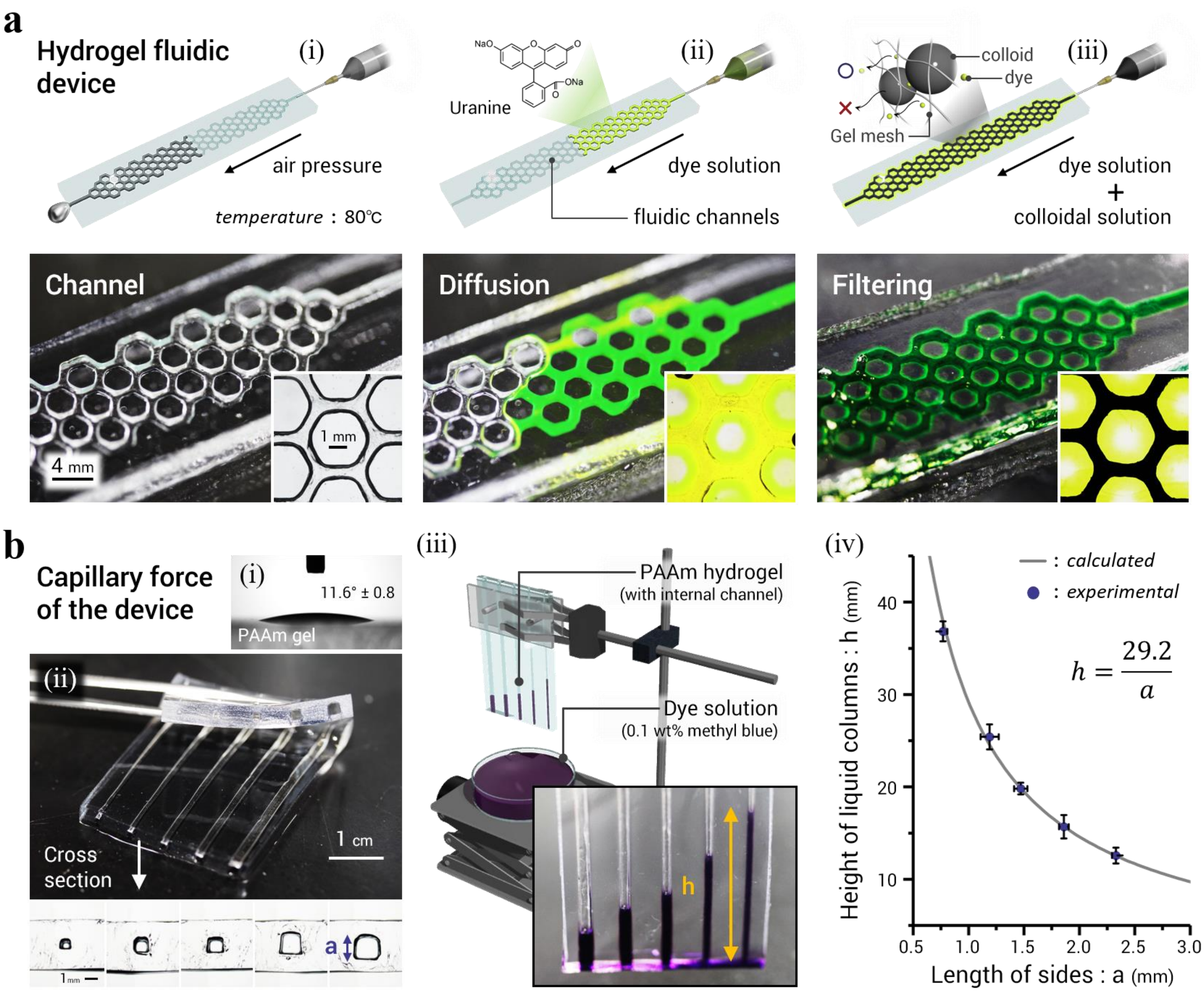

Figure 5.9 | Hydrogel fluidic devices using LMA as template. (**a**) Fabrication of a PAAm hydrogel fluidic device utilizing the LMA skeleton as a channel template; (i) photograph and optical micrograph (inset) of the channel structure, (ii) demonstration of hydrogel fluidic channels by diffusion of green dye molecules (Uranine) into the hydrogel matrix (inset picture), (iii) hydrogel filtration of black colloidal particles (Indian ink) from a mixture with green dye (Uranine) when passed through the hydrogel channels. The upper row are illustrations to show the channel fabrication (i), dye diffusion (ii), and filtration (iii). (**b**) Investigation of a capillary action of the PAAm hydrogel fluidic channels; (i) whole view (top) and cross sections (bottom) of hydrogel channels with various width, *a*, (ii) demonstration of capillary action using purple dye solution (0.1 % methyl blue), (iii) theoretical and experimental results of the relationships between the liquid columns height, *h*, and the length of the channel side, *a*. The theoretical inverse relationship between *h* (mm) and *a* (mm) is the result of the energy balance between the wetting of water on the gel surface and the potential energy of the water column. The numerical factor 29.2 (mm^2) is estimated using the surface tension of water, the contact angle of water to the PAAm gel, the density of water, and the acceleration of gravity. Each measurement was performed for three times. Error bars represent standard deviation.

CHAPTER 6

Tunable Mechanical Properties of Macro-scale Soft Composites via Geometrical design

6.1 Introduction

Over the past decade, double-network (DN) gels have drawn significant attention because of its extremely high Young's modulus (10^5-10^6 Pa) and high toughness (4500 J/m^2) despite of containing up to 90% of water[1-3]. This extraordinary mechanical properties has been attributed to the unique structure of DN gel, consisting of a relatively hard/brittle network (the 1st network) and a soft/ductile network (the 2nd network)[4]. The combination of two different types of networks provide interesting toughening mechanism called a "sacrificial bond principle": the 1st network is catastrophically broken prior to rupture of the 2nd network and this fragmentation distribute significant energy, resulting high mechanical properties. Many researches have devoted intense efforts to improve and generalize this double network concept widely and one remarkable concept proposed by X. Feng *et al.* recently is a "macro-scale" double network composite[5]. This material, consisting of a hard fabric mesh and soft VHB tape layers, is as stiff as the fabric mesh and as stretchable as the VHB tape. Furthermore, at the certain compositions, the mechanical properties of the composite significantly higher than that of individual components due to the sacrificial bond principle similar to typical DN gel[6]. This development indicate that DN concept can be expanded from "micro" scale to "macro" scale and it open new research fields that is macro-scale DN composite materials.

One outstanding advantage of macro-scale composite systems is various types of reinforcement materials can be utilized. If we can combine hydrogels with materials which have interesting properties, we can create functional, smart materials[7-9]. In chapter 5, we described about the macro-scale DN composite gels based on low-melting point alloys, showing high stiffness, high toughness, and tunable mechanical properties via thermal activation. Beyond the use of functions originated from reinforcement itself, one of the next challenge is utilizing a unique architecture of reinforcing phase to introduce further functions. Recent developments of material processing such as 3D printing, computerized numerical control (CNC) milling device, and laser cutting, enable us to design reinforcement materials with desirable shape[10-12], however, current macro-scale DN composite studies did not pay attention to the geometrical effect of reinforcement architectures.

In nature, we can find intricate yet highly ordered architectures in a bee-hive (honeycomb), soles of gecko, and wing of morpho, which is considered to play an important role for emergence of functions, such as high strength-to-weight ratio, strong and anisotropic adhesion, and beautiful structural color[13-15]. In spired by this, many researchers have devoted intense effort to develop such architectures artificially and utilize them for fabricating useful materials in diverse fields, including honeycomb architectures for construction materials, gecko patterns for smart adhesive tape, and morpho structural color for paints[16-18]. Additionally, specific design can achieve anomalous yet valuable properties that cannot be found in nature and an engineering material having such architectures is called a metamaterial[19-21]. For example, "auxetics" proposed by K. E. Evans *et al.* are architectures that have a negative Poisson's ratio (such a material expands laterally when stretched, in contrast to ordinary materials), which may be useful in applications such as packing materials or robust shock absorbing materials[22]. Therefore, architecture of materials are significant for practical applications, which is one of the smartest approach for creating on-demand multi-functional materials.

Towards obtaining such materials, we combine the two concept, macro-scale DN composite approach and smart architectures approach. In this work, we fabricated a 3D-printable resin reinforcing natural rubber (NR) or polyvinyl alcohol (PVA) as the macro-scale DN composites and investigated the geometrical effect of reinforcing phase architectures in the composites on mechanical properties. For comparison, three types of architectures, honeycomb, square, and auxetic grids, are utilized for reinforcing phase architectures. The mechanical properties are measured by uniaxial tensile and compression testing for 2D-shaped and 3D-shaped geometries, respectively. The resultant DN composites exhibits high stiffness, similar to the resin reinforcing phase and high toughness with multiple internal fracture of reinforcing phase like as sacrificial bonds of the classical DN gel.

Furthermore, the mechanical properties, Young's modulus and yielding stress, are well controlled by the geometry of reinforcing phase. To understand the enhancing mechanism of mechanical properties, we estimated the Poisson's ratio of the components of composites. Interestingly, we found that the large mismatch of Poisson's ratio between soft matrix and hard reinforcing phase play an important role for increase of mechanical properties. This work should shed light on designing functional composite materials with tunable mechanical properties and the toughening mechanism based on the mismatch of Poisson's ratio may derive new insight for creating super-tough materials.

6.2 Experiments

6.2.1 Materials

A latex solution (LA-Latex, Qua Yu Kasei Ltd.) was used for synthesizing a stretchable and tough natural rubber (NR) matrix and used as received without further purification. A polyvinyl alcohol (PVA, Mw = 2000) (Wako Pure Chemical Industries, Ltd.) was used for preparing a soft hydrogel matrix and used as received without further purification. For all experiments, water was deionized and purified with 0.22 µm and 5 µm membrane filter prior to use.

6.2.2 Design of various geometries for reinforcing phase

The specific 2D or 3D models of reinforcing phase (honeycomb, square, and auxetic grid-shape) were generated by CAD design software (Inventor, Autodesk Inc. and Shade 3D, Shade 3D Co., Ltd.). These models were printed with the high resolution (minimum resolution: 15 µm) 3D printer (Agilista-3000, KEYENCE Co.). Polyurethane and acrylic resin composite was used as an ink material.

6.2.3 Fabrication of macro-scale soft composites

For resin-NR composites, the 3D-printed reinforcing phases (with spacer region for fixing nominally in the middle of NR matrix) were placed on the clean glass plate with square-shaped 2 mm thick silicone spacer (Scheme 6.1). The pre-rubber solution (Latex with 20 wt% water, mixed by vacuuming planetary centrifugal mixer (ARV-310, THINKY Co.), 2000 rpm, 30 kPa, and 2min) was poured into the curing cells and dried under air atmosphere at 25 °C for 3 days. After that, the samples were cut into specific dimensions ($l_0 \times w_0 \times t_0$ = 72×12×1.2 mm^3, or 36×14×1.2 mm^3).

For resin-PVA composites, the 3D-printed reinforcing phases (with spacer region for fixing nominally in the middle of PVA matrix) were placed on the clean glass plate with square-shaped 20 mm thick silicone spacer (Scheme 6.2). The pre-gel solution (10 wt% PVA, 67.5 wt% DMSO, and 22.5 wt% water, mixed at 60℃) was poured into the curing cells and cooled under air atmosphere at -20 ℃ for 24 hours. After that, the samples were cut into specific dimensions ($l_0 \times w_0 \times t_0$ = 22×22×20 mm^3) and immersed in water for 3days to exchange solvent from DMSO to water.

6.2.4 Mechanical testing

Uniaxial tensile tests were performed on 3D-printable resin reinforced NR composites, pristine NR, and the neat resin skeletons using a tensile-compressive tester (Instron 5965 type universal testing system). The composite and pristine NR were prepared with the following dimensions, the gauge length 32 (or 14) mm and the inner width 12 (or 7) mm. Neat resin skeletons (same dimensions as the resin skeleton in the composites, thickness is 0.3 (0.5) mm) were prepared. All the samples were stretched along the length direction of the samples at an extension rate of 80 mm/min. Tensile stretch ratio, λ, is defined as l/l_0, where l_0 and l are the length of the composites before and during elongation, respectively.

Uniaxial compression tests were performed on 3D-printable resin reinforced PVA composites, pristine PVA, and the neat resin skeletons using a tensile-compressive tester (Tensilon RTC-1310A, Orientec Co.). The composite and pristine gels were prepared with the following dimensions, 22×22×20 mm; 20 mm was the gauge length (thickness). Specific size of resin skeletons (same dimensions as the resin skeleton in the composites) were prepared. All the samples were compressed along the thickness direction of the samples at a compression rate of 2 mm/min. Compression ratio, λ, is defined as t/t_0, where t_0 and t are the length (thickness) of the composites before and during compression, respectively.

6.2.5 Polarized optical microscope (POM) observation

The deformation ratio of soft matrix in 3D-printable resin reinforced NR was determined by the intensity of birefringence of the NR in the as-prepared state and the stretching state that were observed under a polarizing optical microscope (POM) (Nikon, Eclipse, LV100POL) in the crossed polarization modes, with and without the tint plate, at room temperature. The composites that have three types of reinforcement geometry (honeycomb, square, and auxetic grid) were prepared and observed. Samples were placed on glass slides and observed from the top (Fig. 6.6c,d). All the samples of NR matrix exhibited a first order white-gray birefringence color and highly deformed part showed pink birefringence color.

6.3 Results & discussion

6.3.1 Creation of macro-scale soft composites based on double network architectures

Required network properties for creating typical double network (DN) materials; hard/brittle properties and soft/ductile properties are necessary for 1st network and 2nd network, respectively. Traditionally, typical DN gels have a first network consisting of a polyelectrolyte, such as PAMPS, and a second network consisting of a neutral material such as polyacrylamide. To expand the DN concept from micro-scale to macro-scale, we utilized a hard, 3D-printable resin grid with specific geometries for 1st network and a soft, stretchable natural rubber matrix for 2nd network to prepare a macro-scale double network (DN) composite. As model systems to produce such composite, firstly we prepared simple lattice-grid shape for reinforcing phase (Fig. 6.1). The composite has a heterogeneous architecture that is macro-scale (mm scale) hard grid phase and soft matrix phase. To confirm the reinforcing effect based on the aforementioned sacrificial bond principle, uniaxial tensile tests were performed on the macro-scale composite. Typical force-displacement curves of the composite, pristine natural rubber (NR), and neat 3D-printable resin grid are shown in Fig. 6.2. The composite exhibited much higher stiffness than the pristine NR, similar to that of the neat resin grid. However, the extensibility of the composite was comparable to that of the pristine NR. This is due to the unique fracture process of the composite, which results in a highly stretchable, yet stiff composite. As shown in the macrographs in Fig. 6.2, initially, the stress was concentrated in the stiff resin grid, until it fractured (Fig.6.3a). Then, the stress was transferred to the soft NR matrix that stretched until it reached a force that was comparable to the fracture force of the resin grid (Fig. 6.3b,c). After that, other regions of the resin grid ruptured (Fig. 6.3d). Locally, the deformed regions of the NR were highly stretched, which enables strain hardening, resulting in high stress. However, rather than fracturing globally, the force caused the resin grid to fracture, and this process continued over and over (Fig.6.3e). The composite exhibits stretch values close to that of the pristine NR, but with force values near the fracture force of the resin grid. This mechanical response mimics that of double network gels, where the resin grid acts as the first network, breaking to dissipate energy, and the NR matrix acts as the second network, stretching to maintain global integrity. This phenomenon has also recently been reported in a model fabric mesh-VHB tape composite system and in a model metal based mesh-tough hydrogel composite system (described in the chapter 5), respectively[5]. Therefore, it is considered that the DN concept is universal methods for designing tough materials not only microscopically but also macroscopically based on the sacrificial bond principle.

6.3.2 2D geometrical effect of reinforcement on mechanical properties (tensile)

One of the most important advantage of the macro-scale DN composites is its high selectivity of reinforcing phase including material and geometry. The former is already demonstrated in chapter 5 that is macro-scale DN composite based on low-melting point alloy (LMA) with multi-functionalities. In this section, we focus on the latter that is geometrical effect of reinforcing phase on mechanical properties of macro-scale DN composites and will introduce a new enhancing approach for mechanical properties based on “Poisson’s effect”[23].

Poisson’s ratio is a measure of the Poisson effect, the phenomenon in which a material tends to expand in directions perpendicular to the direction of compression. Conversely, if the material is stretched, it generally rends to contract in the directions transverse to the direction of stretching as shown in Fig. 6.4a. By using the transverse contraction strain (ε_x) and longitudinal extension strain (ε_y), the Poisson's ratio (μ) represent as follows:

$$\mu = -\frac{\varepsilon_x}{\varepsilon_y}, \quad \varepsilon_x = \Delta L/L, \quad \varepsilon_y = -\Delta D/D$$

where ΔL and L represent temporary length and initial length (parallel to the stretching direction), ΔD and D represent temporary width and initial width (perpendicular to the stretching direction), respectively.

Virtually all common materials, such as the rubber, become narrower in cross section when they are stretched ($\mu > 0$) (Fig. 6.4b). The reason why, in the continuum view, is that most materials resist a deformation in volume as determined by the bulk modulus K more than they resist a deformation in shape, as determined by the shear modulus G. However, some materials known as auxetic materials exhibit a negative Poisson's ratio. When subjected to positive strain in a longitudinal axis, the transverse strain in the materials will actually be positive ($\mu < 0$). For these materials, it is usually due to uniquely oriented, hinged architectures as shown in Fig. 6.4c. In order for these architectures to stretch in the longitudinal direction, the hinges must "expand" in the transverse direction, effectively exhibiting a positive strain, which is called mechanical metamaterials.

Herein, we report a new strengthening method of macro-scale DN composite by utilizing the internal conflict based on the Poisson's ratio mismatch (Fig.6.4d). Considering the composite that consist of auxetic reinforcing phase ($\mu < 0$) and NR matrix ($\mu > 0$), transverse direction of the reinforcing phase expand with extension of the composite (Fig.6.4d-ii). While the NR matrix tend to shrunk to transverse direction with stretching of the composite (Fig.6.4d-ii). These counter Poisson's effect may induce internal conflict, indicating that high force is required for stretching of the composites (Fig.6.4d-iii). To investigate this concept, firstly, we prepared three types of reinforcing architectures, auxetic, rectangle, and honeycomb, which is determined by the interior angle θ (Fig. 6.5a). The Poisson's ratio of each architectures were estimated by uniaxial tensile tests of neat resin grid and the results are shown in Fig. 6.5b. According to the graph, the Poisson's ratio of reinforcing phase were precisely controlled by the architectures (interior angle). We note that the Poisson's ratio of NR matrix was also estimated and plotted on the graph as $\mu = 0.49$.

To investigate the geometrical effect of reinforcing phase in the composites on mechanical properties, we performed uniaxial tensile tests. Typical force-displacement curves of the composite, pristine NR matrix, and neat 3D-printable resin grid (interior angle $\theta=60°$) are shown in Fig. 6.6a. From the curves, internal fracture force (initial fracture of internal grid) (F), were estimated for all architectures. To clearly understand the enhance effect of various architectures, enhancement ratio for stretching (E_s) is calculated as follows:

$$E_s = F_{comp}/F_{grid}$$

Where F_{comp} and F_{grid} represent internal fracture force of composite and neat grid, respectively. In Fig. 6.6b, the relationship between E_s and Poisson's ratio of grid (neat grid) is displayed. Interestingly, when the Poisson's ratio is nearly 0.5, which is similar to that of NR matrix, the E_s exhibit minimum value. However, when the geometry of reinforcing phase is auxetic architectures, the E_s is highly increased, indicating that the counter Poisson's effect between reinforcing phase and NR matrix induce strengthening effect of composites. Surprisingly, not only auxetic architecture but also honeycomb architecture that show highly positive Poisson's ratio exhibit the significant high E_s. Therefore, it is considered that the mismatch of Poisson's ratio between reinforcing phase and matrix play an important role for induced the enhance effect.

We thought that this enhance effect induced by the internal conflict based on the Poisson's effect. Due to the high stiffness of reinforcing phase, soft NR matrix are stretched or compressed by the deformation of reinforcing phase. At this point, if Poisson's ratio of the reinforcing phase is far from that of NR matrix, the reinforcing phase deform NR matrix largely, resulting in high force during stretching. In order to observe this phenomenon experimentally, deformation of neat grids and composites are observed from top direction under polarized optical microscope (POM) (Fig. 6.6c,d).

As we expected, an area of one cell in neat grids with auxetic or honeycomb architectures were expanded with stretching (Fig. 6.6c-i,iii). While the rectangle architecture maintained an area of one cell in the neat grid (Fig. 6.6c-ii). We then observed composite samples and found that honeycomb one showed strong birefringence in NR matrix induced by high extension due to high positive Poisson's effect of honeycomb architecture. However, rectangle one did not exhibit strong birefringence because of less Poisson's mismatch. As for auxetic one, we could not observe birefringence, but that indicate no extension of NR matrix. Because the auxetic architecture exhibit negative Poisson's effect, inducing biaxial stretching of NR matrix and this deformation usually cancelled the birefringence. Therefore, the results of POM observation well agree with the relationship between enhancement ratio and Poisson's ratio of neat grid and we considered it is good experimental proof.

6.3.3 3D geometrical effect of reinforcement on mechanical properties (compression)

Owing to the negative Poisson's effect of auxetic architectures, they have a great potential application for shock-absorbable materials[24]. In this section, we expand the macro-scale DN composite architectures from two-dimensions to three-dimensions and performed uniaxial compression tests. As a hard reinforcing phase of the composites, four kinds of 3D architectures, which is determined interior angle (θ), were prepared (Fig. 6.7a). The Poisson's ratio that is estimated from the ratio of transverse extension strain to longitudinal compression strain in the direction of compressive force is well controlled by the θ (60° ~ 90°) as shown in Fig. 6.7b. We then fabricate the composite using these 3D architectures as a hard reinforcing phase and polyvinyl alcohol (PVA) hydrogel as soft matrix. The results of uniaxial compression tests were displayed in Fig. 6.8a-d. From the force-displacement curves, internal fracture force (initial fracture of internal grid) (F), were estimated for all architectures in the same way as uniaxial tensile testing. To investigate the enhance effect of 3D architectures, enhancement ratio for compression (E_c) is calculated as follows:

$$E_s = F_{comp}/F_{grid}$$

Where F_{comp} and F_{grid} represent internal fracture force of composite and neat grid, respectively (Fig. 6.8e). In Fig. 6.8f, the relationship between E_c and Poisson's ratio of grid (neat grid) is displayed. As we expected, the E_c is dramatically increased with decrease of Poisson's ratio. This is same trend as tensile testing yet we could observe significant increase effect for compression test. It is considered that the auxetic architectures are suitable for enhancing the mechanical propertied during compression tests because of the negative Poisson's effect (densification easily occur with compression). In addition to this, 3D architectures have more effective region (deformable part) than 2D architectures due to the lattice-like architectures. These results will open new field designing effective 3D architectures for composites materials, not only the macro-scale DN composites but also conventional composite materials, including fiber-reinforced plastic, reinforce concrete, and so on.

6.4 Conclusions

In conclusion, we demonstrate that macro-scale double network composite based on a hard 3D-printable resin and a soft matrix such as natural rubber and polyvinyl alcohol. When the strength of the reinforcing phase is comparable to the soft matrix, the toughness of the composite is significantly increased based on the sacrificial bond principle that is found in micro-scale (classical) double network gel. Furthermore, utilizing the unique architectures, such as auxetic and honeycomb possessing negative and highly positive Poisson's ratio, for the reinforcing phase, the mechanical properties of the composites are dramatically increased. This is because the mismatch of the Poisson's ratio between reinforcing phase and matrix induce the internal conflict, leading high deformation of matrix. We experimentally observed this anomalous deformation by polarized optical microscopy and considered that the large deformation induce high force during mechanical testing. This trend could be observed both 2D architecture system (investigated by uniaxial tensile test) and 3D architecture system (investigated by uniaxial compression test). We should note that only a few experiment were performed in this work, however, the obtained results are quite interesting and it might be giant step for designing super-tough materials based on the composite and the geometrical approach.

6.5 References

1. J. P. Gong, Y. Katsuyama, T. Kurokawa, Y. Osada, *Adv. Matter.*, **15,** 1155 (2003).
2. T. Nakajima, H. Furukawa, Y. Tanaka, T. Kurokawa, Y. Osada & J. P. Gong, *Macromolecules,* **42,** 2184 (2009).
3. A. Nakayama, A. Kakugo, J. P. Gong, Y. Osadam M. Takai & R. Erata, *Adv. Funct. Mater.,* **14,** 1124 (2004).
4. J. P. Gong, *Soft Matter* **6,** 2583-2590 (2010).
5. X. Feng, Z. Ma, J. V. MacArthur, C. Giuffre, A. Bastawros & W. Hong, *Soft Matter* **12,** 8999-9006 (2016).
6. Y. H. Na, Y. Tanaka, Y. Kawauchi, H. Furukawa, T. Sumiyoshi, J. P. Gong & Y. Osada, *Macromolecules,* **39,** 4641 (2006).
7. E. B. Schubert & D. Floreano, *RSC Advances* **3,** 24671 (2013).
8. I. M. V. Meerbeekm, B. C. M. Murray, J. W. Kim, S. S. Robinson, P. X. Zou, M. N. Silbertein & R. F. Shepherd, *Adv. Mater.* **28,** 2801-2806 (2016).
9. A. Tonazzini, S. Mintchev, B. Schubert, B. Mazzolai, J. Shintake & D. Floreano, *Adv. Mater.* **28,** 10142-10148 (2016).
10. H. Lipson & M. Kurman, *"Fabricated: The New World of 3D Printing", John Wiley & Sons,* **ISBN: 1118416945** (2013).
11. J. Kopac & Z. Kampus, *J. Mater. Process. Tech.,* **162-163,** 622 (2005).
12. M. Schuettler, S. Stiess, B. V. King & G. J. Suaning, *J. Netural Eng.,* **2,** 121 (2005).
13. G. Schade, *US Patent,* **4077075,** 625 (1978).
14. A. K. Geim, S. V. Dubonos, I. V. Grigorieva, K. S. Novoselov, A. A. Zhukov & Yu. Shapoval, *Nat. Mater.,* **2,** 461 (2003).
15. B. Gralak, G. Tayeb & S. Enoch, *Optics Express,* **9,** 567 (2001).
16. U. G. K. Wegst, H. Bai, E. Saiz, A. P. Tomsia & R. O, Ritchine, *Nat. Mater.,* **14,** 23 (2015).
17. K. jin, T. Tian, J. S. Erickson, J. Puthoff, K. Autumn & N. S. Pesika, *Langmuir,* **28,** 5737 (2012).

18. A. Saito, *Sci. Technol. Adv. Mater.* **13,** 029501 (2012).
19. D. Schuring, J. J. Mock, B. J. Justice, S. A. Cummer, J. B. Pendry, A. F. Starr & D. R. Smith, *Science,* **314,** 977 (2006).
20. N. I. Landy, S. Sajuyigbe, J. J. Mock, D. R. Smith & W. J. Padilla, *Phys. Rev. Lett.* **100,** 207402 (2008).
21. J. Valentine, S. Zhang, T. Zentgraf, E. Ulin-Avila, D. A. Genov, G. Bartal & X. Zhang, *Nature*, **455,** 376 (2008).
22. K. E. Evans & A. Alderson, *Adv. Mater.,* **12,** 617 (2000).
23. G. N. Greaves, A. L. Greer, R. S. Lakes & T. Rouxel, *Nat. Mater.*, **10,** 823 (2011).
24. W. Yang, Z.-M. Li, W. Shi, B.-H. Xie & N.-B. Yang, *J. Mater. Sci.*, **39,** 3269 (2004).

6.6 Schemes

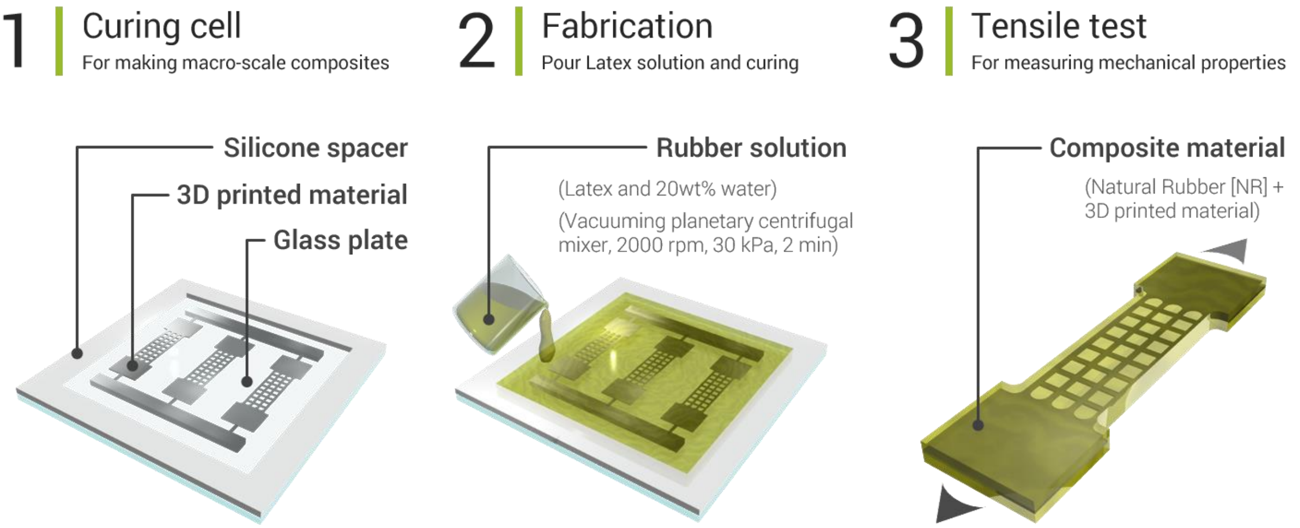

Scheme 6.1 | Fabrication of 3D printable resin reinforced natural rubber (NR) composites.

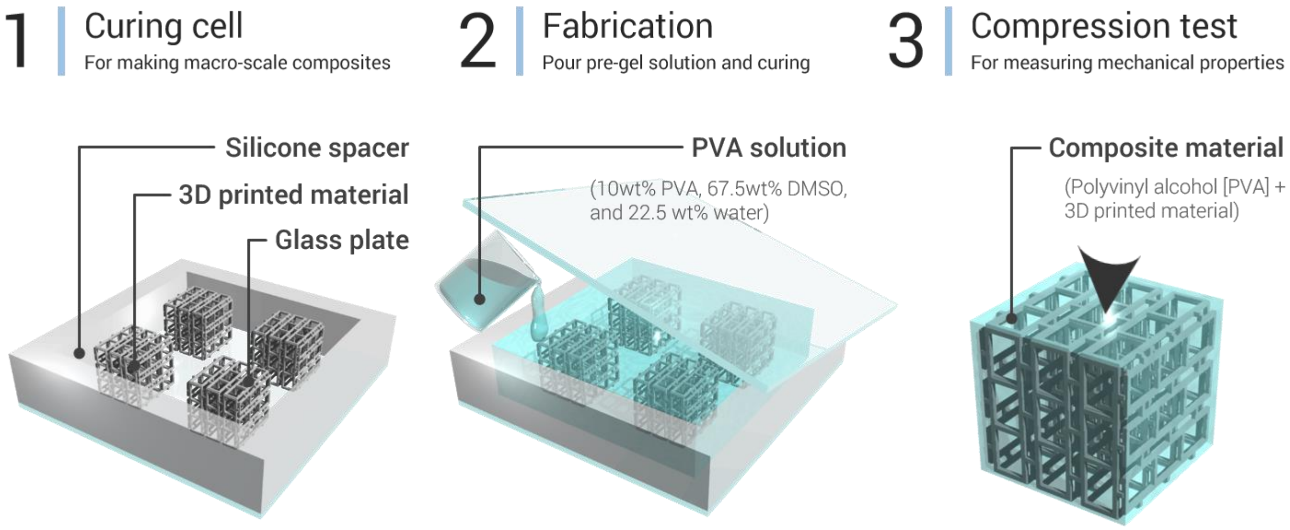

Scheme 6.2 | Fabrication of 3D printable resin reinforced polyvinyl alcohol (PVA) gel composites.

6.7 Figures

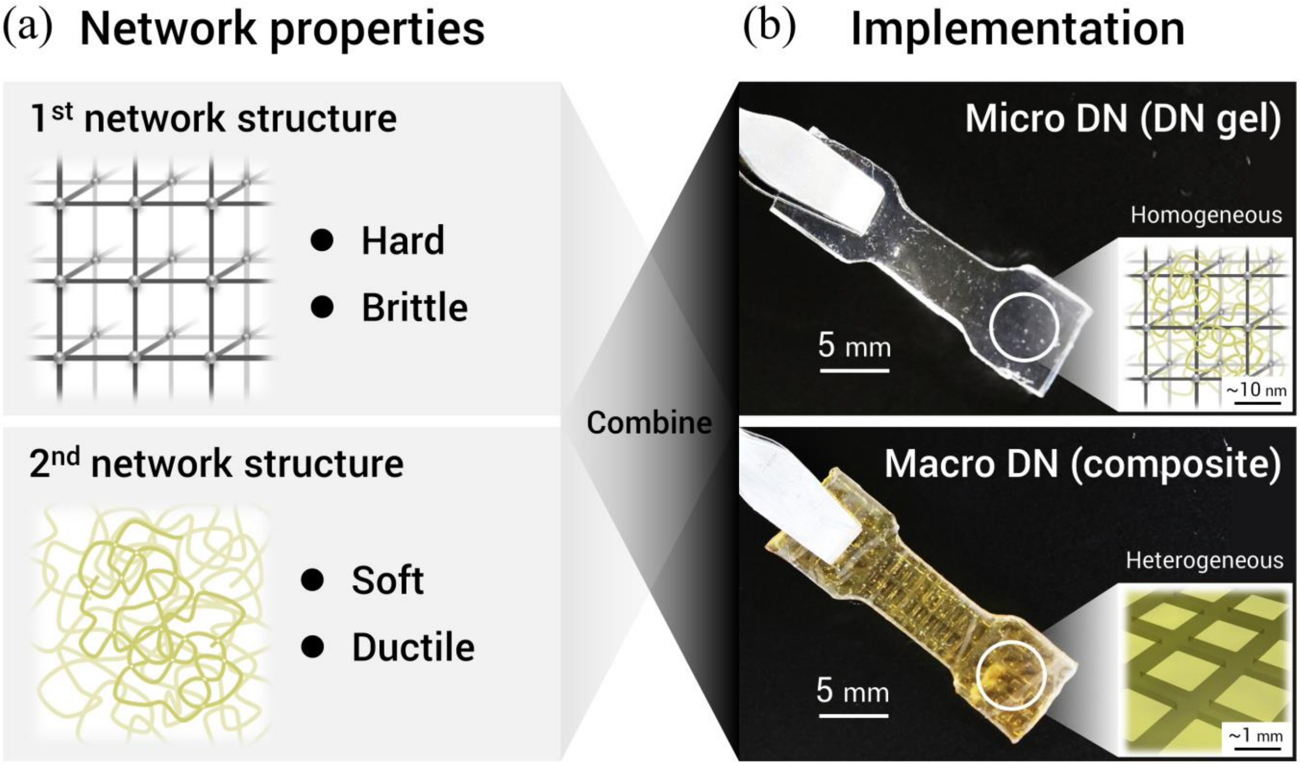

Figure 6.1 | Schematic illustrations of micro and macro double network materials. (a) Required network properties for creating double network materials; hard/brittle properties and soft/ductile properties are necessary for 1st network and 2nd network, respectively. **(b)** Implementation of double network concept in micro- and macro-scales. Traditionally, micro-DN gels have a first network consisting of a polyelectrolyte, such as PAMPS, and a second network consisting of a neutral material such as polyacrylamide. The macro-DN composite has a first network consisting of a 3D printed, rigid grid of (insert polymer name), and a un-crosslinked natural rubber second network.

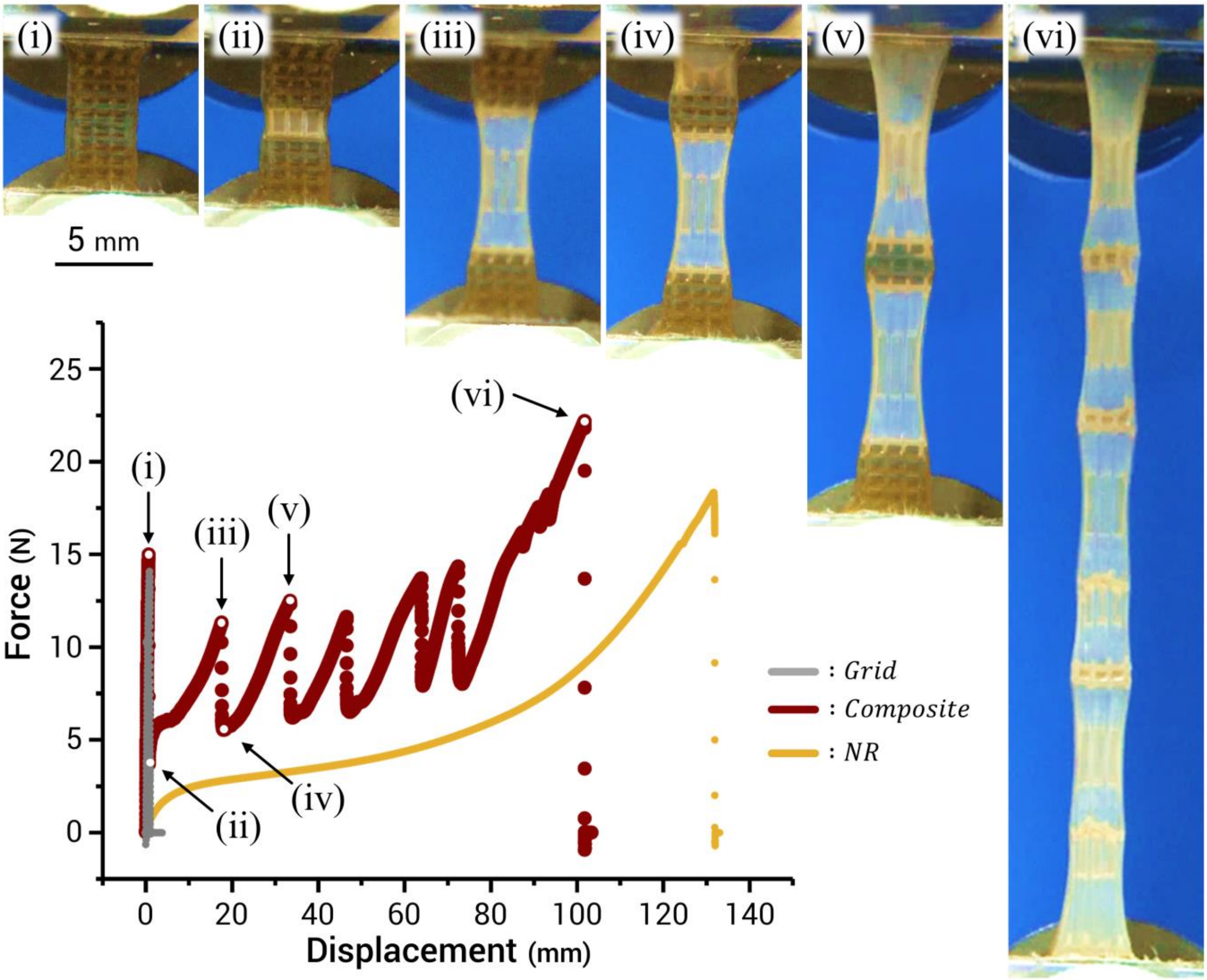

Figure 6.2 | Mechanical properties of macro-scale composites. Force-displacement curves of a square-grid skeleton (grey), pristine natural rubber (yellow), and their composite (wine). The insets (i)-(vi) represent snapshots of the composite sample at the corresponding stretch shown in the loading curves. (i) Initially, the force of the composite rapidly increased and the grid skeleton with the composite broke at a force comparable to that of the neat grid skeleton. (ii) Then, the force of the composite decreases, as the strain is transferred to the rubber within the fractured region of the composite. (iii) with increasing displacement, the natural rubber in the fractured zone stretches, increasing the load until it causes another fracture in the grid skeleton. (e.g. iv-v) During further stretching of the sample, multiple fractures of the grid skeleton were observed, while the natural rubber matrix maintains global integrity. As a result, bulk fracture did not occur. (vi) After the skeleton grid is fractured into many small “islands,” the natural rubber eventually ruptured.

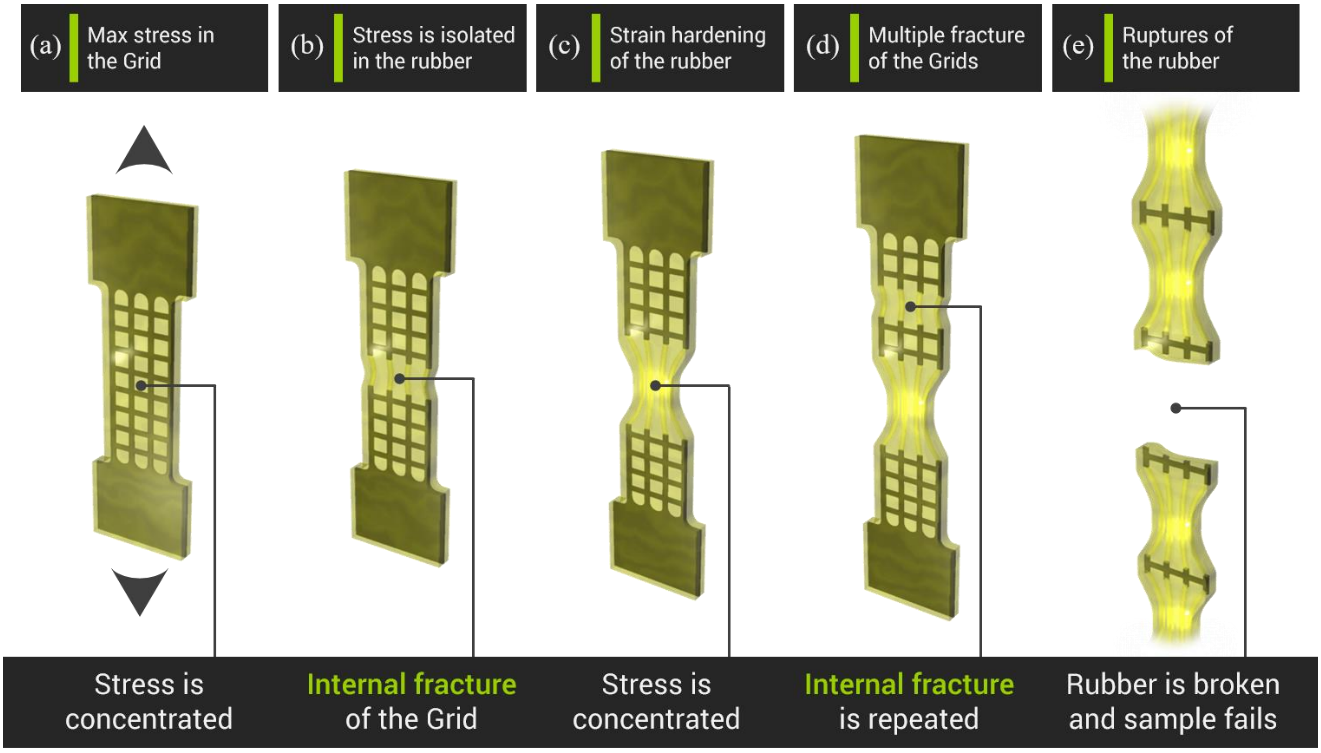

Figure 6.3 | Schematic illustrations of fracture process of the macro-scale DN composites. (**a**) Firstly, when the sample is stretched, the stress is concentrated on the grid. (**b**) Secondly, internal fracture of the grid occur and stress is isolated in the rubber. (**c**) Thirdly, stress is concentrated on the rubber and strain hardening of rubber occur. (**d**) After that, another part of grid is fractured and this cycle is repeated many times. During this process, energy is well dissipated. (**e**) Then finally, rubber is broken and whole sample fails.

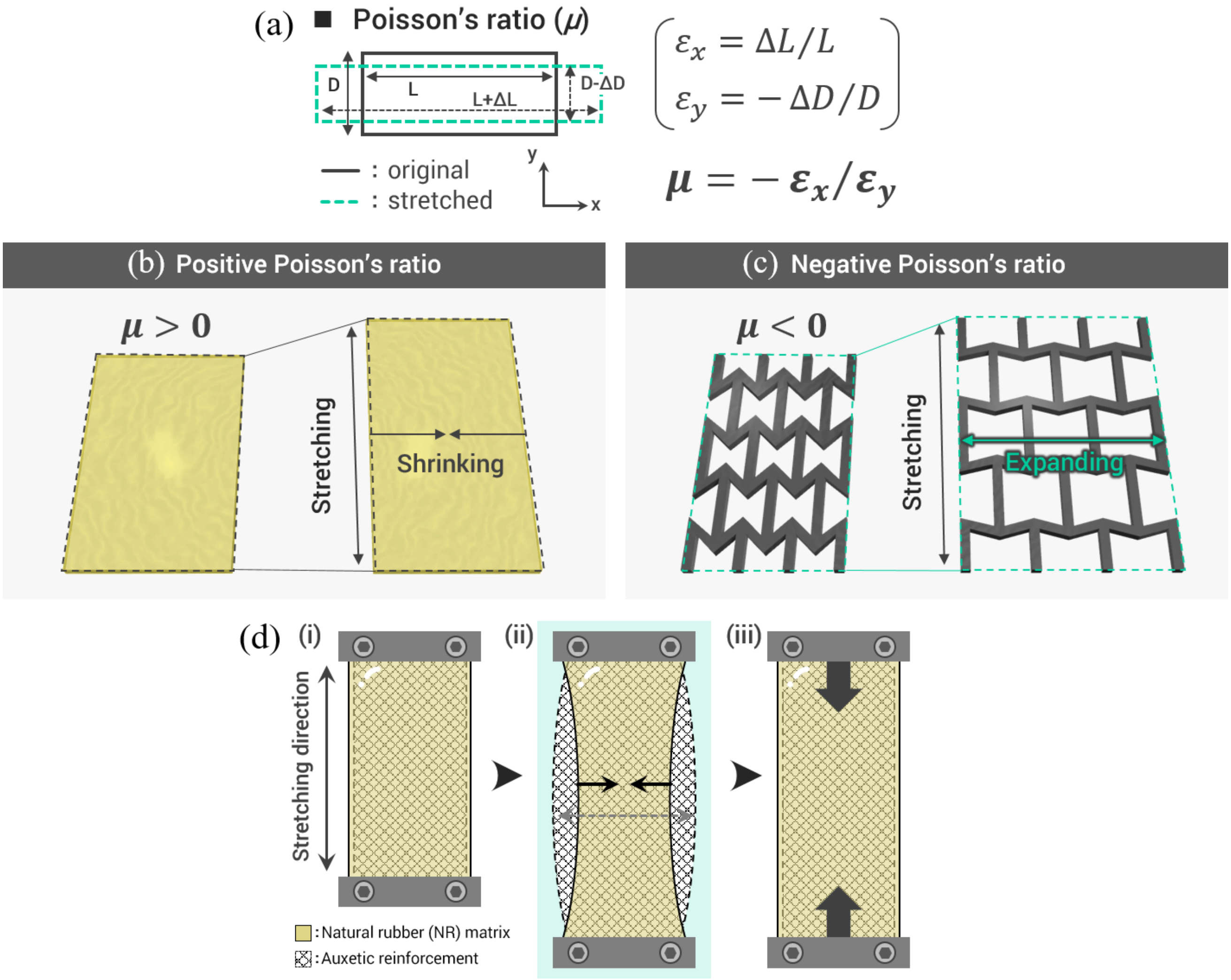

Figure 6.4 | Schematic illustrations of reinforcing mechanism of the macro-scale DN composites based on Poisson's ratio mismatch. (**a**) Definition of Poisson's ratio that is the ratio of transverse contraction strain to longitudinal extension strain in the direction of stretching force. Tensile and compression deformation are considered positive and negative, respectively. (**b**) Schematic illustration of deformation of NR that exhibit positive Poisson's ratio. (**c**) Schematic illustration of deformation of auxetic grid that exhibit negative Poisson's ratio. (**d**) Novel enhancing mechanism of mechanical properties. When the reinforcing phase of macro-scale DN composite show negative Poisson's ratio, extension force is considered to be increased due to the internal conflict induced by the mismatch of Poisson's ratio between reinforcing phase and matrix phase.

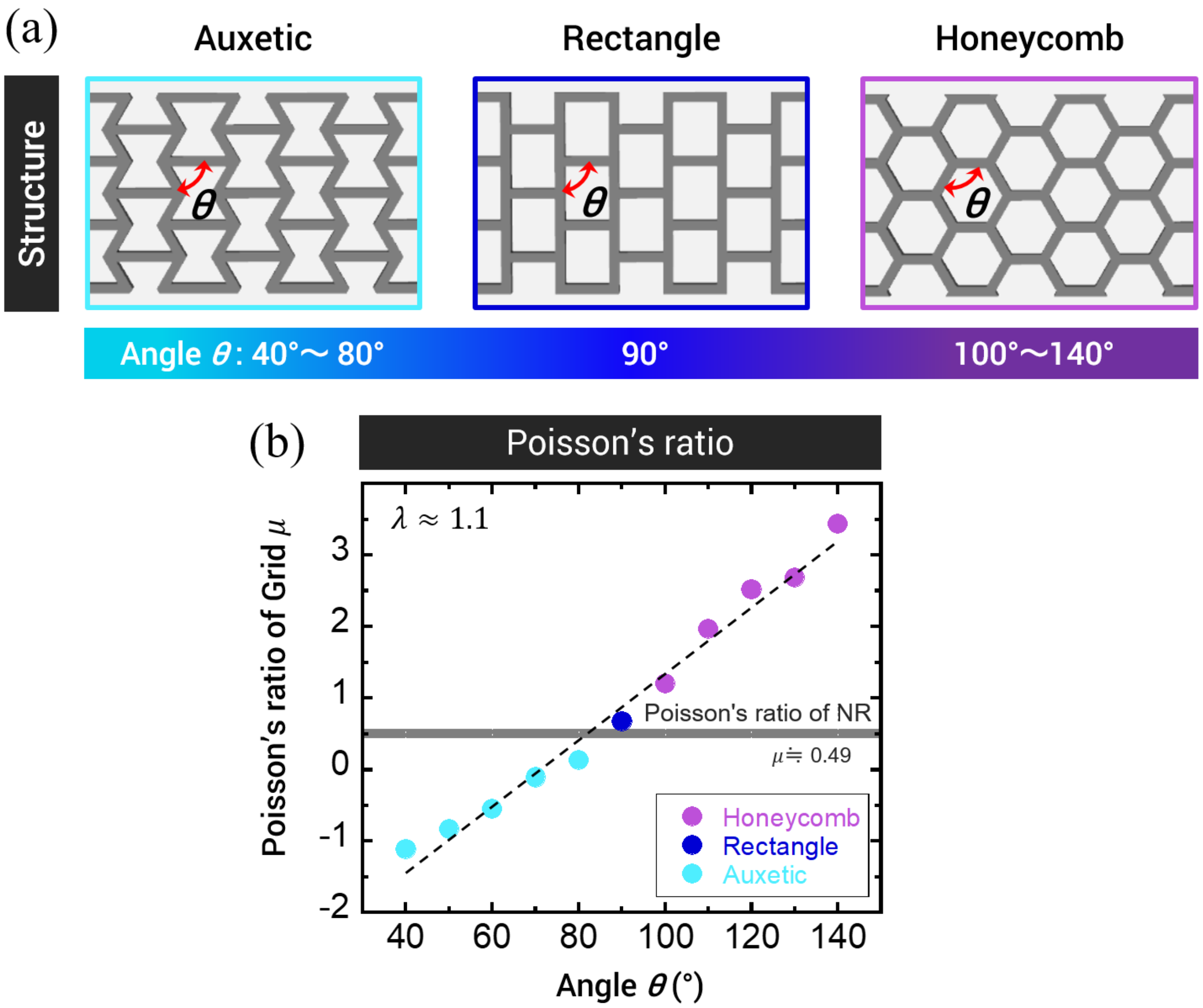

Figure 6.5 | Various architectures of reinforcing phase with controllable Poisson's ratio (a) Schematic illustration of three different types of architectures; Auxetic, rectangle, and honeycomb, which is determined by the interior angle, θ. (**b**) Linear relationship between Poisson's ratio of grid, μ and interior angle, θ. The light blue, blue, and purple dots represent the auxetic, rectangle, and honeycomb shape of reinforcing phase, respectively. The Poisson's ratios are estimated from the ratio of transverse contraction strain to longitudinal extension strain in the direction of stretching force (extension strain: ~1.1). Inset gray color line represent the Poisson's ratio of NR, μ = 0.49.

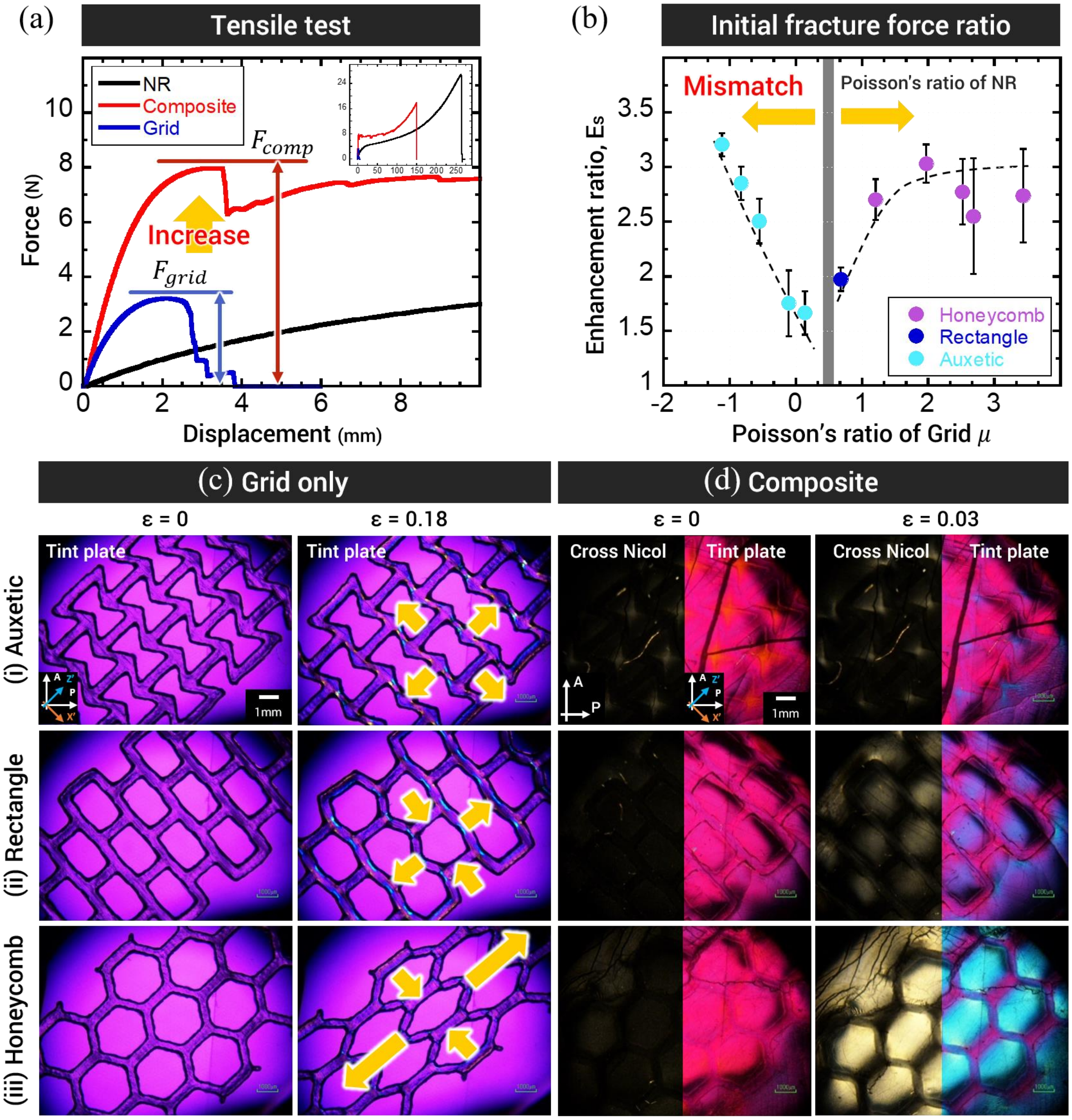

Figure 6.6 | Enhanced mechanical properties based on the Poisson's ratio mismatch (**a**) Typical force-displacement curves of the composite (red), neat resin grid (blue), and pristine NR (black), respectively. For typical example, the results of the auxetic architecture (interior angle; 60°) were displayed. (**b**) Enhancement ratio for stretching (E_S), which is increase ratio of initial fracture force of internal grid, is related to the Poisson's ratio of the grid. The gray line represents the Poisson's ratio of NR matrix. (**c,d**) Polarized optical microscope (POM) observation of neat resin grid (c) and composites (d), respectively. The auxetic (i), rectangle (ii), and honeycomb (iii) architectures were observed by POM with and without tint plate. A: Analyzer; P: Polarizer; X′: Fast axis of the tint plate; Z′: Slow axis of the tint plate.

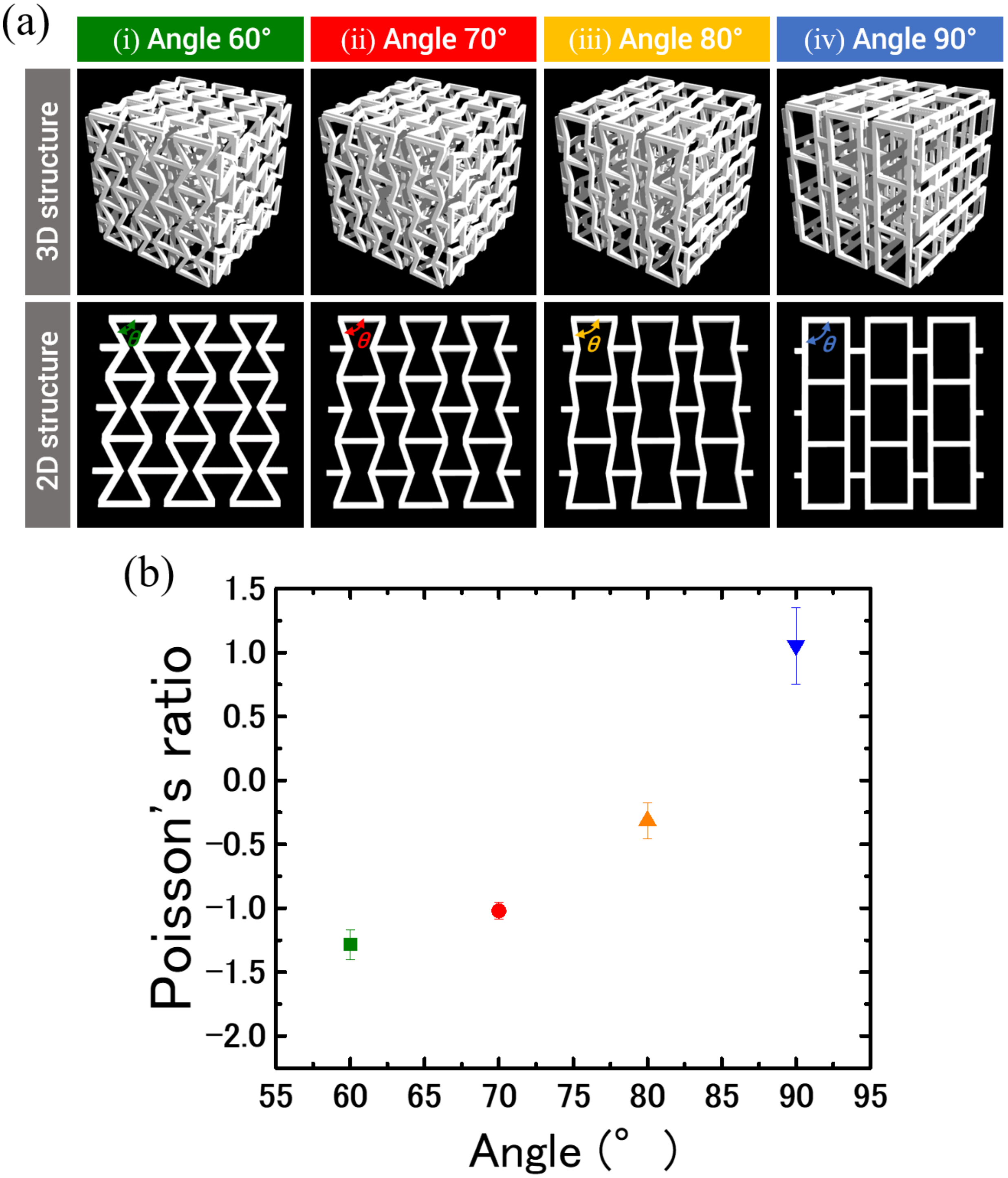

Figure 6.7 | 3D architectures of reinforcing phase with controllable Poisson's ratio (**a**) Schematic illustration of lattice-like 3D architectures determined by the interior angle, θ. (**b**) Relationship between Poisson's ratio of grid, μ and interior angle, θ. The green, red, yellow, and blue dots represent the 60°, 70°, 80°, and 90° of interior angle in the shape of reinforcing phase, respectively. The Poisson's ratios are estimated from the ratio of transverse extension strain to longitudinal compression strain in the direction of compressive force (compression strain: ~1.1).

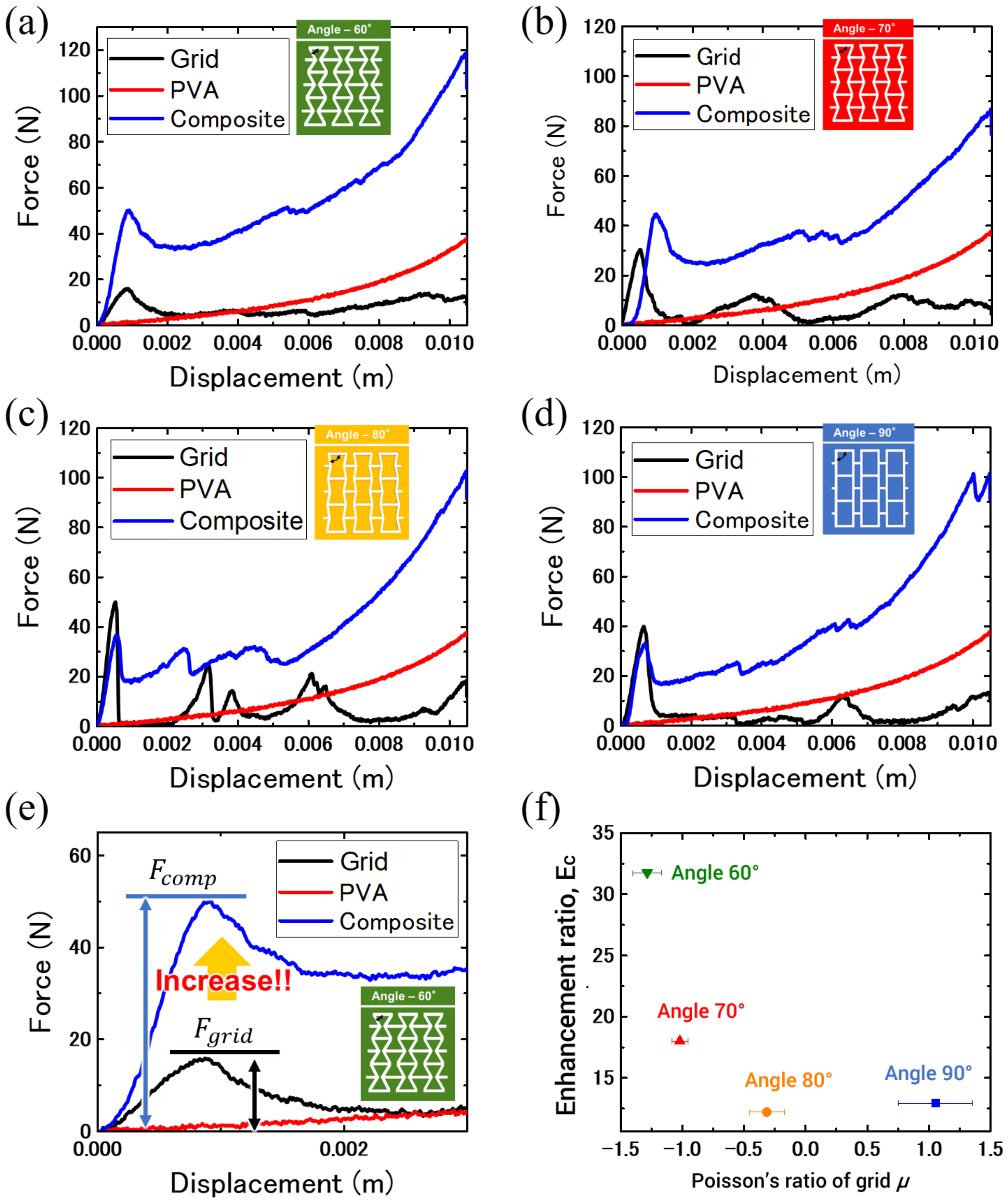

Figure 6.8 | Enhanced mechanical properties based on the 3D architectures (**a,b,c,d**) Typical force-displacement curves of the composite (blue), neat resin grid (black), and pristine NR (red), respectively. Results of interior angle 60°(a), 70°(b), 80°(c), and 90°(d) were displayed. (**e**) Enhancement ratio for compression (E_c), which is increase ratio of initial fracture force of internal grid, is estimated from the force-displacement curves of the composite and the neat grid. (**f**) Comparisons of enhancement ratio and Poisson's ratio.

CHAPTER 7

Summary of the dissertation

In this dissertation, we have introduced two kinds of hydrogel composites: from micro-scale to macro-scale composite hydrogels. In both systems, combination of rigid reinforcing phase and soft hydrogel matrix play an important role to emergence functions. Through the simple yet versatile design concept, we successfully obtained the composite hydrogels exhibiting unique functions such as optical anisotropy, stress visualization, stimulus-response, outstanding mechanical properties and etc., which could not attain with a single material. The following conclusions were given:

1) Micro-scale composite hydrogels

A cationic polyelectrolyte hydrogel that contain dispersed semi-rigid anionic polyelectrolytes (like as filler) have been developed as the micro-scale composite hydrogel. **In chapter 3,** we demonstrated a novel method to control orientation of semi-rigid polyelectrolyte based on an internal stress field induced by a swelling mismatch. For tuning the swelling mismatch, photo-lithography technique during UV polymerization was applied. Due to the osmotic pressure difference between UV-irradiated and un-irradiated regions, desirable swelling mismatch could be introduced. The orientation of semi-rigid polyelectrolytes induced by the internal stress field are fixed by poly-ion complexation between the cationic hydrogel matrix and the anionic semi-rigid polymer. Through this technique, we created the composite hydrogels with complicated structure of semi-rigid polyelectrolytes that is similar system to the articular cartilage with intricate structure of semi-rigid collagen fibrils.

In chapter 4, we demonstrated a function of the micro-scale hydrogel composites as stress sensor for hydrogel matrix. By determining the orientation of semi-rigid polyelectrolytes in the hydrogel, we successfully visualize the internal stress field, which recall us the history of stress during swelling. We found that heterogeneous rapid swelling of polyelectrolyte hydrogel induced stress field due to the swelling mismatch and the experimental results well agree with a mathematical model that we established.

2) Macro-scale composite hydrogels

In chapter 5, Low Melting Point Alloy (LMA) reinforced hydrogels have been developed as the macro-scale composite hydrogels. Taking advantage of the solid-liquid phase transition of LMA, we successfully released the swelling mismatch between hydrogel matrix and reinforcing phase. This approach could be applied to both swellable and de-swellable hydrogel matrix, indicating that it is universal method for creating macro-scale composite hydrogels. Besides the releasing swelling mismatch, tunable mechanical properties, shape-memory effect, self-healing ability via thermal activation were demonstrated. Moreover, the combination of rigid reinforcing phase and tough soft matrix highly enhanced the mechanical properties, such as stiffness, extensibility and toughness, based on a “sacrificial” bond principle. Specifically, internal LMA skeleton was multiply ruptured with stretching of composite hydrogels, resulting in high stretchability maintain high stiffness. This work show that the principle that found in double network gel could be expanded to macro-scale composites.

In chapter 6, 3D-printed polyurethane reinforced natural rubber or polyvinyl alcohol gel have been developed as the macro-scale composites. We then demonstrated an effect of geometry of reinforcing phase on mechanical properties. When we used a square-grid for the geometry, the multiple fracture of reinforcing phase also observed and showed high toughness. Additionally, utilizing the functional geometry such as an auxetic shape (flexible shape possessing negative Poisson’s ratio), we successfully controlled and enhanced the mechanical properties of the composites, including Young’s modulus, Poisson’s ratio and toughness. This high selectivity (material, geometry) of the composites is one of a great advantage to create functional composites towards applications in diverse fields.

Recent progress of hydrogel research is changing our thinking about hydrogels from “weak and brittle” materials to “strong and tough” materials. Beyond the toughness, next challenge is how to introduce multiple functions for practical applications of hydrogels. To create multi-functional materials, the composite approach is one of the smart way and we believe that the research will find use in the fields of soft robotics, wearable electronics, and biocompatible functional materials.

List of Publications

7.1 Original papers

1. **R. Takahashi,** Z. L. Wu, Md. Arifuzzaman, T. Nonoyama, T. Nakajima, T. Kurokawa & J. P. Gong: "Control Superstructure of Rigid Polyelectrolytes in Oppositely Charged Hydrogels via Programmed Internal Stress" *Nat. Commun.*, **5,** 4490 (2014).
2. **R. Takahashi,** Y. Ikua, D. R. King, T. Nonoyama, T. Nakajima, T. Kurokawa, H. Kuroda, Y. Tonegawa & J. P. Gong: "Coupled instabilities of surface crease and bulk bending during fast free swelling of hydrogel" *Soft Mater,* **12,** 5081-5088 (2016).
3. **R. Takahashi,** T. L. Sun, Y. Saruwatari, T. Kurokawa, D. R. King & J. P. Gong: "Creating Stiff, Tough and Functional Hydrogel Composites with Low Melting Point Alloys" *Adv. Mater.* **in press (DOI: 10.1002/adma.201706885).**
4. **R. Takahashi,** T. Okumura, T. kurokawa, D. R. King & J. P. Gong: "Fabrication of Tough and Functional Soft Composites Utilizing Macroscopic Unique Structures of Reinforcements" **in Preparation.**

7.2 Other papers

1. Md. Arifuzzaman, Z. L. Wu, **R. Takahashi,** T. Kurokawa, T. Nakajima & J. P. Gong: "Geometric and Edge Effects on Swelling-Induced Ordered Structure Formation in Polyelectrolyte Hydrogels" *Macromolecules,* **46,** 9083-9090 (2013).
2. Z. L. Wu, **R. Takahashi,** D. Sawada, Md. Arifuzzaman, T. Nakajima, T. Kurokawa, J. Hu & J. P. Gong: "In Situ Observation of Ca 2+ Diffusion-Induced Superstructure Formation of a Rigid Polyanion" *Macromolecules,* **47,** 7208-7214 (2014).
3. K. Yanagisawa, **R. Takahashi,** N. Fumihiko, Y. Sumiya, R. Iida, A. Nitta, T. Kura, Y. Toguchi, R. Kojima & T. Fujiyoshi: "Reasons and Problems When Research Results are Announced : Graduate Student's Opinions" *J. J. Sci. Commun.*, **18,** 145-154, (2015).
4. X. Li, T. Kurokawa, **R. Takahashi,** Md. Haque, Y. Yue, T. Nakajima & J. P. Gong: "Polymer Adsorbed Bilayer Membranes Form Self-Healing Hydrogels with Tunable Superstructure" *Macromolecules,* **7,** 2277-2282 (2015).
5. **R. Takahashi,** K. Shimano, D. R. King, T. Nakajima, T. Nonoyama, T. Kurokawa & J. P. Gong: "High Fidelity Functional Coatings from Tough Particle Double Network Hydrogels" **in Preparation.**
6. D. R. King, T. Okumura, **R. Takahashi,** T. Kurokawa & J. P. Gong: "Creation of Novel Composite Materials Possessing a Macroscale Double-Network Structures" **in Preparation**
7. **R. Takahashi,** T. Ikai, T. Nakajima, T. Nonoyama, T. Kurokawa, D. R. King & J. P. Gong: "Creation of Tough and Mechanically Tunable Hydrogels via the Double Network Principle with Semi-Rigid Polyelectrolytes" **in Preparation.**

7.3 Presentation and published abstracts in scientific meetings

1. **R. Takahashi,** T. Nonoyama, T. Kurokawa, T. Nakajima & J. P. Gong: "Fabrication of Electrical Conductive Hydrogels Utilizing a Silver-coating", 64th SPSJ Annual meeting (May, 2015, Sapporo). (**Poster Presentation Award**)
2. **R. Takahashi,** T. Nonoyama, T. Kurokawa, T. Nakajima & J. P. Gong: "Fabrication of Electrical Conductive Hydrogels with High Stretchability", NTU-HU Joint Materials Science Workshop 2015 (October, 2015, Taipei).
3. **R. Takahashi,** T. Nonoyama, T. Kurokawa, T. Nakajima & J. P. Gong: "Fabrication of Tough and Functional Hydrogels with Macroscale Anisotropic Structures" Pacifichem 2015 (December, 2015, Honolulu).
4. **R. Takahashi,** T. Nonoyama, T. Kurokawa, T. Nakajima & J. P. Gong: "Stripe-like Crease Pattern Formation during Fast Free Swelling of Polyelectrolyte Hydrogel", 65th SPSJ Annual meeting (May, 2016, Kobe).
5. **R. Takahashi,** D. R. King, T. Nonoyama, T. Kurokawa T. Nakajima, T. L. Sun & J. P. Gong: "Fabrication of Low Melting Alloy Composite Hydrogels towards Obtaining Functional Materials", GI-CoRE Kick off Symposium (June, 2016, Sapporo).
6. **R. Takahashi,** D. R. King, T. Nonoyama, T. Kurokawa T. Nakajima, T. L. Sun & J. P. Gong: "Hydrogels – towards Further Applications of Biocompatible Materials", Seminar in NTT basic research laboratories, (June, 2016, Atsugi).
7. **R. Takahashi,** T. Nonoyama, T. Kurokawa, T. Nakajima & J. P. Gong: "Superstructure Formation of Rigid Polyelectrolytes in Hydrogel Matrix", ImPACT group meeting (July, 2016, Otaru).
8. **R. Takahashi,** D. R. King, T. Nonoyama, T. Kurokawa T. Nakajima, T. L. Sun & J. P. Gong: "Fabrication of Low Melting Point Alloy Composite Hydrogels and Emergence of Functions", Young researcher's symposium in Hokkaido University (August, 2016, Sapporo).
9. **R. Takahashi,** D. R. King, T. Nonoyama, T. Kurokawa T. Nakajima, T. L. Sun & J. P. Gong: "Fabrication of Low Melting Point Alloy Composite Hydrogels", 65th Symposium on Macromolecules (September, 2016, Yokohama).
10. **R. Takahashi,** D. R. King, T. Nonoyama, T. Kurokawa T. Nakajima, T. L. Sun & J. P. Gong: "Fabrication of Low Melting Point Alloy Composite Hydrogels for Applications", Gel workshop in Odaiba (September, 2016, Tokyo).
11. **R. Takahashi,** D. R. King, T. Nonoyama, T. Kurokawa T. Nakajima, T. L. Sun & J. P. Gong: "Fabrication of Low Melting Point Alloy Composite Hydrogels towards Obtaining Advanced Functional Materials", 4th International Life Science Symposium (November, 2016, Sapporo).

(**Excellent Presentation Awards**)

12. **R. Takahashi,** D. R. King, T. Nonoyama, T. Kurokawa T. Nakajima, T. L. Sun & J. P. Gong: “Fabrication of Macroscopic Composite Hydrogels to Increase Fracture Toughness”, APS March Meeting 2017 (March, 2017, New Orleans).
13. **R. Takahashi,** Z. L. Wu, Md. Arifuzzaman, T. Nonoyama, T. Kurokawa, T. Nakajima & J. P. Gong: “Controlling Superstructures of Rigid Polyelectrolytes in Oppositely Charged Hydrogels via Programmed Internal Stress” Hokkaido Summer Institute & International Soft Matter Summer School in Hokkaido 2017 (August, 2017, Otaki).
14. **R. Takahashi,** Z. L. Wu, Md. Arifuzzaman, T. Nonoyama, T. Kurokawa, T. Nakajima & J. P. Gong: “Superstructure Formation of Rigid Polyelectrolytes in Hydrogel matrix based on Programmable Internal Stress” HU-ImPACT Joint Symposium (August, 2017, Sapporo).
15. **R. Takahashi,** Y. Saruwatari, T. L. Sun, K. Takayuki, D. R. King & J. P. Gong: “Creating Stiff, Tough and Functional Hydrogel Composites based on Low Melting Point Alloys” International Symposium for Advanced Gel Materials & Soft Matters (August, 2017, Guiyang).

7.4 *Cover art of the published paper*

Volume 12 | Number 23 | 21 June 2016 | Pages 5063–5234

Soft Matter

www.softmatter.org

ISSN 1744-683X

ROYAL SOCIETY OF CHEMISTRY

PAPER
Jian Ping Gong *et al.*
Coupled instabilities of surface crease and bulk bending during fast free swelling of hydrogels

175 YEARS

R. Takahashi, Y. Ikua, D. R. King, T. Nonoyama, T. Nakajima, T. Kurokawa, H. Kuroda, Y. Tonegawa & J. P. Gong: "Coupled instabilities of surface crease and bulk bending during fast free swelling of hydrogel" *Soft Mater,* **12,** 5081-5088 (2016).

Acknowledgments

Undertaking this PhD research in the Laboratory of Soft & Wet Matter (LSW), Graduate School of Life Science, Hokkaido University (HU), Sapporo, Japan has been a really valuable experience for me and it would have been impossible to do without the guidance and support that I received from many people.

Firstly, I would like to say a very big thank you to my enthusiastic supervisor, **Professor Jian Ping Gong** for all the support and encouragement during my bachelor's, master's and doctoral study in LSW. She gave me not only her tremendous academic support to be an outstanding researcher but also so many wonderful opportunities to be a global leader. I really appreciate that she evaluated my interdisciplinary research. Moreover, I remembered that one of the most important things to be the leader is "tolerance", which was taught from her life-style. I deeply respect her amicable personality, positive attitude and research understanding and consider that I want to be so in future.

Many thanks also to Professor Dr. Takayuki Kurokawa, assistant Professor Dr. Tasuku Nakajima, assistant Professor Dr. Takayuki Nonoyama, assistant Professor Tao Lin Sun and assistant Professor Dr. Daniel R. King for their helpful attitude, scientific insight, fruitful discussions and useful suggestions regarding my research. Additionally, **Dr. Nonoyama** and **Dr. King** are really friendly, I often spent a lot of time with them to refresh. Without them it was truly difficult to complete my doctoral dissertation.

I am also very grateful to post-doctoral fellows, guest researcher and research assistants in LSW. Especially, Dr. Yoshinori Katsuyama, Mr. Masaya Iwata (NGK Spark Plug Co., Ltd.) and Ms. Yukiko Hane gave me not only a lot of scientific insight but also an attitude as a member of society. I also would like to thank the staffs in LSW; Ms. Eiko Hasegawa and Ms. Yuki Okubo for helping and teaching me in financial work of HU.

I greatly appreciate all the past and present Japanese and International students of LSW for their kind and friendly attitude. Especially, I would like to take the name of **Mr. Takuma Ikai** and **Mr. Tuyoshi Okumura** for their support in fabrication of micro-scale and macro-scale composite hydrogel system, without which it were very hard to prepare my dissertation and forth coming papers.

Here, I want to thank Mr. Yoshiyuki Saruwatari, Specialty Chemical Sales Department, Osaka Organic Chemical Industry LTD., for providing special monomer and teaching how to synthesis the monomer. Actually, the monomer is quite important of my doctoral dissertation.

I want to gratefully acknowledge the Japan Society for the Promotion of Science (JSPS) for providing me Grant-in-Aid for JSPS Fellow. Also thanks to Monbu-kagakusho (MEXT) for supporting my research by the Program for Leading Graduate Schools (Hokkaido University “Ambitious Leader’s Program”). It was impossible to complete my doctoral research without their financial support. In addition to this, taking part in the Ambitious Leader’s Program is a great asset for understanding what the global leader is. I really appreciate the program to give me such a wonderful opportunity.

Finally, but by no means least, grateful thanks to my family for almost unbelievable support. They are the most important people in my world and I dedicate this dissertation to them. I am truly happy because I could study as much as I want of what I like…

Riku Takahashi

Laboratory of Soft & Wet Matter
Graduate School of Life Science
Hokkaido University
Sapporo Japan
March 2018